

GUIDED-WAVE ATOM INTERFEROMETERS WITH  
BOSE-EINSTEIN CONDENSATE

by

Ebubechukwu Odidika Ilo-Okeke

A dissertation submitted to the faculty of

Worcester Polytechnic Institute

in partial fulfillment of the requirements for the degree of

Doctor of Philosophy

Department of Physics

Worcester Polytechnic Institute

April 2012

Copyright © 2012 Ebubechukwu Odidika Ilo-Okeke

All Rights Reserved

WORCESTER POLYTECHNIC INSTITUTE


GRADUATE COMMITTEE APPROVAL

of a dissertation submitted by

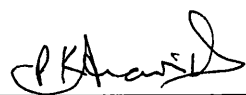
Ebubechukwu Odidika Ilo-Okeke

This dissertation has been read by each member of the following graduate committee and by majority vote has been found to be satisfactory.


4/23/2012  
Date

  
\_\_\_\_\_  
Alex A. Zozulya (Advisor), Professor of Physics,  
Worcester Polytechnic Institute

4/23/2012  
Date

  
\_\_\_\_\_  
Padmanabhan K. Aravind, Professor of Physics,  
Worcester Polytechnic Institute

4/23/2012  
Date

  
\_\_\_\_\_  
Konstantin A. Lurie, Professor of Mathematics,  
Worcester Polytechnic Institute

## DEDICATION

To God, who made heaven and earth

To my parents: Patrick Iloakaegbuna Okeke and Lucy Nwadiuto Okeke

## ABSTRACT

An atom interferometer is a sensitive device that has potential for many useful applications. Atoms are sensitive to electromagnetic fields due to their electric and magnetic moments and their mass allows them to be deflected in a gravitational field, thereby making them attractive for measuring inertial forces. The narrow momentum distribution of Bose-Einstein condensate (BEC) is a great asset in realizing portable atom interferometers. An example is a guided-wave atom interferometer that uses a confining potential to guide the motion of the condensate. Despite the promise of guided-wave atom interferometry with BEC, spatial phase and phase diffusion limit the contrast of the interference fringes. The control of these phases is required for successful development of a BEC-based guided-wave atom interferometer.

This thesis analyses the guided-wave atom interferometer, where an atomic BEC cloud at the center of a confining potential is split into two clouds that move along different arms of the interferometer. The clouds accumulate relative phase due to the environment, spatially inhomogeneous trapping potential and atom-atom interactions within the condensate. At the end of the interferometric cycle, the clouds are recombined producing a cloud at rest and moving clouds. The number of atoms in the clouds that emerge depends on the relative phase accumulated by the clouds during propagation. This is investigated by deriving an expression for the probability of finding any given number of atoms in the clouds that emerge after recombination. Characteristic features like mean, standard deviation and cross-correlation function of the probability density distribution are calculated and the contrast of the interference fringes is optimized. This thesis found that optimum contrast is achieved through the control of total population of atoms in the condensate, trap frequencies, s-wave scattering length, and the duration of the interferometric cycle.

## ACKNOWLEDGMENTS

I say a big “Thank You!” to all of you who made this thesis possible. First I would like to thank Prof. Alex Zozulya for giving me the opportunity to work with him. Through his ideas and understanding of physics he gave me good guidance and advice that I needed to feel the work I was doing was important. I would like to thank Prof. Ramdas Ram-Mohan for the invaluable time I spent in his lab learning some numerical techniques and programming skills some of which were used in this work.

I would like to thank Prof. Bede Anusionwu, Prof. Germano Iannacchione and Oscar Onyema for their encouragement which helped in my good and difficult moments. I would like to thank Jackie Malone for her assistance in helping me settle in when I first arrived in Worcester and all the other departmental secretaries Margaret Cassie (former) and Michele O’Brien for their assistance throughout my stay at WPI. I would like to thank the Department of Physics for supporting me as a Teaching Assistant for most part of my graduate programme.

Also I would like to thank all my friends and colleagues for sharing your time with me. I would like to thank all the persons in the Department of Physics, WPI. My interactions with you all have left me with memories of a lifetime.

Finally, my deepest gratitude goes to my family - my mother, my father, my sister and my brothers. They have always stood by me in good and bad times. I really owe my successes to them.

# Contents

<b>Table of Contents</b>	<b>vii</b>
<b>List of Figures</b>	<b>ix</b>
<b>1 Introduction</b>	<b>1</b>
1.1 Atom Interferometers . . . . .	3
1.1.1 Trapped-atom interferometer . . . . .	4
1.1.2 Guided-wave atom interferometer . . . . .	5
1.2 Outline of this Thesis . . . . .	8
<b>2 Tools of the trade</b>	<b>10</b>
2.1 Diffraction of atoms by light . . . . .	10
2.1.1 Bragg diffraction of atoms by light . . . . .	12
2.1.2 Atom diffraction using square-wave Bragg pulses . . . . .	15
2.1.3 Atom diffraction using Raman pulses . . . . .	19
2.2 Bose-Einstein condensation . . . . .	20
2.2.1 Critical temperature . . . . .	20
2.2.2 Critical phase space density . . . . .	21
2.3 Gross-Pitaevskii equation . . . . .	23
2.3.1 Thomas-Fermi approximation . . . . .	24
<b>3 Phase diffusion of Bose-Einstein condensate</b>	<b>27</b>
3.1 Atom-Michelson interferometer . . . . .	28
3.2 Atom-Mach-Zehnder interferometer . . . . .	32
3.3 Probability . . . . .	33
3.3.1 Mach-Zehnder interferometer . . . . .	33
3.3.2 Michelson interferometer . . . . .	35
3.4 Characteristic features of the probability density . . . . .	42
3.5 Comparison with experiments . . . . .	46
<b>4 Spatial phase and phase diffusion of Bose-Einstein condensate</b>	<b>52</b>
4.1 State vector at recombination . . . . .	54
4.2 Probability . . . . .	60
4.2.1 Probability for $\xi$ equal to zero . . . . .	60

---

4.2.2	Probability for $\xi$ not equal to zero . . . . .	64
4.2.3	Moments of the probability function . . . . .	71
4.3	Optimisation of interference fringe contrast . . . . .	74
4.4	Discussion . . . . .	78
<b>Bibliography</b>		<b>81</b>
<b>A Published Work</b>		<b>91</b>
<b>Index</b>		<b>102</b>



# List of Figures

1.1	Schematic representaion of the evolution of BEC atomic cloud in an atom Michelson interferometer. . . . .	6
2.1	Coupling of two-level atom by laser beam that is detuned from atomic resonance. . . . .	13
2.2	Dressed-state energies as a function of position at large detuning in a light standing wave. . . . .	16
2.3	Velocity distribution of an ensemble of atoms trapped in a magnetic optical trap at different temperatures. . . . .	23
3.1	The probability function $P(n_0)$ vs $n_0$ at three different values of $\theta$ . . .	37
3.2	The relative mean value $\langle n_0 \rangle / N$ vs $\theta$ . . . . .	38
3.3	The relative standard deviation $\Delta n_0 / N$ vs $\theta$ . . . . .	39
3.4	The probability function $P_0$ vs $n_0$ plotted at small values of $\xi$ . . . . .	44
3.5	Probability function $P_0$ vs $n_0$ for $\xi = 0.2/\sqrt{N}$ , $\theta = \pi/4$ and $N = 2000$ . . . . .	45
3.6	Probability function $P_0$ vs $n_0$ for $\xi = 1/\sqrt{N}$ , $\theta = \pi/4$ and $N = 2000$ . . . . .	46
3.7	An enlargement showing fast-scale spatial oscillations of $P_0$ . . . . .	47
3.8	Normalised mean value of atoms in the central cloud. . . . .	48
3.9	Normalised standard deviation of atoms in the central cloud. . . . .	49
3.10	Interference fringe contrast $V$ as a function of $\xi\sqrt{N}$ . . . . .	50
4.1	The basis vectors $\chi_0$ and $\eta_0$ versus the dimensionless coordinate $z$ . . .	58
4.2	The probability function $P_0$ at different values of spatial phase for 2000 atoms. . . . .	62
4.3	The normalised average number of atoms in the cloud at rest. . . . .	63
4.4	Normalised standard deviation of atoms at increasing spatial phase . . . . .	64
4.5	Contour plots of the probability function $P$ at small values of unwanted phase. . . . .	66
4.6	Contour plots of the probability function $P$ at large values of unwanted phase. . . . .	67
4.7	The probability function $P_{n_0}$ at different values of spatial phase. . . . .	69
4.8	Normalised mean value of atoms at different values of spatial phase for a fixed value of $\xi\sqrt{N}$ . . . . .	70

---

4.9	Normalised standard deviation at different values of spatial phase for a fixed value of $\xi\sqrt{N}$ . . . . .	72
4.10	Normalised mean values at different values of $\xi\sqrt{N}$ for a fixed value of spatial phase. . . . .	73
4.11	Normalised standard deviation at different values of $\xi\sqrt{N}$ for a fixed value of spatial phase. . . . .	74

# Chapter 1

## Introduction

Condensation in bosonic gases was first predicted by Einstein [1] in 1925 based on photon quantum statistics developed by Bose [2]. The transition from gaseous atoms to condensate occurs when the de Broglie wavelength becomes comparable to the mean distance between the atoms so that the wave functions of the atoms overlap and individual atoms become indistinguishable; large number of atoms occupies the lowest energy state. The search for Bose-Einstein condensation (BEC) started in liquid helium after Fritz London [3] pointed out that there could be a connection between superfluidity and condensation. However, interactions between the atoms in the liquid were so strong that only a few populations of atoms, about 10%, occupy the lowest energy state.

The search for BEC continued with a focus on atomic species that would interact weakly at very low temperature. Following the suggestions of Hecht [4] and later Stwalley and Nosanov [5], spin polarized hydrogen atoms were used in the first of these experiments. However, the adsorption [6] of hydrogen atoms on the surface of the cell walls made condensation impossible due to the loss of atoms to three-body recombination at low temperature. As a result, magnetic trapping [7] was used to

provide a wall-free confinement while evaporative cooling technique [8] was used to cool the atoms. These techniques are well suited for the trapping and cooling alkali atoms.

Using magnetic trapping and evaporative cooling techniques in conjunction with advances made in laser cooling of alkali atoms led to the first observation of BEC in rubidium vapour [9] in 1995 and later in vapours of lithium [10] and sodium [11]. More than a decade after observing the first BEC, condensation has been realised in many different atomic species [12–17] and molecules [18–20]. Also cooling fermions to very low temperature have resulted in the formation of degenerate gases [21]; all the Fermi particles do not occupy a single quantum state when compared to condensate due to Pauli's exclusion principle.

The realisation of BEC and quantum degenerate gases has provided researchers a new tool to probe quantum phenomenon most of which have been observed in other areas of physics. The earliest example was the observation of interference pattern [22] between two BEC due to wave-particle duality. Other examples include the observation of vortex formation in BEC [23] as a result of superfluid nature of the condensates, quantum tunneling of atoms across a potential barrier in optical lattices [24, 25], observation of quantum phase transition from superfluid to the Mott insulator phase of atoms in a periodic lattice [26], observation of itinerant ferromagnetism in a Fermi gas of ultra cold atoms [27], creation of squeezed states in BEC [28, 29] among others.

Condensates attract the interest of researchers for a number of reasons. It is a source of bright coherent beams of atoms just like lasers. Also, condensates are sensitive to external interactions because atoms have dipole moments and mass which could respond to variations in their external environment like electric and magnetic fields, and gravitational forces. Some or all these properties are constantly exploited in diverse research areas like atom interferometry [30–32], quantum simulations [33, 34]

and quantum computation [35], ultra-cold atoms in optical lattices [36], and atom beam focusing [37] and more.

## 1.1 Atom Interferometers

The wave-like behavior of both light and matter is a fundamental principle in physics. The key to this behavior is the ability of waves to demonstrate interference. This effect was demonstrated first for light in 1802 by Thomas Young [38] in a double-slit experiment. Over the intervening years and with the arrival of laser, light interferometers have been perfected and turned into indispensable measuring devices that have found applications in measurements of rotations, accelerations distance and atomic spectra. While light interferometers were reaching maturity, Louis de Broglie [39] put forward a hypothesis predicting the wave-like duality of matter. This hypothesis was proved in the electron diffraction experiment and later the neutron interference experiments of the 1940s. It was not until 1991 that interference by massive particles like atoms were demonstrated [40,41].

The difficulty in developing neutral atom interferometer was partly because atoms have large mass compared to that of say electron and results in a much smaller de Broglie wavelength for a given velocity. The very first atom interferometer [40] surmounted these challenges by working with streams of supersonic gaseous atoms and used mechanical gratings that were coherently illuminated by light. Subsequent experiments [41–46] used laser beams that provided a periodic potential, in place of the material and mechanical gratings, to split and recombine streams of gaseous atomic beams. Today, atoms are unprecedentedly controlled and manipulated using laser to achieve improved interference signals, high contrast ratio and precision measurements. They have been used to measure gravitational constant [47], acceleration [41,42], elec-

tric polarisability [48] and fine-structure constant [49] to very high accuracy.

The performance of atom interferometers depends on the interferometric time (the time interval within which the phase of the propagating atoms is predictable) and improves with increase in the interferometric time. The current interferometric times of free-space atom interferometers are less than one-tenth of a second and are limited by sagging of the atomic beam due free falling of atoms in the gravitational field. This problem is solved by the use of atomic fountain [50] that increases the physical size of the interferometer at the expense of the portability of the device and requires very sensitive technical details for its operations. Because of the limitation of the atomic fountain, other techniques that could hold atoms against gravity throughout the period of the interferometric time without compromising the portability of the device are desired. An example of such technique is the use of a confining trap to hold the atoms against gravity while the atoms are being manipulated. Condensates are well-suited for use in this technique because they have very small momentum that allows them to be confined to a small region in space.

Such BEC-based atom interferometers have been realised in trapped atom interferometer [30,51,52] and guided-wave interferometer [31,32,53]. The interferometric time of these interferometers is often limited by the techniques used in the manipulation of the cloud, the spatial inhomogeneity of the trap and the atom-atom interactions within the cloud.

### 1.1.1 Trapped-atom interferometer

For instance in trapped atom interferometers [30,51,52], a cloud of condensate, which is in the lowest mode in a single well trap and is sitting at the center of a trap, is dynamically split into two clouds in real space by deforming a single well potential into double well potential. During the splitting process, a weak confinement along

the axis transverse to the deformation allows states other than the ground state to be occupied thereby causing instability [54] within the condensate that limits the interferometric time of the condensate [30, 55]. The method was improved upon in subsequent experiments [51, 52] by providing tighter confinement along the axis transverse to the deformation and achieved an interferometric time of 200 ms [52]. However, it [52, 56, 57] was reported that atom-atom interactions still limited the interferometric time. More so, the recombination process is very sensitive to the phase due to atom-atom interactions. This is because merging the condensate with opposite phase cause excitations within the condensate which lead to exponential growth of the unstable modes [58]. To avoid this problem, the trap is switched off allowing the condensate to fall, undergo ballistic expansion under the influence of the of the atom-atom interactions which decrease the atomic density before the overlap and interfere.

### 1.1.2 Guided-wave atom interferometer

Parallel to the development of trapped-atom interferometers, guided-wave atom interferometers that use potentials to guide the motion of atomic wave packets were developed. Examples of guided-wave atom interferometers are the atom Michelson interferometer [31] and the atom Mach-Zehnder interferometer [32]. In these interferometer, the dynamic splitting of condensate in momentum space is used to manipulate the condensate in the guide.

In atom Michelson interferometer shown in Fig. 1.1 (called so because the splitting and recombination take place at the same spatial location), the BEC cloud  $\psi_0$  is initially at rest in a wave guide. Splitting pulses consisting of a pair of counterpropagating laser beams detuned from atomic resonance and acting as a diffraction grating are incident on the cloud. These pulses split the condensate into two harmonics,  $\psi_+$

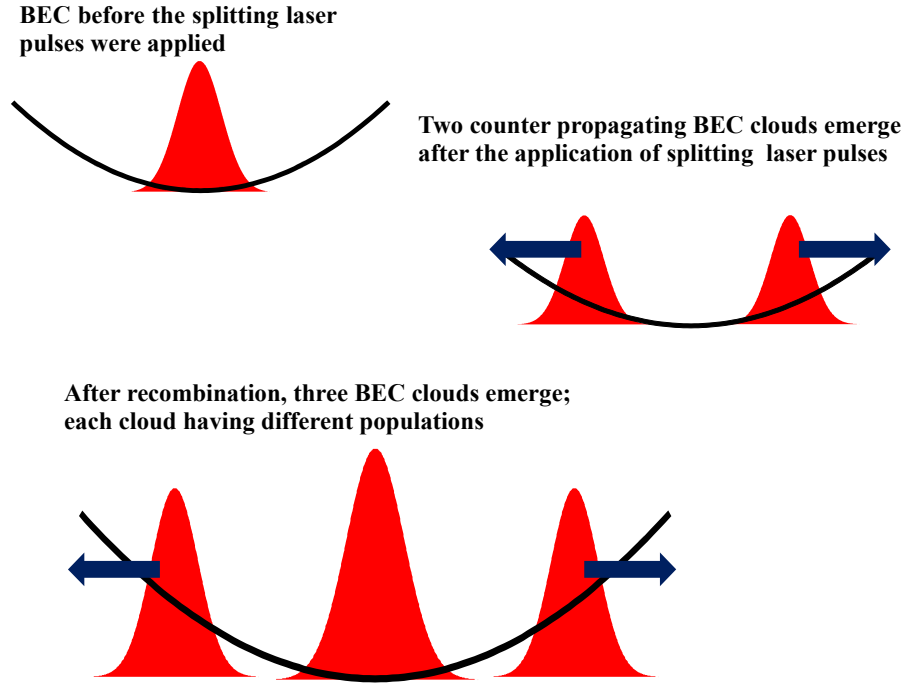


**Figure 1.1** Schematic of the evolution of BEC atomic cloud in an atom Michelson interferometer. The arrows in the figure indicate the direction of motion.

and  $\psi_-$ , moving with the initial velocities  $\pm v_0$ , respectively as shown in Fig 1.1. In a single reflection interferometers, the directions of propagation of these harmonics are reversed at time  $T/2$  (where  $T$  is the duration of the interferometric cycle), i.e., in the middle of the cycle with the help of a reflection pulse. The harmonics are then allowed to propagate back and are recombined when they overlap again using the same optical pulses that were used to split the original BEC cloud. After the recombination, the condensate is in general in a superposition of  $\psi_0$ ,  $\psi_+$  and  $\psi_-$  with the relative amplitudes depending on the amount of the accumulated phase shift between the arms of the interferometer acquired during the cycle.

In double reflection interferometer [53, 59], the optical reflection pulse is applied



twice at times  $T/4$  and  $3T/4$ . After the first reflection pulse, the harmonics change their direction of propagation and start moving back. They pass through each other, and exchange their positions by the time  $3T/4$ . The harmonic that was on the right at  $T/2$  is now on the left and vice versa. The second reflection pulse is applied at  $3T/4$  again reverses the direction of the propagation of the harmonics and, finally they are recombined at time  $T$ .

Also interferometric geometry that does not rely on the reflecting optical pulses but instead uses gradient of the confining waveguide potential for reversing direction of propagation of the BEC harmonics have been investigated. In this “free oscillation” interferometer [59–61], the moving BEC clouds propagate in a parabolic confining potential. They slow down as they climb the potential, stop at their classical turning points after one quarter of the trap period ( $T/4$ ) has elapsed, and turn back. At  $T/2$  the clouds meet at the bottom of the potential, reach again their turning points at  $3T/4$  and are recombined at time  $T$ . The duration of the interferometric cycle is thus equal to the oscillation period of the parabolic longitudinal waveguide potential  $T$ .

Similarly, the Mach-Zehnder-type interferometer using BEC has been experimentally demonstrated [32,60]. Compared to Michelson-type interferometer, the splitting technique is different; one of the two counter-propagating waves used to form the  $\pi/2$  splitting pulses is frequency-shifted with respect to the other thereby resulting in a traveling optical potential. The  $\pi/2$ -pulses transform the BEC originally at rest at the center of the trap into clouds of equal amplitude. One of the clouds remains at rest and the other travels with velocity  $v$ . A  $\pi$ -pulse applied at the mid-cycle stops the moving cloud and sets the stationary cloud into motion. At the end of the cycle, a  $\pi/2$ -pulse is used to recombine the two clouds. These experiments recorded a coherence time of 59ms and 97ms.

Both atom-atom interactions and spatially inhomogeneous trapping potential in-

duce decoherence on the condensate that separate after diffraction. These decoherence mechanisms work in tandem to limit the interferometric time and have been studied both experimentally [59,60] and theoretically [62–64]. For instance, experiments with BEC in Michelson interferometer [31] that were realized in a parabolic potential with radial frequency of 177 Hz, and axial frequency of 5 Hz had a coherence time of only 10 ms. The short coherence time was explained [62,63] to be caused by atom-atom interactions and the residual potential along the waveguide. To improve on these findings, subsequent experiments [53,59] used a more flat and symmetric parabolic potential whose frequencies are (6, 1.1, 3.3) Hz to confine and guide the atoms when compared to the first experiment [31]. In the experiments, the coherence time of the interferometer increased to 44 ms (71 ms) which is about 4 (7) times the first experiment [31]. In another experiment by the same group [59], the condensate was allowed to evolve freely after the splitting pulses were applied; the interferometer does not rely on the reflection pulses but relies on the gradient of the confining potential to reverse the direction of propagation of the clouds. The coherence time achieved in the experiment was 0.91 s. Despite the success in describing the decoherence resulting from atom-atom interactions and spatial inhomogeneous trapping potential within mean-field theory, the studies [59,60,62–64] could not account for atom-atom interactions within each condensate after diffraction, often called phase diffusion, because mean-field theory that was used in the formulation of the problem is incapable of describing the many-body effects which is addressed in this thesis.

## 1.2 Outline of this Thesis

The focus of this thesis is on controlling the spatial phase and phase diffusion in guided-wave atom interferometers in order to increase the interferometric time. At

---

first in Chapter 2, the diffraction techniques used in the manipulation of condensate is described. This is followed by a semiclassical statistical description of condensation. Finally the non-linear Schrodinger wave equation that describes the condensate is derived and discussed. In Chapter 3, the phase diffusion of split condensate is analysed by deriving the equation for the probability of observing any population of atoms in the output of the interferometer and investigate the characteristic features of the probability. The interferometric fringe contrast is then optimized within the experimentally-controlled parameter space for performance. Finally in Chapter 4, the combined effect of spatial phase and phase diffusion of split condensate is investigated by deriving the probability of observing any population of atoms in the output of the interferometer. The probability is analysed in various limiting cases and the corresponding averages are derived and analysed. Also the interference fringe contrast is optimised and then discussed.

# Chapter 2

## Tools of the trade

This chapter begins with the description of the physics behind the diffraction of atomic beam using laser pulses. Two diffractions schemes - Raman pulses and Bragg diffraction - are discussed. Special attention is paid to the diffraction of atomic beam using square-wave Bragg pulses as this technique is used for most part of this thesis. This is followed by a brief semiclassical statistical description of condensation in Sec. 2.2. Finally, the non-linear Schrodinger wave equation that describes the condensate is derived and briefly discussed in Sec. 2.3.

### 2.1 Diffraction of atoms by light

Large arm separation in atom interferometry allows each arm of the interferometer to be addressed separately by fields and helps reduce the effects from stray fields. It is achieved by beam splitters that would put the atomic wave packets into superposition of very narrow momentum distributions. The narrow momentum distributions are necessary for obtaining good fringe contrast. There are two techniques to achieve arm separation with atomic beams.

One method [41] uses a laser beam that causes atomic wave packets to be in different internal state and external motional state. The method exploits Raman transitions between two hyperfine ground states of an atom, which has very long lifetime compared with the duration of the experiment, via a third quasi-excited state. The pulses often called Raman pulses, consist of two light beams with different frequencies  $\omega_{L1}$  and  $\omega_{L2}$ . They are superposed together to form a traveling wave and are applied in  $\pi/2 - \pi - \pi/2$  sequence. The first  $\pi/2$ -pulse excites some population of atoms in an atomic beam initially in the internal state  $|1\rangle$  with momentum  $p$  when photons are absorbed from the laser beam with wave vector  $\kappa_{L1}$ . The population of atoms in the excited state is stimulated by the second laser beam with wave vector  $\kappa_{L2}$  to make transition to the other hyperfine ground state  $|2\rangle$ . Since the frequency of the absorbed and emitted photons are different, the population in state  $|2\rangle$  gains momenta  $2\hbar\kappa$  in the direction of the laser beams, where  $\kappa$  is the difference between the two wave vectors  $\kappa_{L1}$  and  $\kappa_{L2}$ . Thus the  $\pi/2$  pulse produces superposed states  $|1\rangle$  and  $|2\rangle$  moving with momentum  $p$  and  $p + 2\hbar\kappa$  respectively. The second pulse sequence,  $\pi$  pulse, swaps the two states and their respective momentum. Since the manipulation of the internal states of the atom involves the two ground state energy levels at different frequencies, the whole process discussed so far is inelastic because not all photon energy absorbed from one beam is re-emitted into the other beam.

Another method [46, 65, 66] uses light standing wave to diffract atomic clouds. The light standing wave is formed using a laser beam that is detuned from atomic resonance, to avoid spontaneous emission, and is retro-reflected by a mirror. Diffraction of atomic beam by standing light wave is understood by observing its effect on motional state of an atom within the atomic beam. An atom with momentum  $p$  that is incident on the standing light wave, would absorb a photon of momentum  $\hbar\kappa_l$  from one of the light beams and it is put in a quasi-excited state. The atom decays back

to the ground state by emitting a photon with the same wave vector into the counter propagating laser beam via stimulated emission and is deflected with a net momentum change of  $p + 2\hbar\kappa_l$ . However, an atom which absorbed a photon from same beam and re-emitted it into the same beam through stimulated emission will continue to be in its external motional state. Thus standing light wave, which presents periodic potential equivalent to material gratings to an atomic beam, coherently splits the atomic beam to form superposed states, thereby creates distinct paths in space. Because all the photon energy absorbed in one cycle is re-emitted in another cycle by the atom, the process is elastic. Since the diffraction of atomic beam by standing light waves is analogous to electron diffraction by crystals, the dependence of the scattering angle on the wavelength of the laser light and the de Broglie wavelength of the atoms makes it possible to align the standing light waves parallel to each other such that a closed path is obtained. Bragg diffraction technique has been used to split and recombine atomic BEC cloud in a number of experiments [31, 53, 59]. Standing wave formed from laser beams that are detuned from atomic resonance acts a periodic potential and plays the role of gratings for atomic beam with spacing  $d = \lambda_{\text{laser}}/2$ . Atomic beams with deBroglie wavelength  $\lambda_B = h/p$  that are comparable to the spacing of the optical light gratings are diffracted by the light standing wave.

### 2.1.1 Bragg diffraction of atoms by light

The discussion below follows closely that of B. Young *et al.* in Ref. [67]. Considered here is the case where the light frequency is far detuned from the atomic resonance so that spontaneous emission can be neglected. The evolution of the system (atom + field) can be described by Schrodinger wave equation where both atom and field are treated as waves.

The Hamiltonian of an atom coupled to the electromagnetic field in the absence

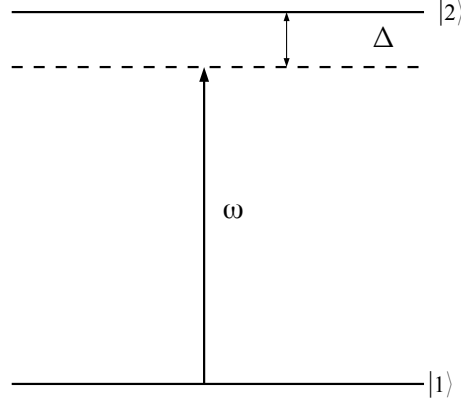


**Figure 2.1** Two-level atom with the ground state  $|1\rangle$  and excited state  $|2\rangle$  is coupled by the laser of frequency  $\omega$  that is detuned from resonance.  $\Delta$  is the detuning frequency defined in the text.

of spontaneous emission is given by

$$H = \frac{\mathbf{p}^2}{2m} + \hbar\omega_1 |1\rangle \langle 1| + \hbar\omega_2 |2\rangle \langle 2| - \mathbf{d} \cdot \mathbf{E}, \quad (2.1)$$

where  $\mathbf{p}$  is the atomic momentum,  $m$  is the mass of the atom,  $\mathbf{d}$  is the electric dipole moment,  $\mathbf{E}$  is the light field,  $\omega_{1,2}$  is the frequency of the states  $|1\rangle$ ,  $|2\rangle$  shown in Fig. 2.1. Here the particle momentum is neglected simply because the atoms in the BEC cloud are initially at rest so that  $\mathbf{p} = 0$ . Consider an atom that is in light field of the form

$$\mathbf{E} = \mathbf{E}_0(x, t) \cos(\omega t + \phi_L), \quad (2.2)$$

where  $\mathbf{E}_0(x, t) = \mathbf{E}_0(t) \cos(\kappa_L x)$  is the amplitude of the standing light field,  $\omega$  is the frequency of the light field,  $\phi_L$  is the phase of the laser beam. The light field couples two of its internal states as shown in Fig. 2.1 through dipole interaction. The time evolution of the state vector of the system at any time

$$|\psi(t)\rangle = a_1(t) |1\rangle + a_2(t) |2\rangle, \quad (2.3)$$

is given by the Schrodinger equation

$$i\hbar \frac{d}{dt} |\psi(t)\rangle = H |\psi(t)\rangle. \quad (2.4)$$

Substituting the state vector Eq. (2.3) in the Eq. (2.4) reduces to a coupled differential equations for the coefficients

$$\begin{aligned} i\hbar \dot{a}_1(t) &= \hbar\omega_1 a_1(t) + V_{21} a_2(t), \\ i\hbar \dot{a}_2(t) &= V_{21}^* a_1(t) + \hbar\omega_2 a_2(t), \end{aligned} \quad (2.5)$$

where

$$V_{12} = \hbar\Omega_{21} \frac{e^{i(\omega t + \phi_L)} + e^{-i(\omega t + \phi_L)}}{2}, \quad (2.6)$$

and the Rabi frequency is defined as

$$\Omega_{21} = -\frac{\langle 2 | \mathbf{d} \cdot \mathbf{E}_0(x, t) | 1 \rangle}{\hbar}. \quad (2.7)$$

The term  $V_{12}$  contains both fast and slow terms ( $e^{i\omega t}$ ,  $e^{-i\omega t}$ ). For instance, the component  $e^{-i\omega t}$  causes atoms in their ground state  $|1\rangle$  to undergo rapid oscillation whose effect on the state  $|1\rangle$  is zero on the average and vice versa. Making the following change of variables

$$\begin{aligned} a_1(t) &= c_1(t) e^{-i\omega_1 t - i\Delta t/2}, \\ a_2(t) &= c_2(t) e^{-i\omega_2 t + i\Delta t/2}, \end{aligned} \quad (2.8)$$

where  $\Delta = (\omega_2 - \omega_1 - \omega)$  and neglecting the term in  $V_{12}$  that oscillates rapidly, Eq. (2.5) become

$$\begin{aligned} i\dot{c}_1 &= -\frac{\Delta}{2} c_1 + \frac{\Omega_{21} e^{i\phi_L}}{2} c_2, \\ i\dot{c}_2 &= \frac{\Omega_{21}^* e^{-i\phi_L}}{2} c_1 + \frac{\Delta}{2} c_2. \end{aligned} \quad (2.9)$$



### 2.1.2 Atom diffraction using square-wave Bragg pulses

To solve the differential equations in Eq. (2.9),  $\Omega_{21}(x, t)$  is assumed to be constant when light beams are interacting with the atoms. This is true since in the experiments to be described in this work, square pulse large were used in the diffraction of the atomic BEC cloud.

Defining the following parameters [68]

$$\tan \theta = \frac{|\Omega_{21}|}{\Delta}, \quad \sin \theta = \frac{|\Omega_{21}|}{\Omega_r}, \quad \cos \theta = \frac{\Delta}{\Omega_r}, \quad (2.10)$$

where  $\Omega_r = \sqrt{\Delta^2 + \Omega_{21}^2}$  and  $0 < \theta < \pi$ , the eigenvalues  $\lambda$  of Eq. (2.9) are

$$\lambda_{\pm} = \pm \frac{\sqrt{\Delta^2 + \Omega_{21}^2}}{2}, \quad (2.11)$$

and the corresponding eigenvectors are

$$|\lambda_{-}\rangle = \begin{pmatrix} \cos\left(\frac{\theta}{2}\right) \\ -\sin\left(\frac{\theta}{2}\right) e^{-i\phi_L} \end{pmatrix}, \quad |\lambda_{+}\rangle = \begin{pmatrix} \sin\left(\frac{\theta}{2}\right) e^{i\phi_L} \\ \cos\left(\frac{\theta}{2}\right) \end{pmatrix}. \quad (2.12)$$

For a population of atoms that where initially in their ground state, then

$$\begin{aligned} a_1 &= e^{-i(\omega_1 + \Delta/2)t} (\cos^2 \theta/2 e^{-i\lambda_{-}t} + \sin^2 \theta/2 e^{-i\lambda_{+}t}) \\ a_2 &= \frac{\sin \theta}{2} e^{-i(\omega_2 - \Delta/2)t} (e^{-i(\lambda_{+}t + \phi_L)} - e^{-i(\lambda_{-}t + \phi_L)}). \end{aligned} \quad (2.13)$$

and the energies  $E_{1-} = \hbar(\omega_1 + \Delta/2 - \lambda_{-})$  and  $E_{1+} = \hbar(\omega_1 + \Delta/2 - \lambda_{+})$  associated with  $a_1$  i.e. the ground state are

$$\begin{aligned} E_{1-} &= \hbar \left[ \omega_1 + \frac{\Delta}{2} - \frac{1}{2} \sqrt{\Delta^2 + \Omega_{12}^2} \right], \\ E_{1+} &= \hbar \left[ \omega_1 + \frac{\Delta}{2} + \frac{1}{2} \sqrt{\Delta^2 + \Omega_{12}^2} \right], \end{aligned} \quad (2.14)$$

respectively.

In experiments [31, 53, 59], the detuning  $\Delta$  is controlled by the interaction frequency  $\omega$  of the laser light. For very large positive (red) detuning  $\Delta > 0$ ,  $\theta$  is approximately zero and the state vector of the system becomes  $\psi \approx e^{-iE_{1-}t/\hbar} |1\rangle$  where

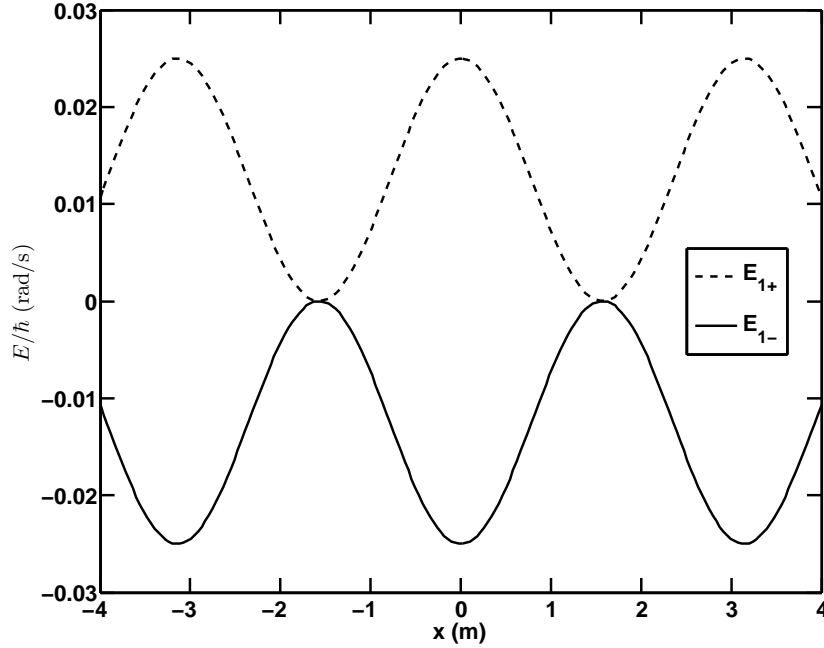


**Figure 2.2** The dressed state energies as a function of position in light standing wave. The detuning is  $|\Delta| = 10$  rad/s,  $\omega_1 = 0$  rad/s,  $\Omega = \cos(\kappa_L x)$  rad/s and  $\kappa_L = 1$  m $^{-1}$ . Depending on whether the detuning  $\Delta$  is positive or negative, the atoms follow either curve but never both.

$E_{1-} \approx \hbar \left( \omega_1 - \frac{1}{4} \frac{\Omega_{21}^2}{|\Delta|} \right)$ . Similarly for very large negative (blue) detuning  $\Delta < 0$ ,  $\theta$  is roughly equal to  $\pi$  and the state vector of the system is given as  $|\psi\rangle \approx e^{-iE_{1+}t/\hbar} |1\rangle$ , where  $E_{1+} \approx \hbar \left( \omega_1 + \frac{1}{4} \frac{\Omega_{21}^2}{|\Delta|} \right)$ . Notice that in either of the detuning considered, the atoms are always found in the ground state  $|1\rangle$  while the excited  $|2\rangle$  is unoccupied. The overall effect of the large detuned laser light is to shift the ground state energy level of the atoms up or down. It also present periodic potentials to the atoms since  $\Omega_{21} \sim \langle 2 | \mathbf{d} \cdot \mathbf{E}_0(t) | 1 \rangle \cos(\kappa_L x)$  which the ground state follows adiabatically as shown in Fig. 2.2. Then, the Schrodinger wave equation for the ground state in terms of the

potential  $\Omega(x, t)$  is

$$i\frac{d}{dt}\psi_g = -\frac{\hbar}{2m}\frac{d^2}{dx^2}\psi_g + \Omega(t)\cos(2\kappa_L x)\psi_g. \quad (2.15)$$

As observed in experiments [31,53], the atomic distribution after diffraction shows a series of very narrow peaks in the momentum space. This is explained by the optical potential  $\Omega(t)\cos 2\kappa_L x$  that presents a grating of periodicity  $\lambda_L/2$  to the atoms, where  $\kappa_L$  and  $\lambda_L$  are the wave number and the wavelength of the laser beam respectively. The periodicity of the gratings has a characteristic width of  $2\hbar\kappa_L$  in the momentum space. The Bragg condition for such grating is

$$p = 2n\hbar\kappa_L \quad (2.16)$$

where  $n$  is the diffraction order and takes integer values only,  $p$  is the momentum of the atom and  $\kappa_L$  is the wave vector of the laser beam. It is then instructive to expand the ground state wave function  $\psi_g(x, t)$  in the Fourier space

$$\psi_g(x, t) = \sum_{n=-\infty}^{\infty} \phi_n(x, t) e^{2n\kappa_L x}. \quad (2.17)$$

Substituting Eq. (2.17) in the Schrodinger equation Eq. (2.15) gives

$$i\dot{\phi}_n = \frac{\hbar(2n\kappa_L)^2}{2m}\phi_n + (\phi_{n-1} + \phi_{n+1})\frac{\Omega(t)}{2} \quad (2.18)$$

where the dispersion and relative displacement terms have been neglected because when the laser pulses are on, the lattice potential energy and the particles kinetic energy dominates every other dynamics. Defining the terms  $\hbar(2\kappa_L)^2/(2m) = \omega_{rec}$  the recoil frequency of the atom and a dimensionless time  $\tau = 2\omega_{rec}t$ , the coupled equations become

$$i\dot{\phi}_n = \frac{n^2}{2}\phi_n + (\phi_{n-1} + \phi_{n+1})\frac{\omega(t)}{2}, \quad (2.19)$$

where  $\omega(t) = \Omega(t)/(2\omega_{rec})$ . Eq. (2.19) comprises an infinite set of coupled differential equations. To be able to truncate the series, note that if the recoil energy of the atom

is greater than the atom-field interaction, then  $N$ th diffraction order and beyond cannot be excited (i.e.  $N^2 \gg \Omega/(2\omega_{rec})$  in order to truncate the series for diffraction orders less than  $N$ ,  $N$  is the largest order possible). To describe the lowest order diffraction  $n = 0, \pm 1$  only,  $N = 2$  [i.e.  $n = 0, \pm 1, \dots, \pm(N-1)$ ] and Eq. (2.19) gives three coupled differential equations

$$i \begin{pmatrix} \dot{\phi}_1 \\ \dot{\phi}_0 \\ \dot{\phi}_{-1} \end{pmatrix} = \frac{1}{2} \begin{pmatrix} 1 & \Omega & 0 \\ \Omega & 0 & \Omega \\ 0 & \Omega & 1 \end{pmatrix} \begin{pmatrix} \phi_1 \\ \phi_0 \\ \phi_{-1} \end{pmatrix} \quad (2.20)$$

The solution of Eq. (2.20) has the form

$$\begin{pmatrix} \phi_1 \\ \phi_0 \\ \phi_{-1} \end{pmatrix} = e^{-it/4} \begin{pmatrix} \phi_{11} & \phi_{12} & \phi_{13} \\ \phi_{12} & \phi_{22} & \phi_{12} \\ \phi_{13} & \phi_{12} & \phi_{11} \end{pmatrix} \begin{pmatrix} \phi_1(0) \\ \phi_0(0) \\ \phi_{-1}(0) \end{pmatrix} \quad (2.21)$$

where

$$\begin{aligned} \phi_{11} &= \frac{1}{2} \left[ e^{-it/4} + \cos \frac{qt}{4} - i \sin \frac{qt}{4} \right], \\ \phi_{12} &= 2i \frac{\Omega}{q} \sin \frac{qt}{4}, \\ \phi_{13} &= \frac{1}{2} \left[ \cos \frac{qt}{4} - e^{-it/4} - \frac{i}{q} \sin \frac{qt}{4} \right], \\ \phi_{22} &= \cos \frac{qt}{4} + \frac{i}{q} \sin \frac{qt}{4}, \end{aligned} \quad (2.22)$$

and  $q = \sqrt{1 + 8\omega^2}$ . This result was obtained in Ref. [63]. In order to excite the population of atoms in the stationary cloud (i.e. atoms in the zeroth harmonic) into moving clouds that have momentum  $\pm 2\hbar\kappa_L$  without exciting other higher motional states, a compound pulse of two square pulses is used. The first pulse of duration  $t = \sqrt{2}\pi$  and dimensionless frequency  $\Omega = \sqrt{1/8}$  put the system in a superposition of  $\phi_1$ ,  $\phi_0$ , and  $\phi_-$ . The first pulse is followed by a period of free evolution lasting for a time  $t = 2\pi$  during which the laser pulses are turned off and the clouds are allowed to

rephase. After the free evolution, a second pulse at the same dimensionless frequency and duration applied to the clouds completes the transfer of atoms from  $\phi_0$  to the harmonics  $\phi_1$  and  $\phi_{-1}$ . The sequence of the pulses described above is given by the splitting matrix,

$$A_{0\leftrightarrow\pm 1} = \begin{pmatrix} -\frac{1}{2}e^{-i\sqrt{2}\pi} & \frac{1}{\sqrt{2}}e^{-i\pi/\sqrt{2}} & \frac{1}{2}e^{-i\sqrt{2}\pi} \\ \frac{1}{\sqrt{2}}e^{-i\pi/\sqrt{2}} & 0 & \frac{1}{\sqrt{2}}e^{-i\pi/\sqrt{2}} \\ \frac{1}{2}e^{-i\sqrt{2}\pi} & \frac{1}{\sqrt{2}}e^{-i\pi/\sqrt{2}} & -\frac{1}{2}e^{-i\sqrt{2}\pi} \end{pmatrix}. \quad (2.23)$$

Similarly, the reflection pulses are used to reverse the momentum of the atoms in the moving clouds. The momentum reversal  $\phi_{\pm} \rightarrow \phi_{\mp}$  is achieved with a single reflection pulse of duration  $t = 4\pi$  and intensity  $\Omega = \sqrt{3/8}$ . The matrix that represents the momentum reversal is

$$A_{\pm\leftrightarrow\mp} = \begin{pmatrix} 0 & 0 & -1 \\ 0 & -1 & 0 \\ -1 & 0 & 0 \end{pmatrix}. \quad (2.24)$$

### 2.1.3 Atom diffraction using Raman pulses

In this diffraction technique, both the internal and the external states are exploited. This is achieved for zero detuning so that the solution of the coupled differential equation Eq. (2.9) becomes (see Chap. 7 of Ref. [69] )

$$\begin{pmatrix} a_1(t) \\ a_2(t) \end{pmatrix} = \begin{pmatrix} e^{-i\omega_1 t} \cos\left(\frac{\Omega t}{2}\right) & -ie^{-i\omega_1 t} \sin\left(\frac{\Omega t}{2}\right) e^{i\phi_L} \\ -ie^{-i\omega_2 t} \sin\left(\frac{\Omega t}{2}\right) e^{-i\phi_L} & e^{-i\omega_2 t} \cos\left(\frac{\Omega t}{2}\right) \end{pmatrix} \begin{pmatrix} a_1(0) \\ a_2(0) \end{pmatrix}. \quad (2.25)$$

A single pulse of duration  $t = \pi/(2\Omega)$  splits an atomic beam into two beams and put them in a linear superposition of their motional states. The matrix of the splitting pulse is

$$A_{1\leftrightarrow 1+2} = \frac{1}{\sqrt{2}} \begin{pmatrix} 1 & -ie^{i\phi_L} \\ -ie^{-i\phi_L} & 1 \end{pmatrix}. \quad (2.26)$$

Similarly a single pulse of duration  $t = \pi/\Omega$  acts as a mirror by reversing the momentum of atoms in the states  $c_1$  and  $c_2$  respectively. The matrix that represents the reflection pulse is

$$A_{1\leftrightarrow 2} = \frac{1}{\sqrt{2}} \begin{pmatrix} 0 & -ie^{i\phi_L} \\ -ie^{-i\phi_L} & 0 \end{pmatrix}. \quad (2.27)$$

## 2.2 Bose-Einstein condensation

Bosons are particles that like to stay together in the same state. When a system of bosons reach a critical temperature, it undergoes a phase transition and the particles occupies the lowest energy state in the system. This phenomenon is called Bose-Einstein condensation. The mechanism of Bose-Einstein condensation is understood from the semiclassical statistical description as discussed below [70, 71].

### 2.2.1 Critical temperature

The mean number of atoms occupying the  $i$ th state with energy  $\epsilon_i$  in a Bose-gas is given by

$$\langle n_i \rangle = \frac{1}{e^{\beta(\epsilon_i - \mu)} - 1}, \quad (2.28)$$

where  $\beta = (\kappa_B T)^{-1}$ ,  $k_B$  is the Boltzmann constant,  $T$  is the temperature and  $\mu$  is the chemical potential. The total number of atoms within the confining potential is given by

$$\begin{aligned} N &= N_0 + N_e, \\ &= N_0 + \sum_{i=1}^{\infty} \frac{1}{e^{\beta(\epsilon_i - \mu)} - 1}, \end{aligned} \quad (2.29)$$

where  $N_0$  is the number of atoms in the ground state and  $N_e$  is the number of atoms in the excited state. For an isotropic harmonic oscillator,

$$\epsilon_{n_x, n_y, n_z} = \hbar\omega(n_x + n_y + n_z + 3/2), \quad (2.30)$$

and

$$N_e = \sum_{n_x, n_y, n_z \neq 0}^{\infty} \frac{1}{e^{\hbar\omega\beta(n_x+n_y+n_z+3/2)-\beta\mu} - 1}. \quad (2.31)$$

Let  $n_x + n_y + n_z = m$  and  $\alpha = -\beta\mu + \frac{3}{2} \frac{T_0}{TN^{1/3}}$  where

$$T_0 = \frac{\hbar\omega N^{1/3}}{k_B}. \quad (2.32)$$

The sum in Eq. (2.31) can be reduced to one variable sum over  $m$

$$N_e = \sum_{m=1}^{\infty} \frac{m^2/2 + 3m/2 + 1}{e^{\frac{T_0}{TN^{1/3}} + \alpha} - 1}. \quad (2.33)$$

When  $N$  is large, the states becomes more closely spaced and the sum can be replaced by an integral to a good approximation. Making the transformation  $m \rightarrow m + 1$  and using Eq. (23.1.30) of Ref. [72],  $N_e$  becomes [70, 71]

$$N_e \approx N\zeta(3) \left(\frac{T}{T_0}\right)^3, \quad (2.34)$$

where  $\zeta(n)$  is the Riemann  $\zeta$  function. Using Eq. (2.29), the fractional population of atoms in the ground state for temperature ( $T$ ) less than the critical temperature ( $T_c$ ) is

$$\frac{N_0}{N} = 1 - \zeta(3) \left(\frac{T}{T_0}\right)^3. \quad (2.35)$$

In the limit  $N_0 \rightarrow 0$ , the critical temperature is

$$k_B T_c = \hbar\omega \left(\frac{N}{\zeta(3)}\right)^{1/3} = 0.94\hbar\omega N^{1/3}. \quad (2.36)$$

For temperature greater than the critical temperature, the population of atoms in the ground state is of the order unity instead of the order  $N$ .

### 2.2.2 Critical phase space density

The total number of atoms in the excited state can be evaluated from the density distribution. In the limit  $T > T_c$ ,

$$N_e = \int dr n(\mathbf{r}) \quad (2.37)$$

where

$$n(\mathbf{r}) = \frac{1}{(2\pi\hbar)^{-3}} \int \frac{d\mathbf{p}}{e^{\beta[\epsilon(\mathbf{r},\mathbf{p})-\mu]} - 1} \quad (2.38)$$

where  $\epsilon(\mathbf{r}, \mathbf{p}) = p^2/2m + V_{\text{ext}}(\mathbf{r})$  is the semiclassical energy in the phase space [71].

Upon evaluation of the integral,  $n(\mathbf{r})$  becomes

$$n(\mathbf{r}) = \frac{1}{\Lambda_T^3} g_{3/2}(e^{\beta(\mu-V(\mathbf{r}))}), \quad (2.39)$$

where  $g_\nu(x) = \sum_{k=1}^{\infty} \frac{x^k}{k^\nu}$  is the polylogarithm function and  $\Lambda_T$  is the thermal de Broglie wavelength defined as

$$\Lambda_T = \sqrt{\frac{2\pi\hbar^2}{mk_B T}}. \quad (2.40)$$

Bose-Einstein condensation occurs when the interparticle spacing  $n^{-1/3}$  becomes comparable to the thermal de Broglie wavelength  $\Lambda_T$  and the individual particle can no longer be distinguished. This condition is equivalent to stating that the phase space density  $n\Lambda_T^3$  is greater than unity. This condition is met at  $T = T_c$  when the atoms macroscopically occupy the lowest energy ( $\epsilon_{\text{min}}$ ) level of the potential  $V(\mathbf{r})$  and chemical potential for adding a particle within the minimum energy level of the potential  $V(\mathbf{r})$  is equal to  $\epsilon_{\text{min}}$  (i.e.  $\mu - \epsilon_{\text{min}} = 0$ ) so that  $e^{\beta(\mu-\epsilon_{\text{min}})}$  becomes unity. The phase space density then reaches its maximum value

$$n\Lambda_T^3 = 2.612, \quad (2.41)$$

and corresponds to a phase transition point in a Bose gas.

The presence of BEC is indicated by the appearance of a peak in the velocity distribution of the atoms as shown in Fig 2.3. The critical temperature for BEC of alkali atoms to appear in dilute gas trapped in magnetic trap is  $T_c \sim 100$  nK. In experiment that realised BEC using  $^{87}\text{Rb}$  [9], the condensation started at 170 nK, and the BEC had a lifetime of about fifteen seconds.



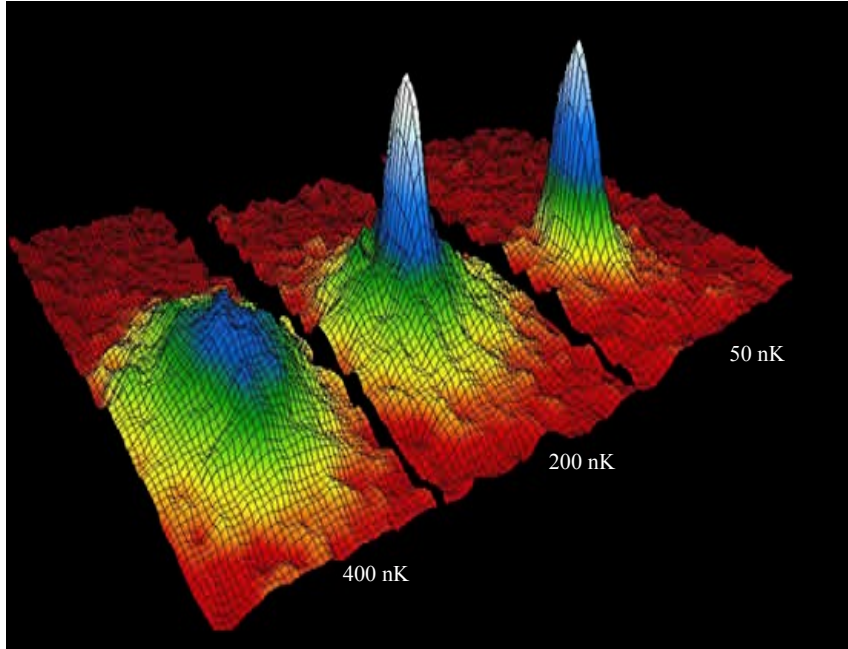


**Figure 2.3** Velocity distribution of an ensemble of atoms trapped in a magnetic optical trap at different temperatures, from hot (left) to cold (right). As the atoms begin to condense in the ground state of the trap, the velocity distribution of the atomic ensemble exhibits a peak at zero velocity (image from [jila.colorado.edu/bec](http://jila.colorado.edu/bec)).

## 2.3 Gross-Pitaevskii equation

At condensation, most atoms in a Bose gas occupy the lowest energy state of the system. In the limit where the population of the background thermal atoms are small and negligible, most of the atoms are in the condensate and the wave function of the many-particle system may be written to an approximation as a product of a single-particle state  $\psi(\mathbf{r}, t)$  (See Sec.6.1 of Ref [73])

$$\Psi(\mathbf{r}_1, \mathbf{r}_2, \mathbf{r}_3, \dots, \mathbf{r}_N, t) = \psi(\mathbf{r}_1, t)\psi(\mathbf{r}_2, t) \cdots \psi(\mathbf{r}_N, t). \quad (2.42)$$

The Lagrangian [74] corresponding to the state Eq. (2.42) is given by

$$L = N \int d\mathbf{r} \left\{ i\hbar\psi^* \frac{\partial\psi}{\partial t} - \frac{\hbar^2}{2m} \nabla\psi^* \nabla\psi - \psi^* V(\mathbf{r}) - \frac{N-1}{2} U_0 |\psi|^4 \right\}, \quad (2.43)$$

where  $\psi = \psi(\mathbf{r}, t)$ ,  $U_0 (=4\pi\hbar^2 a_s/m)$ ,  $V(\mathbf{r})$  is the external potential experienced by the atoms,  $m$  is the mass of atom in the condensate and  $a_s$  is the s-wave scattering length. According to Hamilton's principle, the true evolution of the state Eq. (2.42) is one for which variations in the Lagrangian Eq. (2.43) corresponding to it is stationary (i.e.  $\delta L = 0$ ). Using integration by parts and treating  $\psi$  and  $\psi^*$  as two independent fields, the variation of the Lagrangian is

$$\begin{aligned} \delta L = N \int d\mathbf{r} \delta\psi^* \left\{ i\hbar \frac{\partial\psi}{\partial t} + \frac{\hbar^2}{2m} \nabla^2 \psi - V(\mathbf{r})\psi - (N-1) U_0 |\psi|^2 \psi \right\} \\ - N \frac{\hbar^2}{2m} \delta\psi^* \nabla\psi, \end{aligned} \quad (2.44)$$

where  $\delta\psi = 0$  has been used. Requiring that variation in Lagrangian be stationary, implies that  $\delta\psi^* \nabla\psi|_i^f = 0$  so that the constant term vanishes at the boundary and

$$i\hbar \frac{\partial\psi}{\partial t} = -\frac{\hbar^2}{2m} \nabla^2 \psi + V(\mathbf{r})\psi + (N-1) U_0 |\psi|^2 \psi \quad (2.45)$$

Equation (2.45) is called the time-dependent Gross-Pitaevskii equation and describes accurately the behaviour of condensate at very low temperature  $T < T_c$ , provided that the background thermal atoms are negligible.

### 2.3.1 Thomas-Fermi approximation

Equation (2.45) is a nonlinear differential equation with cubic nonlinearity in  $\psi(\mathbf{r}, t)$ .

Consider a parabolic potential of the form

$$V(\mathbf{r}) = \frac{m}{2} (\omega_x^2 x^2 + \omega_y^2 y^2 + \omega_z^2 z^2). \quad (2.46)$$

To bring out the features of the Gross-Pitaevskii equation the original work of Ref. [75] is followed. Equation (2.45) is rescaled using the following characteristic scales: the

characteristic length  $R_c = (4\pi N a_{\text{os}}^4 a_{\text{sc}}) = a_{\text{os}} \zeta$ , a dimensionless scale  $\zeta = (4\pi N a_{\text{sc}}/a_{\text{os}})^{1/5}$ , oscillator length  $a_{\text{os}} = \sqrt{\hbar/m\omega}$  and the characteristic time scale  $T_c = (\omega\zeta^2)^{-1}$ , where  $\omega = (\omega_x\omega_y\omega_z)^{1/3}$  is the geometric mean frequency of the external trapping potential. Defining a dimensionless length  $\eta = \mathbf{r}/R_c$ , a dimensionless time  $\tau = t/T_c$  and dimensionless wave function  $\psi(\eta, \tau) = (R_c)^{3/2} \psi(\mathbf{r}, t)$ , Eq. (2.45) becomes

$$i \frac{\partial \psi(\eta, \tau)}{\partial \tau} = \left[ -\frac{1}{2\zeta^4} \nabla_\eta^2 + \frac{\eta^2}{2} + |\psi(\eta, \tau)|^2 \right] \psi(\eta, \tau). \quad (2.47)$$

In the limit  $\zeta \ll 1$  (that is  $N a_{\text{sc}}/a_{\text{os}} \ll 1$ ), the  $\zeta^{-4}$  term is large compared to the cubic term in  $\psi$ . The cubic term is then treated as a perturbation to the harmonic oscillator problem. In the opposite limit when there are large number  $N$  of atoms in the condensate,  $\zeta \gg 1$  and the cubic term dominates. The term having  $\zeta^{-4}$  dependence is very small and is treated as a correction. Equation (2.47) then becomes

$$i \frac{\partial \psi}{\partial \tau} = \left[ \frac{\eta^2}{2} + |\psi|^2 \right] \psi. \quad (2.48)$$

The neglect of the  $\zeta^{-4}$  term in Eq. (2.47) is referred to as Thomas-Fermi approximation [71, 75]. Assuming a stationary state solution of the form  $\psi \sim \exp(-i\tilde{\mu}\tau) \psi(\eta)$  where  $\tilde{\mu}$  is the dimensionless chemical potential defined as  $\tilde{\mu} = \mu (\hbar\omega\zeta^2)^{-1}$ , Eq. (2.48) becomes

$$\tilde{\mu} \psi(\eta) = \left[ \frac{\eta^2}{2} + |\psi(\eta)|^2 \right] \psi(\eta). \quad (2.49)$$

Equation (2.49) has a solution

$$n(\eta) = |\psi(\eta)|^2 = \tilde{\mu} - \frac{\eta^2}{2} \quad (2.50)$$

in the region where the right hand side is positive and the density  $n(\eta)$  is zero outside this region. The boundary of the condensate is then given by the balance between the parabolic potential and interactions within the condensate and is given by  $\tilde{\mu} = \frac{\eta^2}{2}$ . The radius of the cloud in three dimensions is given by  $R = \sqrt{2\tilde{\mu}}$ , where dimensionless

chemical potential  $\tilde{\mu}$  is determined from the normalisation  $\int |\psi|^2 d\eta = 1$  and gives

$$\tilde{\mu} = \left( \frac{15}{2^{9/2}\pi} \right)^{2/5}, \quad (2.51)$$

from which the chemical potential  $\mu$  is determined as

$$\mu = \frac{\hbar\omega}{2} \left( 15 \frac{Na_{\text{sc}}}{a_{\text{os}}} \right)^{2/5}. \quad (2.52)$$

# Chapter 3

## Phase diffusion of Bose-Einstein condensate

An atom in real condensate interacts with other atoms when it is in close proximity to another atom via the dipole-dipole interaction between the two atoms. Because the interaction is pairwise it often called two-body or atom-atom interaction. Atom-atom interactions are useful in the formation of condensate by providing thermalisation for the cold atoms during evaporative cooling.

However, the same two-body interaction is detrimental to the operation of atom interferometers. It gives rise to random fluctuation in the phase called phase diffusion [56, 57, 76]. At the beginning of interferometric cycle, the system is in a mode-entangled state with each cloud being in a linear superposition of number states. The presence of atom-atom interactions cause each number state to evolve at different rate that results in the accumulation of relative time-dependent phase shift between the different number states. Recombining the clouds at the end of interferometric cycle gives a random fluctuation in the atomic populations of the clouds observed at the end of cycle. In order to beat the phase diffusion in atom interferometers using

BEC, the atom-atom interactions in the condensate are exploited and used to create squeezed states [29, 52, 77]. By slowly raising the barrier height [29, 78, 79] of the trapping double-well potential to frustrate tunneling of atoms between the well sites an entangled squeezed state that has equal number of atoms on the average is formed. Also entangled squeezed states are created by using state dependent potential [80] or Feshbach resonance [81] to manipulate the two-body interactions between different internal states of condensate population.

This chapter focuses on analysing the effect of phase diffusion on the population of atomic BEC in guided-wave atom interferometers. The remainder of the chapter is organised as follows. In Sections 3.1 and 3.2, the state vector at the end of the interferometric cycle is derived for Michelson and Mach-Zehnder interferometers respectively. The probability of observing any number of atoms in the output ports of either interferometer is derived in Sec. 3.3. Effects of phase diffusion on the features of the probability density of observing any number of atoms in the output ports of either interferometer is analysed in Sec. 3.4 and its implication for experiments is discussed in Sec. 3.5. Finally, the results presented in this chapter has been published [82] and is included in the Appendix A

## 3.1 Atom-Michelson interferometer

Two counter-propagating laser pulses incident on the a cloud at rest splits the cloud into two clouds that move in opposite directions with velocity  $\pm v_0$  as previously described in Sec. 1.1.2. During the clouds' evolution, atoms in each cloud accumulate phase due to the external potential and atom-atom interactions. The many-body Hamiltonian describing the atomic BEC in the presence of an external potential  $V$  is

$$\hat{H}(t) = \int d^3\mathbf{r} \hat{\Psi}^\dagger \left[ -\frac{\hbar^2}{2m} \nabla^2 + V + \frac{U_0}{2} \hat{\Psi}^\dagger \hat{\Psi} \right] \hat{\Psi}, \quad (3.1)$$

where  $M$  is the atomic mass  $U_0 = 4\pi\hbar^2 a_s M^{-1}$  is the strength of the two-body interaction within the condensate,  $a_s$  is the s-wave scattering length,  $\hat{\Psi}^\dagger, \hat{\Psi}$  are the creation and annihilation field operators respectively, which at a given time  $t$  create or annihilate atom at position  $\vec{r}$ . Introducing the bosonic creation  $b_k^\dagger$  and annihilation  $b_k$  operator  $k = \pm$  in each cloud, the field operator  $\hat{\Psi}$  is represented in the basis of  $\psi_\pm$

$$\hat{\Psi} = b_+ \psi_+ + b_- \psi_-, \quad (3.2)$$

where  $\psi_\pm$  are the eigenfunctions of the BEC clouds moving to the right and to the left respectively, and the normalisation condition

$$\int d\mathbf{r} \psi_\pm^* \psi_\pm = 1, \quad (3.3)$$

and are not overlapping for the entire time of the interferometric cycle. The wave functions  $\psi_\pm$  are solutions of the two coupled Gross-Pitaevskii equations given in Eq. (9) of Ref. [63]. Substituting Eq. 3.2 into the Hamiltonian (3.1) gives the following

$$\begin{aligned} \hat{H} &= \frac{1}{2}(\varepsilon_+ + \varepsilon_-)(b_+^\dagger b_+ + b_-^\dagger b_-) + \frac{1}{2}(\varepsilon_+ - \varepsilon_-)(b_+^\dagger b_+ + b_-^\dagger b_-) \\ &+ g \left( b_+^\dagger b_+^\dagger b_+ b_+ + b_-^\dagger b_-^\dagger b_- b_- \right), \end{aligned} \quad (3.4)$$

where

$$\varepsilon_+ = \int d^3\mathbf{r} \psi_+^* \left( -\frac{\hbar^2}{2m} \nabla^2 + V \right) \psi_+, \quad (3.5)$$

$$\varepsilon_- = \int d^3\mathbf{r} \psi_-^* \left( -\frac{\hbar^2}{2m} \nabla^2 + V \right) \psi_-, \quad (3.6)$$

$$g = \frac{U_0}{2} \int d^3\mathbf{r} \psi_\pm^* \psi_\pm^* \psi_\pm \psi_\pm. \quad (3.7)$$

Using the bosonic commutation algebra of the creation and annihilation operators  $[b_j, b_k^\dagger] = \delta_{jk}$ ,  $[b_i, b_j] = 0$  and the total number operator of the two clouds  $\hat{N}$  ( $=$

$\hat{n}_+ + \hat{n}_-$ ), where  $\hat{n}_k = b_k^\dagger b_k$ , the Hamiltonian (3.4) is re-arranged and one writes

$$\hat{H}_{\text{eff}} = \frac{W}{2} (\hat{n}_+ - \hat{n}_-) + \frac{g}{2} \left[ \hat{N}^2 + (\hat{n}_+ - \hat{n}_-)^2 - 2\hat{N} \right]. \quad (3.8)$$

where  $W = (\varepsilon_+ - \varepsilon_-)$  is the relative environment-introduced energy shift between the right- and left- propagating clouds and  $g$  characterises the atom-atom interaction energy within each cloud.

The initial state vector of the condensate, before the splitting laser pulses are applied is described for a fixed number of atoms  $N$  as

$$|\Psi_{\text{ini}}\rangle = \frac{(b_0^\dagger)^N}{\sqrt{N!}} |0\rangle. \quad (3.9)$$

The splitting or recombination pulses couple the bosonic creation operators  $b_0^\dagger, b_\pm^\dagger$  as described in Sec. 2.1.2

$$\begin{aligned} b_+^\dagger &\rightarrow -\frac{b_+^\dagger}{2} + \frac{e^{i\pi/\sqrt{2}}}{\sqrt{2}} b_0^\dagger + \frac{b_-^\dagger}{2}, \\ b_0^\dagger &\rightarrow \frac{b_+^\dagger}{\sqrt{2}} + \frac{b_-^\dagger}{\sqrt{2}}, \\ b_-^\dagger &\rightarrow \frac{b_+^\dagger}{2} + \frac{e^{i\pi/\sqrt{2}}}{\sqrt{2}} b_0^\dagger - \frac{b_-^\dagger}{2}. \end{aligned} \quad (3.10)$$

The state vector Eq. (3.9), after the splitting pulse was applied, is

$$\begin{aligned} |\Psi_{\text{split}}\rangle &= \frac{(b_+^\dagger + b_-^\dagger)^N}{\sqrt{2^N N!}} |0\rangle, \\ &= \frac{1}{2^{N/2} \sqrt{N!}} \sum_{n=0}^N \binom{N}{n} (b_+^\dagger)^n (b_-^\dagger)^{N-n} |0\rangle. \end{aligned} \quad (3.11)$$

This state evolves under the Hamiltonian (3.8), as described by the Schrodinger equation, until the recombination pulse is applied at the end of interferometric cycle  $t = \tau$ . The state vector at any time  $t$  before interferometric cycle ends is  $|\psi_{\text{evo}}(t)\rangle =$



$e^{-i/\hbar \int_t \hat{H} dt} |\psi_{\text{split}}\rangle$  and has a simple form

$$|\Psi(t)\rangle = \frac{1}{2^{N/2}\sqrt{N!}} \sum_{n=0}^N \binom{N}{n} e^{-i\Phi_n(t)} (b_+^\dagger)^n (b_-^\dagger)^{N-n} |0\rangle, \quad (3.12)$$

$$\Phi_n(t) = \frac{\theta}{2} (2n - N) + \frac{\xi}{2} [2n^2 + 2(n - N)^2 - 2N], \quad (3.13)$$

where  $\binom{N}{n} = \frac{N!}{n!(N-n)!}$  is the binomial coefficient and

$$\theta = \frac{1}{\hbar} \int_t dt W \quad (3.14)$$

is the accumulated phase difference between the left and right clouds due to the environment and

$$\xi = \frac{1}{\hbar} \int_t dt g \quad (3.15)$$

is the accumulated nonlinear phase per atom due to inter-atomic interactions within each cloud.

At the end of the interferometric cycle  $T$ , the recombination pulses act on  $|\Psi(t)\rangle$  in accordance with Eq. (3.9) and transform  $|\psi_{\text{evo}}(t)\rangle$  to  $|\psi_{\text{rec}}\rangle$ , that is

$$\begin{aligned} |\psi_{\text{rec}}\rangle = & \frac{1}{2^{N/2}\sqrt{N!}} \sum_{n=0}^N \binom{N}{n} \exp\left(-i \left[ \frac{\theta}{2} (2n - N) + \xi (n^2 + (n - N)^2) \right]\right) \\ & \left( -\frac{b_+^\dagger}{2} + \frac{e^{i\pi/\sqrt{2}}}{\sqrt{2}} b_0^\dagger + \frac{b_-^\dagger}{2} \right)^n \left( \frac{b_+^\dagger}{2} + \frac{e^{i\pi/\sqrt{2}}}{\sqrt{2}} b_0^\dagger - \frac{b_-^\dagger}{2} \right)^{N-n} |0\rangle, \end{aligned} \quad (3.16)$$

where

$$\begin{aligned} \left( -\frac{b_+^\dagger}{2} + \frac{b_0^\dagger e^{i\pi/\sqrt{2}}}{\sqrt{2}} + \frac{b_-^\dagger}{2} \right)^n \left( \frac{b_+^\dagger}{2} + \frac{b_0^\dagger e^{i\pi/\sqrt{2}}}{\sqrt{2}} - \frac{b_-^\dagger}{2} \right)^{N-n} &= \sum_{j=0}^n \sum_{k=0}^{N-n} \binom{n}{j} \\ & \binom{N-n}{k} (-1)^{n-j} \left( \frac{b_0^\dagger e^{i\pi/\sqrt{2}}}{\sqrt{2}} \right)^{j+k} \left( \frac{b_+^\dagger - b_-^\dagger}{2} \right)^{N-k-j}, \end{aligned} \quad (3.17)$$

and the global phase factor  $\exp(iN\xi)$  is neglected.

## 3.2 Atom-Mach-Zehnder interferometer

In atom Mach-Zehnder interferometer [32] one cloud remains at rest  $\psi_0$  while the other cloud  $\psi_+$  is moving to right after splitting. The annihilation operator  $\hat{\Psi}$  is represented in terms of the basis  $\psi_0$  and  $\psi_+$  as

$$\hat{\Psi} = b_0\psi_0 + b_+\psi_+, \quad (3.18)$$

where  $b_k$  are operators introduced just before Eq. (3.2). Substituting Eq. (3.18) into Eq. (3.1) gives

$$\hat{H}_{\text{eff}} = \frac{W}{2}(\hat{n}_+ - \hat{n}_0) + \frac{g}{2} \left[ \hat{N}^2 + (\hat{n}_+ - \hat{n}_0)^2 - 2\hat{N} \right], \quad (3.19)$$

where  $W$  is the environment-introduced energy shifts between the right-propagating cloud and the stationary cloud,  $g$  is defined in Eqs. (3.7) and

$$\varepsilon_0 = \int d^3\mathbf{r} \psi_0^* \left( -\frac{\hbar^2}{2m} \nabla^2 + V \right) \psi_0. \quad (3.20)$$

During splitting, an optical splitting pulses transforms the operators  $b_k$ ,  $k = 0, -$  as follows

$$\begin{aligned} b_0^\dagger &\rightarrow \frac{1}{\sqrt{2}} (b_0^\dagger - ib_+^\dagger) \\ b_+^\dagger &\rightarrow \frac{1}{\sqrt{2}} (-ib_0^\dagger + b_+^\dagger) \end{aligned} \quad (3.21)$$

Following the same steps described in Sec.3.1, the state vector after recombination is

$$|\Psi_{\text{rec}}\rangle = \frac{1}{\sqrt{2^N N!}} \sum_{n=0}^N \frac{N!}{n!(N-n)!} e^{-i\Phi_n(T)} \left( \frac{b_0^\dagger - ib_+^\dagger}{\sqrt{2}} \right)^n \left( \frac{-ib_0^\dagger + b_+^\dagger}{\sqrt{2}} \right)^{N-n} |0\rangle, \quad (3.22)$$

where  $\Phi_n(T)$  is defined in Eq. (3.13). The product of two terms in brackets in Eq. (3.22) can be expanded as

$$\left( \frac{b_0^\dagger - ib_+^\dagger}{\sqrt{2}} \right)^n \left( \frac{-ib_0^\dagger + b_+^\dagger}{\sqrt{2}} \right)^{N-n} = \sum_{j,k}^{n, N-n} \binom{n}{j} \binom{N-n}{k} (-i)^{n-j+k} (b_0^\dagger)^{j+k} (b_+^\dagger)^{N-j-k} \quad (3.23)$$

### 3.3 Probability

In this section, the probability of finding any number of atoms in the output ports of the Mach-Zehnder and Michelson interferometer is derived. The two probabilities will be shown to be identical. Detailed analysis of the probability of observing any number of atoms in the output port is then provided for Michelson-type interferometer.

#### 3.3.1 Mach-Zehnder interferometer

The state that has  $n_0$  atoms in the cloud at rest and  $n_+ = N - n_0$  atoms in the cloud moving to the right is given by

$$|n_0, n_+\rangle = \frac{(b_0^\dagger)^{n_0}}{\sqrt{n_0!}} \frac{(b_+^\dagger)^{n_+}}{\sqrt{n_+!}} |0\rangle. \quad (3.24)$$

The bra corresponding to the ket given above may be written as

$$\langle n_+, n_0| = \langle 0| \frac{\partial^{n_+}}{\partial (b_+^\dagger)^{n_+}} \frac{\partial^{n_0}}{\partial (b_0^\dagger)^{n_0}}$$

The probability of observing  $n_0$  atoms in the cloud at rest and  $n_+ = N - n_0$  atoms in the cloud moving to the right is given by the modulus squared of the probability amplitude  $\langle n_+, n_0|\Psi_{\text{rec}}\rangle$  i.e  $P(n_0, n_+) = |\langle n_+, n_0|\Psi_{\text{rec}}\rangle|^2$ . Using Eqs. (3.22), (3.23) and (3.24), probability amplitude is

$$\langle n_+, n_0|\Psi_{\text{rec}}\rangle = \sqrt{\frac{N! n_0!}{2^{2N} n_+!}} (N - n_0)! \sum_{n=0}^N e^{-i\theta(n-N/2) - i\xi(n^2 + (n-N)^2)} S(n, n_0), \quad (3.25)$$

where

$$S(n, n_0) = \sum_{j=\max(0, n+n_0-N)}^{\min(n, n_0)} \frac{(-i)^{n+n_0-2j}}{j! (n-j)! (n_0-j)! (N-n-n_0+j)!}. \quad (3.26)$$

At  $\xi = 0$ , it can be shown that

$$\langle n_+, n_0|\Psi_{\text{rec}}\rangle_{\xi=0} = \sqrt{\frac{N!}{n_0! n_+!}} (-i)^N (\sin \theta/2)^{n_0} (\cos \theta/2)^{N-n_0}. \quad (3.27)$$

Comparing Eq. (3.25) at  $\xi = 0$  with Eq. (3.27) shows that

$$\sum_{n=0}^N e^{-in\theta} S(n, n_0) = \frac{(-i)^N 2^N}{n_0! (N - n_0)!} e^{-iN\theta/2} (\sin \theta/2)^{n_0} (\cos \theta/2)^{N-n_0}, \quad (3.28)$$

whose Fourier transform gives

$$S(n, n_0) = \frac{1}{2\pi} \frac{2^N (-i)^N}{n_0! (N - n_0)!} \int_0^{2\pi} e^{i(n-N/2)\theta} (\sin \theta)^{n_0} (\cos \theta)^{N-n_0} d\theta. \quad (3.29)$$

Substituting  $S(n, n_0)$  into Eq. (3.25), the probability amplitude becomes

$$\langle n_+, n_0 | \Psi_{\text{rec}} \rangle = \sqrt{\frac{N!}{n_0! n_+!}} (-i)^N \sum_{n=0}^N e^{-i\theta(n-N/2) - i\xi(n^2 + (n-N)^2)} I(n, n_0) \quad (3.30)$$

where

$$I(n, n_0) = \frac{1}{\pi} \int_0^\pi dx e^{i(2n-N)x} (\sin x)^{n_0} (\cos x)^{N-n_0}. \quad (3.31)$$

The integral  $I(n, n_0)$  is evaluated on a complex plane to yield

$$\begin{aligned} I(n, n_0) &= \frac{e^{in_0\pi/2}}{\sqrt{N\pi}} \exp \left[ n_0 \ln \sqrt{\frac{n_0}{N}} + (N - n_0) \ln \sqrt{1 - \frac{n_0}{N}} - \frac{(n - N/2)^2}{N} \right] \\ &\times \left[ e^{i(2n-N) \arcsin \sqrt{n_0/N} - in_0\pi/2} + e^{-i(2n-N) \arcsin \sqrt{n_0/N} + in_0\pi/2} \right]. \end{aligned} \quad (3.32)$$

Let the summation over  $n$  in Eq. (3.30) is represented as  $\Sigma$ . Using Eq. (3.32), the sum over  $n$  in  $\Sigma(n_0, \theta, \xi)$  may be approximated by an integral and evaluation of the resulting integral gives

$$\begin{aligned} \Sigma(n_0, \theta, \xi) &= \frac{e^{-iN^2\xi/2}}{\sqrt{1 + 2i\xi N}} \exp \left[ n_0 \ln \sqrt{\frac{n_0}{N}} + (N - n_0) \ln \sqrt{1 - \frac{n_0}{N}} \right] \\ &\times \left( e^{-\eta_-^2} + (-1)^{n_0} e^{-\eta_+^2} \right) \end{aligned} \quad (3.33)$$

where

$$\eta_{\mp} = \frac{N}{1 + 2i\xi N} \left( \frac{\theta}{2} \mp \arcsin \sqrt{\frac{n_0}{N}} \right)^2.$$

Then the probability  $P(n_0, n_+) = |\langle n_+, n_0 | \Psi_{\text{rec}} \rangle|^2$ , is

$$P(n_0, n_+) = \frac{N!}{n_+! n_0!} |\Sigma(n_0, \theta, \xi)|^2. \quad (3.34)$$

### 3.3.2 Michelson interferometer

After recombination,  $n_0$  atoms are counted in the cloud that is at rest,  $n_+$  atoms are counted in the cloud moving to the right and  $n_-$  atoms are counted in the cloud moving to the left. The state vector that represent the  $n_0$  atoms being at rest and  $n_{\pm}$  atoms being the clouds moving to right and left respectively is given by

$$|n_+, n_-, n_0\rangle = \frac{(b_+^\dagger)^{n_+}}{\sqrt{n_+!}} \frac{(b_-^\dagger)^{n_-}}{\sqrt{n_-!}} \frac{(b_0^\dagger)^{n_0}}{\sqrt{n_0!}} |0\rangle \quad (3.35)$$

The probability of measuring atoms in the state  $|n_+, n_-, n_0\rangle$  after recombination is given by the modulus square of the probability amplitude  $\langle n_0, n_-, n_+ | \Psi_{\text{rec}} \rangle$ . Using Eqs. (3.35) and (3.16), the probability amplitude is

$$\begin{aligned} \langle n_0, n_-, n_+ | \Psi_{\text{rec}} \rangle &= \frac{1}{\sqrt{2^N N!}} \sum_{n=0}^N \binom{N}{n} e^{-i[\theta(n-N/2)+2\xi(n-N/2)^2]} \\ &\quad \times \langle 0 | \frac{(b_0)^{n_0}}{\sqrt{n_0!}} \frac{(b_-)^{n_-}}{\sqrt{n_-!}} \frac{(b_+)^{n_+}}{\sqrt{n_+!}} \sum_{j=0}^n \sum_{k=0}^{N-n} \binom{n}{j} \\ &\quad \times \binom{N-n}{k} (-1)^{n-j} \left( \frac{b_0^\dagger e^{i\pi/\sqrt{2}}}{\sqrt{2}} \right)^{j+k} \left( \frac{b_+^\dagger - b_-^\dagger}{2} \right)^{N-k-j}, \end{aligned} \quad (3.36)$$

where the irrelevant phase term  $\exp(-i\xi N^2/2)$  have been omitted, and the probability  $P$  is given by

$$P = |\langle n_0, n_-, n_+ | \Psi_{\text{rec}} \rangle|^2. \quad (3.37)$$

#### Probability for $\xi$ equal to zero

For  $\xi = 0$ , the probability amplitude Eq. (3.36) takes the form

$$\langle n_0, n_-, n_+ | \Psi_{\text{rec}} \rangle = \sqrt{\frac{N!}{2^N n_+! n_-! n_0!}} (-1)^{n_-} (-i \sin(\theta/2))^{N-n_0} \left( \sqrt{2} \cos(\theta/2) \right)^{n_0}, \quad (3.38)$$

and the probability  $P$  is given by

$$P = |\langle n_0, n_-, n_+ | \Psi_{\text{rec}} \rangle|^2 = \frac{1}{2^N} \frac{N!}{n_+! n_-! n_0!} \left( \sin^2 \frac{\theta}{2} \right)^{n_+ + n_-} \left( 2 \cos^2 \frac{\theta}{2} \right)^{n_0}. \quad (3.39)$$

Eq. (3.39) is a binomial distribution and could be written as a product of two probability functions

$$P = P_{\pm}P(n_0), \quad (3.40)$$

where

$$P_{\pm} = \frac{(N - n_0)!}{2^{N-n_0} n_+! n_-!}, \quad (3.41)$$

and

$$P(n_0) = \frac{N!}{n_0!(N - n_0)!} \left( \sin^2 \frac{\theta}{2} \right)^{N-n_0} \left( \cos^2 \frac{\theta}{2} \right)^{n_0}. \quad (3.42)$$

The probability function  $P_{\pm}$  describes the probability of observing  $n_+$  and  $n_-$  atoms in the right and left moving clouds respectively for a fixed number of atoms in the cloud at rest. This function is independent of phase angle  $\theta$  and is normalised to unity. The probability function  $P(n_0)$  is the probability of observing  $n_0$  atoms in cloud at rest. It is normalised to unity and depends on the phase angle  $\theta$  introduced by the environment.

For very large population of atoms ( $N \gg 1$ ), the factorials may be approximated using Stirling's formula,

$$n! = \sqrt{2\pi n} n^n e^{-n}, \quad (3.43)$$

and the probability densities that correspond to  $P(n_0)$  and  $P_{\pm}$  become

$$P(n_0) = \frac{2}{\sqrt{2\pi N} \sin \theta} \exp \left[ -\frac{2}{N} \frac{(n_0 - N \cos^2(\theta/2))^2}{\sin^2 \theta} \right], \quad (3.44)$$

and

$$P_{\pm} = \sqrt{\frac{2}{\pi(n_+ + n_-)}} \exp \left[ -\frac{2}{n_+ + n_-} \left( \frac{n_+ - n_-}{2} \right)^2 \right], \quad (3.45)$$

respectively, where  $n_+ + n_- \gg 1$ .

Both the probability functions  $P_{\pm}$  and  $P(n_0)$  are Gaussian. For a fixed value of  $n_0$  atoms in the stationary cloud, the peak of the probability function  $P_{\pm}$  is located

at  $(N - n_0)/2$ , with an average values of  $n_+$  and  $n_-$  given by

$$\langle n_+ \rangle = \langle n_- \rangle = \frac{1}{2}(N - n_0), \quad (3.46)$$

and standard deviations

$$\Delta n_+ = \Delta n_- = \frac{1}{2}\sqrt{N - n_0}. \quad (3.47)$$

The number of atoms in the right and the left clouds are anticorrelated,

$$\text{Cov}(n_+, n_-) = \langle n_+ n_- \rangle - \langle n_+ \rangle \langle n_- \rangle = -\frac{1}{4}(N - n_0) \quad (3.48)$$

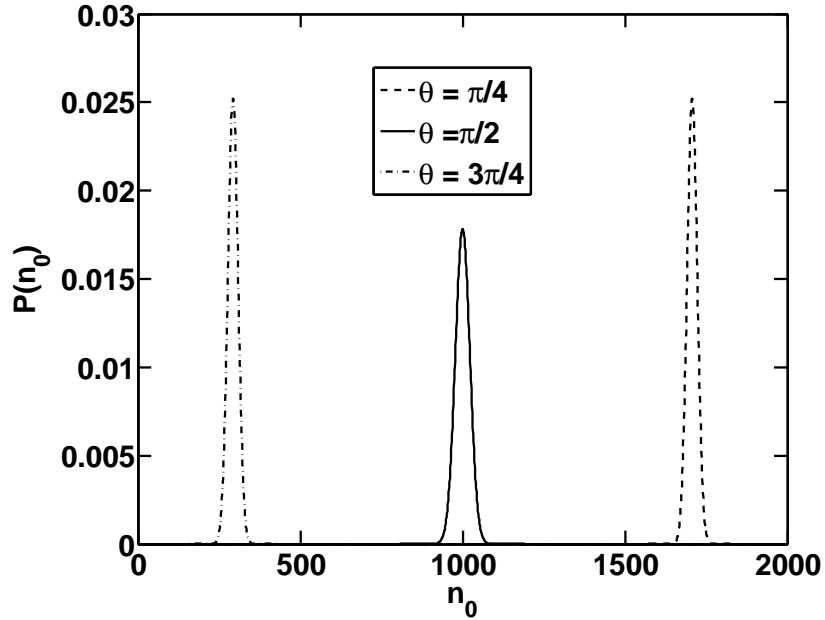


**Figure 3.1** The probability function  $P(n_0)$  vs  $n_0$  at three different values of  $\theta$ .

The maximum of the probability function  $P(n_0)$  is located at  $n_0 = N \cos^2(\theta/2)$ . Since  $n_0$  take values in the interval  $\{0, N\}$ , then  $\theta$  take values in the interval  $0 < \theta < \pi$ . The end points  $\theta = 0$  and  $\theta = \pi$  are excluded because the probability function  $P(n_0)$

Eq. (3.44) is not defined at the end points. To get the values of  $P(n_0)$  at the end points, one has to use Eq. (3.42) which gives that  $P(n_0) = 1$  for  $\theta = 0, \pi$ . The probability function  $P(n_0 = N) = 1$  for  $\theta = 0$  means that all the atoms are in the cloud at rest after recombination and  $P(n_0 = 0) = 1$  for  $\theta = \pi$  implies that no atom is observed in the cloud at rest after recombination; all the atoms are found in the clouds moving to the left and right after recombination. The probability of finding any population of atoms in the cloud at rest for any other value of  $\theta$  in the interval  $0 < \theta/2 < \pi/2$  is well described by Eq. (3.44).

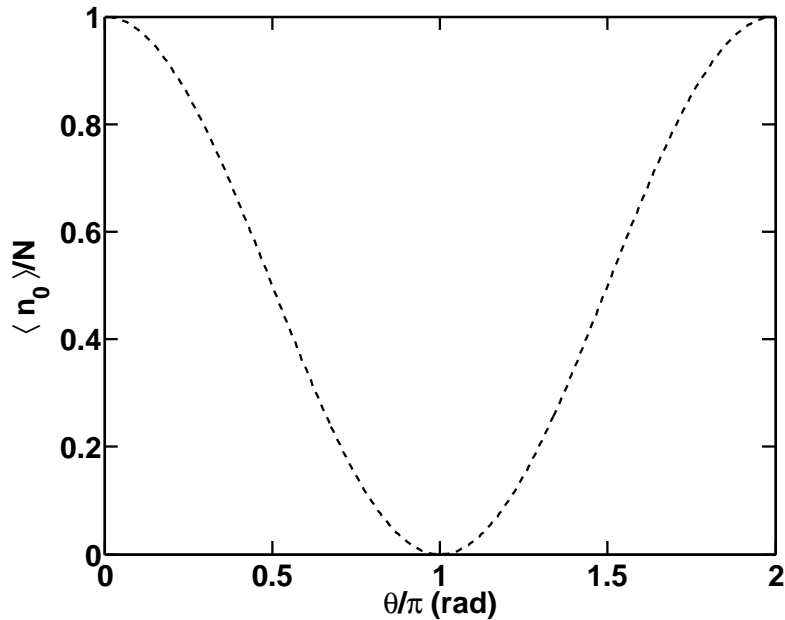


**Figure 3.2** The relative mean value  $\langle n_0 \rangle / N$  vs  $\theta$ .

Shown in Fig 3.1 is the plot of the probability function Eq. (3.49) at three different values of  $\theta$ . The width of each peak on the graph scales roughly as  $\sqrt{(N \sin^2 \theta)/4}$  so that the relative width of the distribution scales roughly as  $\sqrt{\sin^2 \theta / (4N)}$ . Because of the dependence of the width of the distribution function on  $\theta$ , the width of the probability function is largest at  $\theta = \pi/2$  and vanishes at  $\theta = 0, \pi$ . The changing val-



ues of  $\theta$  move the peak of the probability function  $P(n_0)$  from  $n_0 = N$  corresponding to the situation where more atoms are in the stationary cloud towards  $n_0 = 0$  that corresponds to situation where less number of atoms are in stationary cloud.

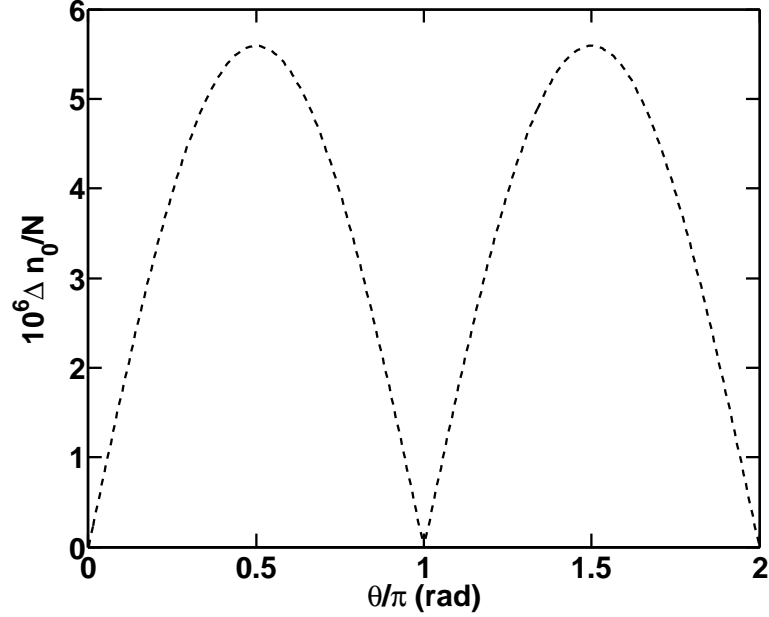


**Figure 3.3** The relative standard deviation  $\Delta n_0/N$  vs  $\theta$ .

The mean value and variance of the probability function  $P(n_0)$  are

$$\langle n_0 \rangle = N \cos^2 \frac{\theta}{2} \quad (3.49)$$

and

$$(\Delta n_0)^2 = N \cos^2 \frac{\theta}{2} \sin^2 \frac{\theta}{2} \quad (3.50)$$

Figures 3.2 and 3.3 show the plots of the relative mean value and relative standard deviation respectively. In Fig. 3.2 the contrast is unity and the visibility is maximum (unity). So for non-interacting condensate, full fringes would be observed in every run of the experiment. The error associated in counting the number of atoms in the

stationary cloud shows a sinusoidal oscillations with a periodicity of  $\pi$  as shown in Fig. 3.3. At  $\theta = 0, m\pi$  (where  $m$  is any integer value), the standard deviation is zero and corresponds to situations where all the atoms are known with absolute certainty to be either in the cloud at rest or in moving clouds. At this point, the width of the probability function vanishes as previously described (see Fig 3.1). Even values of  $m$  and zero corresponds to situation when all the atoms are in the cloud at rest while odd values of  $m$  corresponds to the case when all the atoms are in the moving clouds. The standard deviation is maximum at  $\theta = m_{odd}\pi/2$  as shown in Fig. 3.3 [see also Fig. 3.1] with  $m_{odd} = 1$  and occurs when equal population of atoms are found in the moving clouds and the cloud at rest.

### Probability for $\xi$ not equal to zero

The bra corresponding to the ket given in Eq. (3.35) is written as

$$\langle n_0, n_-, n_+ | = \langle 0 | \frac{\partial^{n_0}}{\partial (b_0^\dagger)^{n_0}} \frac{\partial^{n_-}}{\partial (b_-^\dagger)^{n_-}} \frac{\partial^{n_+}}{\partial (b_+^\dagger)^{n_+}}. \quad (3.51)$$

The derivatives with respect to  $b_0^\dagger$  selects only terms with  $j + k = n_0$  from the sum in Eq. (3.36) giving

$$\langle n_0, n_-, n_+ | \psi_{rec} \rangle = \sqrt{\frac{N!n_0!}{2^{(3N-n_0)}n_+!n_-!}} (N - n_0)! e^{in_0\pi/\sqrt{2}} (-1)^{n_-} \sum_{n=0}^N e^{-i\theta(n-N/2)+i\phi(n^2+(n-N)^2)} S(n, n_0), \quad (3.52)$$

where

$$S(n, n_0) = \sum_{j=\max(0, n_0+n-N)}^{\min(n, n_0)} \frac{(-1)^{n-j}}{j!(n-j)!(n_0-j)!(N-n-n_0+j)!}. \quad (3.53)$$

Comparing the probability amplitude Eq. (3.52) for  $\xi = 0$  and Eq. (3.38) shows that

$$\sum_{n=0}^N e^{-in\theta} S(n, n_0) = \frac{2^N}{(N-n_0)!n_0!} \left(\cos \frac{\theta}{2}\right)^{n_0} \left(-i \sin \frac{\theta}{2}\right)^{N-n_0} e^{-iN\theta/2}, \quad (3.54)$$

where the Fourier transform of Eq. (3.54) gives

$$S(n, n_0) = \frac{1}{2\pi} \frac{2^N}{(N - n_0)! n_0!} \int_0^{2\pi} d\theta e^{i(n - N/2)\theta} \left( \cos \frac{\theta}{2} \right)^{n_0} \left( -i \sin \frac{\theta}{2} \right)^{N - n_0}. \quad (3.55)$$

Using Eq. (3.52), one writes the probability density Eq. (3.37) as product of two functions

$$P(n_0, n_-, n_+) = P_{\pm} P_0(n_0, \theta, \xi), \quad (3.56)$$

where  $P_{\pm}$  is already defined in Eq. (3.41) and

$$P_0(n_0, \theta, \xi) = \frac{N!}{n_0!(N - n_0)!} |\Sigma(n_0, \theta, \xi)|^2. \quad (3.57)$$

The function  $\Sigma(n_0, \theta, \xi)$  is

$$\begin{aligned} \Sigma &= \frac{e^{-iN^2\xi/2}}{\sqrt{1 - 2iN\xi}} \exp \left[ (N - n_0) \ln \sqrt{1 - \frac{n_0}{N}} + n_0 \ln \sqrt{\frac{n_0}{N}} \right] \\ &\times \left( e^{-\eta_-^2} + (-1)^{N - n_0} e^{-\eta_+^2} \right), \end{aligned} \quad (3.58)$$

and

$$\eta_{\pm} = \frac{N \left( \arccos \sqrt{n_0/N} \pm \theta/2 \right)^2}{1 - 2iN\xi}. \quad (3.59)$$

Comparing Eq. (3.57) and Eq. (3.34), it is seen that the function  $\Sigma(n_0, \theta, \xi)$  in both equations are equivalent. It then means that probabilities  $P_0(n_0, \theta, \xi)$  [Eqs. (3.34) and (3.57)] are identical so that the results to be obtained in subsequent discussion for Michelson-type interferometer are also applicable to the Mach-Zehnder-type interferometer.

### 3.4 Characteristic features of the probability density

The function  $P_0(n_0, \theta, \xi)$  is proportional to the modulus squared of the sums of two terms

$$P_0(n_0, \theta, \xi) = \sqrt{\frac{N}{2\pi n_0 (N - n_0) (1 + 4N^2 \xi^2)}} \left| e^{-\eta_-^2} + (-1)^{N-n_0} e^{-\eta_+^2} \right|^2. \quad (3.60)$$

The relative phase difference between the two terms in  $P_0(n_0, \theta, \xi)$  as a function of  $n_0$  changes rapidly due to the multiplier  $(-1)^{N-n_0}$ . Thus, the interference terms are neglected in calculating both mean and standard deviation. The mean population  $\langle n_0 \rangle$  of atoms in the cloud at rest after recombination is

$$\langle n_0 \rangle = \int_0^N dn_0 n_0 P(n_0, \theta, \xi). \quad (3.61)$$

The evaluation of the above integral gives

$$\langle n_0 \rangle = \frac{N}{2} \left[ 1 + \exp\left(-\frac{1 + 4N^2 \xi^2}{2N}\right) \cos \theta \right]. \quad (3.62)$$

Similarly, the variance is

$$(\Delta n_0)^2 = \frac{N^2}{2} \left[ \frac{1}{4} + \frac{\exp\left(-2\frac{1+4N^2\xi^2}{N}\right) \cos 2\theta}{4} - \frac{\exp\left(-\frac{1+4N^2\xi^2}{N}\right) \cos^2 \theta}{2} \right]. \quad (3.63)$$

These results are understood by studying the dependence of the function  $P_0(n_0, \theta, \xi)$  on the number of atoms  $n_0$  for different values of the strength of the interatomic interactions  $\xi$ . At relatively small values of  $\xi$  such that  $\xi \ll 1/\sqrt{N}$ , the term  $\exp(-\eta_-)$  in Eq. (3.60) for the probability dominates the other. The probability  $P_0(n_0, \theta, \xi)$  is then Gaussian

$$P_0(n_0, \theta, \xi) \approx \sqrt{\frac{N}{2\pi n_0 (N - n_0) (1 + 4N^2 \xi^2)}} \exp \left[ -\frac{2N \left( \theta/2 - \arccos \sqrt{n_0/N} \right)^2}{1 + 4\xi^2 N^2} \right] \quad (3.64)$$

with a maximum located at  $n_0 = N \cos^2 \theta/2$ . This situation is shown in Fig. 3.4. The two curves in the figure are plots of the probability density  $P_0(n_0, \theta, \xi)$  given by Eq. (3.64) versus  $n_0$  for two different values of interatomic interactions strength  $\xi$ . Both curves correspond to the same value of angle  $\theta$ . The noticeable feature of Fig. 3.4 is the increase in the width of the probability distribution with  $\xi$ . This behaviour is explained by Eq. (3.63), which in the limit  $\xi \ll 1/\sqrt{N}$  reduces to

$$\Delta n_0 \approx \frac{\sqrt{N}}{2} \sqrt{1 + 4N^2 \xi^2} \sin \theta \quad (3.65)$$

For very small values of  $\xi$  ( $\xi \ll 1/N$ ), the influence of the interatomic interactions on the operation of the beamsplitter is negligible. The relative standard deviation of the number of atoms in the central cloud is inversely proportional to the square root of the total number of atoms in the system:  $\Delta n_0 \propto 1/\sqrt{N}$ . For  $1/N \ll \xi \ll 1/\sqrt{N}$ , the width of the distribution grows linearly with increase in  $\xi$ .

The mean value of  $n_0$  for  $\xi \ll 1/\sqrt{N}$  reasonably corresponds to the position of the peak. Equation (3.62) for  $\langle n_0 \rangle$  in this limit yields

$$\langle n_0 \rangle \approx \frac{N}{2} (1 + \cos \theta). \quad (3.66)$$

As is seen,  $n_0$  depends on  $\theta$  but not on  $\xi$ .

For large values of  $\xi$  ( $\xi \approx 1/\sqrt{N}$ ), the width of the probability density  $P_0(n_0, \theta, \xi)$  becomes of the order of the total number  $N$  of atoms in the system. The two terms  $\exp(-\eta_-)$  and  $\exp(-\eta_+)$  in Eq. (3.60) are now comparable in magnitude. The transition to this limit is shown by Fig. 3.5 and Fig. 3.6. Black regions not resolved in Fig. 3.5 and Fig. 3.6 correspond to rapid spatial oscillations with period 2. These oscillations are clearly seen in Fig. 3.7, which shows part of Fig. 3.6 for a narrow range of values of  $n_0$ . The oscillations are caused by the interference between the two terms in Eq. (3.60). As the magnitude of  $\xi$  approaches  $1/\sqrt{N}$ , these terms become comparable in magnitude. Because of the nearly  $\pi$ -phase change between the two

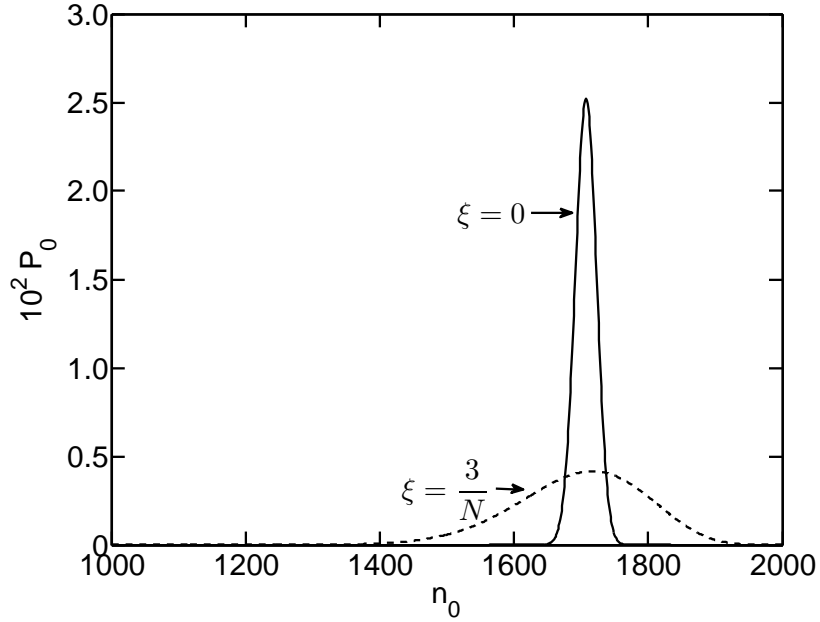


**Figure 3.4** The probability function  $P_0(n_0, \theta, \xi)$  vs  $n_0$  for  $\xi = 0$  and  $\xi = 3/N$ . For both curves,  $\theta = \pi/4$  and  $N = 2000$ .

terms very time  $n_0$  changes by one due to the factor  $(-1)^{N-n_0}$ , the two terms consecutively add either in phase or out of phase when one steps through different values of  $n_0$ . Along with rapid spatial oscillations, both Fig. 3.5 and Fig. 3.6 demonstrate oscillations of the envelopes at a much slower spatial rate which are more pronounced for larger values of the interactions strength. These oscillations are due to the fact that the relative phase of the terms  $\exp(-\eta_-)$  and  $\exp(-\eta_+)$  in Eq. (3.60) changes with  $n_0$ . The nodes in Fig. 3.6 correspond to the value of this relative phase being equal to 0 or a  $\pi$  and an antinodes have the phase shifted by  $\pm\pi/2$ .

Figs. 3.5 and 3.6 indicate that the probability  $P_0(n_0, \theta, \xi)$  and, as a consequence,  $\langle n_0 \rangle$  and  $\Delta n_0$ , become less sensitive to changes in the environment-introduced angle  $\theta$ . This fact is graphically illustrated in Figs. 3.8 and 3.9 showing the average value of the number of atoms in the central cloud  $\langle n_0 \rangle$  and the standard deviation  $\Delta n_0$  versus

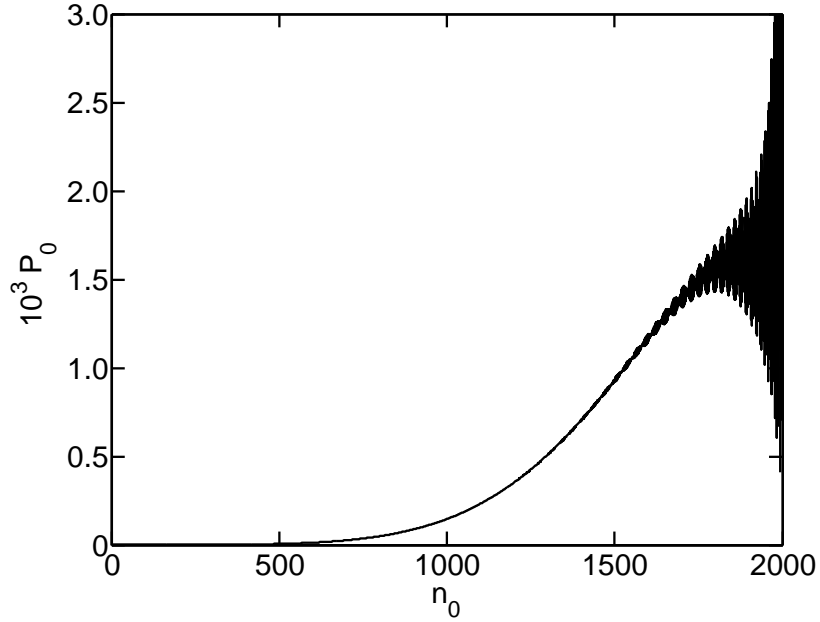


**Figure 3.5** The probability function  $P_0(n_0, \theta, \xi)$  vs  $n_0$  for  $\xi = 0.2/\sqrt{N}$ ,  $\theta = \pi/4$  and  $N = 2000$ .

$\theta$  as given by Eqs. (3.62) and (3.63), respectively. Fig. 3.8 demonstrates that increased interatomic interactions eventually lead to the loss of contrast of interference fringes. Additionally, larger interatomic interactions cause large shot-to-shot fluctuations in the number of atoms in each of the three output ports, as is seen from Fig. 3.9. The loss of contrast of the interference fringes can be quantified by writing Eq. (3.62) as

$$\langle n_0 \rangle = \frac{N}{2} (1 + V \cos \theta), \quad (3.67)$$

where

$$V = \exp\left(-\frac{1 + 4N^2\xi^2}{N}\right), \quad (3.68)$$

where  $V$  is the fringe contrast. Figure 3.10 shows the fringe contrast Eq. (3.68) as a function of  $\xi$  and demonstrates that the values of  $\xi$  approaching  $1/\sqrt{N}$  result in the washing out of interference fringes.

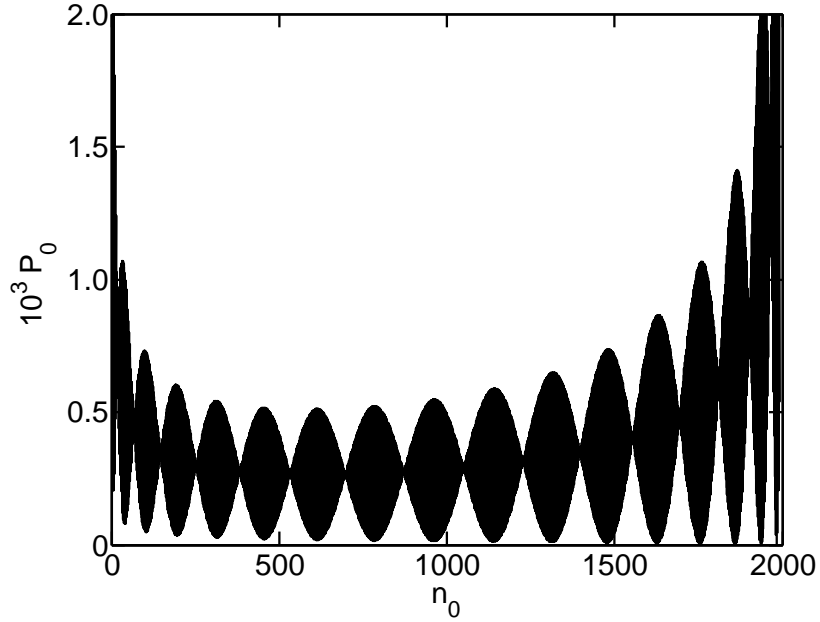


**Figure 3.6** The probability function  $P_0(n_0, \theta, \xi)$  vs  $n_0$  for  $\xi = 1/\sqrt{N}$ ,  $\theta = \pi/4$  and  $N = 2000$ .

### 3.5 Comparison with experiments

As shown in previous section, limited interference fringes were observed when the nonlinear phase per atom  $\xi$  due to interatomic interactions is about the order of  $1/\sqrt{N}$ . Experiments [31, 53, 60] have reported that loss of fringe contrast were due to confinement effects [59, 60] and repulsion between the atomic densities [32, 59, 60] during the splitting and recombination of clouds. In order to quantify the effects due to interatomic interactions within the condensate, the phase  $\xi$  is calculated in terms of experimental parameters. The experiments [31, 53, 60] to be discussed in the following were conducted in parabolic traps with confining potential of the form

$$V = \frac{M}{2} (\omega_x^2 x^2 + \omega_y^2 y^2 + \omega_z^2 z^2). \quad (3.69)$$



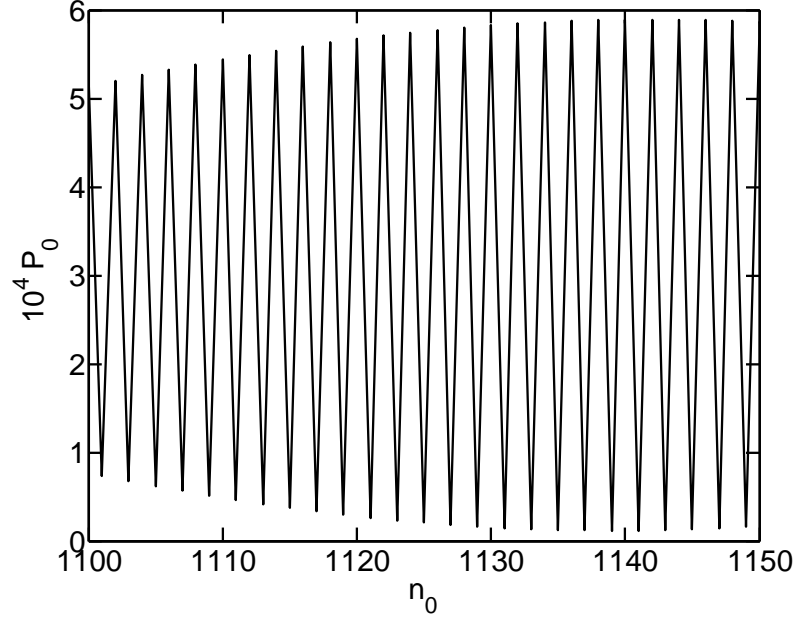


**Figure 3.7** An enlargement of part of Fig. 3.6 showing fast-scale spatial oscillations of the probability function

The density profiles of the moving clouds are well described by Thomas-Fermi approximation

$$|\psi_{\pm}| = \frac{\mu_n}{U_0 n} \left( 1 - \frac{x^2}{R_x^2} - \frac{y^2}{R_y^2} - \frac{z^2}{R_z^2} \right), \quad |\psi_{\pm}|^2 \geq 0, \quad (3.70)$$

where  $R_i$  are the radial sizes of the cloud in the  $i$ th dimension,  $\mu_n$  is the chemical potential of the BEC cloud with  $n$  atoms and  $U_0 = 4\pi\hbar^2 a_{sc}/M$  is the strength of two-body interaction within the cloud.

After splitting each of the moving clouds contains on the average  $N/2$  atoms. The repulsive nonlinearity is no longer balanced by the confining potential and the radii of both clouds starts to oscillate. The maximum size of the oscillating clouds is equilibrium size corresponding to  $N$  atoms and the minimum size lies below the corresponding equilibrium size corresponding to  $N/2$  atoms. For estimates, the number  $n$  of atoms in each cloud is taken to be  $N/2$  atoms, that is  $n = N/2$ . Evaluating

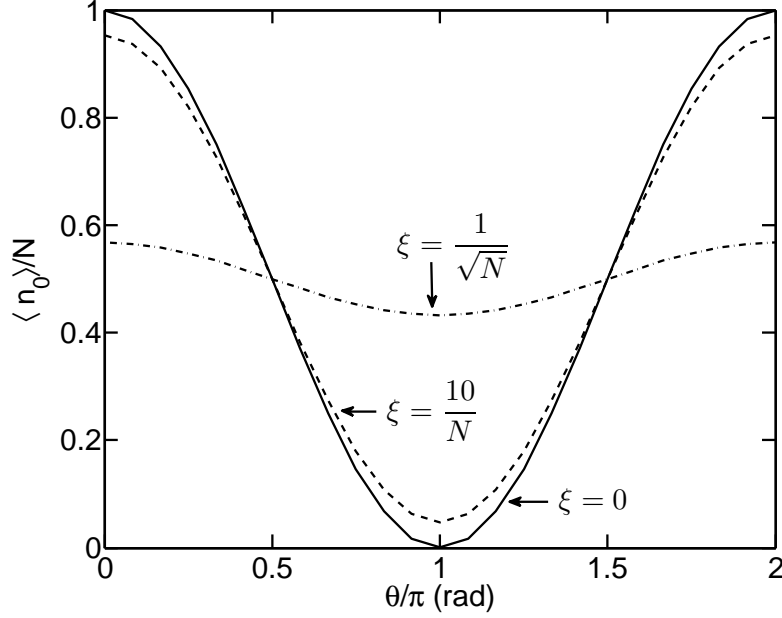


**Figure 3.8** The normalised mean value of the number of atoms in the central cloud  $\langle n_0 \rangle / N$  vs  $\theta$  for  $N = 2000$ .

Eq. (3.15) give the accumulated relative phase  $\xi$  due to interatomic interactions as

$$\xi = \frac{2 \mu_n T}{7 n \hbar} \quad (3.71)$$

where  $\mu_n = 2^{-2/5} \mu$ ,  $\mu$  the equilibrium chemical potential [71, 75] is

$$\mu = \frac{\hbar \bar{\omega}}{2} \left( 15 N \frac{a_{\text{sc}}}{\bar{a}} \right)^{2/5}, \quad (3.72)$$

$$\bar{\omega} = (\omega_x \omega_y \omega_z)^{1/3}, \quad \bar{a} = \sqrt{\hbar / M \bar{\omega}}.$$

The relative importance of interatomic interaction effects on the operation of the interferometer is determined by the parameter  $P = \xi \sqrt{N} \ll 1$ ,

$$P = \left( \frac{1800}{7^5} \right)^{1/5} \left( \frac{a_{\text{sc}}}{\bar{a}} \right)^{2/5} \bar{\omega} T N^{-1/10} \quad (3.73)$$

shows that the contrast of the interference fringes decreases with the increase in  $P$ . The condition of good contrast can be somewhat arbitrarily stated as  $P < 1/2$  (for  $P = 0.5$ , the contrast  $V = 0.6$ ).

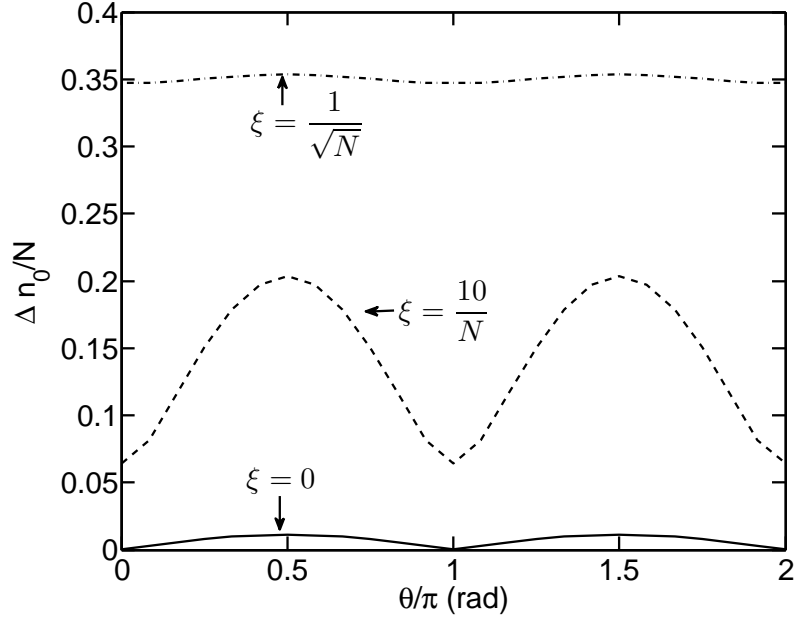


**Figure 3.9** Normalised standard deviation  $\Delta n_0/N$  vs  $\theta$  for  $N = 2000$ .

Equation (3.73) shows that  $P \propto T\bar{\omega}^{-6/5}N^{-1/10}$ . The dependence of  $P$  on the total number of atoms in BEC clouds is very weak, and so this parameter is primarily dependent on the duration of the interferometric cycle and averaged frequency of the trap.

Experiments by Wang et al. [31] were conducted using the Michelson geometry. The BEC consisted of about  $10^5$  Rb atoms [83]. The transverse and longitudinal frequencies of the trap were 177 Hz and 5 Hz respectively. The propagation time  $T$  was up to 10 ms. For these parameters and the value of the scattering length  $a_{sc} = 5.2 \times 10^{-9}$  m [84], Eq. (3.73) yields  $P \approx 1.6 \times 10^{-2}$ . Thus, the interatomic interactions were not limiting the visibility of the interference fringes in these experiments.

Similar experiments were performed by Garcia [53] and Burke [59] also in the geometry of a Michelson interferometer. In Ref. [53], a BEC cloud of about  $10^4$   $^{87}\text{Rb}$  atoms has been produced in a trap with frequencies of 6.0 Hz, 1.2 Hz and 3.0 Hz,

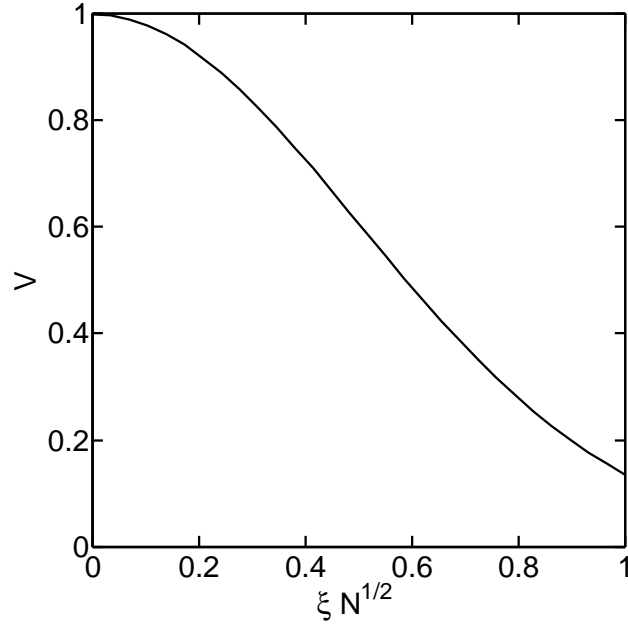


**Figure 3.10** Interference fringe contrast  $V$  as a function of the interatomic interactions  $\xi\sqrt{N}$ .

respectively. The interferometric time  $T$  was about 40 ms. Using Eq. (3.73), the value of the parameter  $P$  in the experiment evaluates to  $P \approx 10^{-2}$ , which was too small to result in observed degradation of the contrast. The loss of visibility in the experiment [53] was attributed by the authors to spatial noise on the splitting beams and asymmetric splitting of the cloud due to the condensates' residual motion when it was loaded into the trap. At longer times, the loss of coherence might have been caused by various noise sources. Similar results were reported in Ref. [59], where the confinement frequencies were deliberately kept weak, making the atomic density and thus interatomic interaction effects small.

Horikoshi et al. [32, 60] demonstrated a BEC Mach-Zehnder interferometer. The number of atoms in Ref. [60] was about  $3 \times 10^3$  and the radial frequency of the trap was fixed at 60 Hz. The experiments have been conducted for two different values

of the axial frequencies and interrogation times  $T$ . At an axial frequency of  $\omega_z = 2\pi \times 17$  Hz and the propagation time of the cloud about  $T = 60$  ms, the parameter  $P = \xi\sqrt{N}$  estimated using Eq. (3.73) turns out to be about 0.38. For this value of  $P$ , Eq. (3.43) gives the value of the fringe contrast about 70%. The experimental value is 30% [60]. Similarly, for the axial frequency 10.29 Hz and interferometric time 97 ms Eq. (3.73) gives the value of  $P \approx 0.5$  corresponding to an estimated contrast of 58%. In this case no fringes were observed experimentally with about 40% scatter of data points. The authors of Ref. [60] conjecture that the vibrations could be the main source of the loss of fringes in their experiments. The above estimates indicate that the interatomic interactions could be also partly responsible for the observed degradation of the interference fringe.

# Chapter 4

## Spatial phase and phase diffusion of Bose-Einstein condensate

Besides the phase diffusion discussed in previous chapter, unwanted spatial relative phase is another dephasing mechanism that washes out the interference fringe contrast. Spatial relative phase is accumulated via different mechanism by atomic clouds. For example, in a single-reflection interferometer [31], during propagation the outer edge of each cloud experiences a higher potential than the inner edge (the outer edge in the first half of the cycle when the clouds move away from each other and the trailing edge in the second part when the clouds move towards each other). The outer edge thus accumulates a larger phase than the inner one. During the recombination, the outer edge of one cloud interferes with the inner edge of another and the phase difference accumulated due to the presence of the confining potential leads to a coordinate-dependent residual phase across the cloud after recombination. Another mechanism for spatial phase accumulation is due to the repulsion of the two atomic densities when they spatially overlap. During separation, the inner edge of one cloud interacts with atoms in the other cloud until it has traversed the entire

---

length of the other cloud, while the outer edge of each cloud hardly interacts with any atoms in the other cloud and similarly during recombination. As a result, the inner edge accumulates a larger phase than the outer edge. Still another mechanism for accumulation of spatial phase is due to the fact that the velocities of the moving clouds during reflection are different from their initial velocities due to the influence of confining potential and the atom-atom interactions. As a result the reflection pulses are not exactly on resonance and do not exactly reverse clouds' velocities; the direction of propagation of each of the clouds does change but the speeds before and after reflection are different.

Both single- and double-reflection interferometer geometries have been studied in Refs. [59, 62–64]. According to the studies of Refs. [59, 64], symmetric motion of the two clouds in a double-reflection geometry partially cancels the velocity errors imposed by the reflection pulses and the phase imposed by the confining potential. This conclusion has been confirmed experimentally in Ref [59]. The free oscillation interferometer provides an even greater degree of cancellation of unwanted spatial relative phase since it does not rely on the reflection pulses and do not suffer from velocity mismatch effects. Experiments [59, 60] where the atomic clouds were allowed to be reflected from their classical turning points instead of using reflection pulses to truncate their motion, confirmed a more accurate cancellation of unwanted spatial relative phase.

In literature, both spatial phase and phase diffusion have been addressed separately in the operation of guided-wave atom interferometers. The studies of Ref. [59, 60, 62–64, 85] focused on analysing the effects of spatial relative phase on the interference fringe contrast and in Ref. [82], phase diffusion was analysed and discussed while neglecting spatial phase. In this chapter, for the first time the combined effects of spatial phase and phase diffusion on interference fringe contrast are analysed qual-

itatively using the probability of observing any number of atoms in the output ports of a Michelson interferometer. It will be shown that the effects arising from spatial phase on the interference fringe contrast dominates that due to phase diffusion. The remainder of the chapter is organised as follows. The state vector of the system is derived in Sec. 4.1 using the appropriate recombination matrix elements in the presence of spatial relative phase. This is followed by the derivation of the probability of counting any number of atoms in the output ports of the interferometer and the calculation of the population's averages in the different limiting cases of the unwanted phases in Sec. 4.2. The interference fringe contrast is optimised in the various limits in Sec. 4.3 and then discussed in Sec. 4.4.

## 4.1 State vector at recombination

The dynamics of the mode-entangled states of a split cloud is described by the two coupled [63, 64] time dependent Gross-Pitaevskii equations

$$\begin{aligned} i\hbar \frac{\partial \psi_+}{\partial t} &= \frac{P^2}{2M} \psi_+ + V \psi_+ + g_{1D} (|\psi_+|^2 + 2|\psi_-|^2) \psi_+, \\ i\hbar \frac{\partial \psi_-}{\partial t} &= \frac{P^2}{2M} \psi_- + V \psi_- + g_{1D} (|\psi_-|^2 + 2|\psi_+|^2) \psi_-, \end{aligned} \quad (4.1)$$

where  $g_{1D} = \frac{2\hbar^2 a_s}{M a_\perp^2}$  is the strength of the two-body interaction,  $M$  is the mass of the atom,  $a_\perp$  is the transverse oscillator length and  $a_s$  is the s-wave scattering length. The normalised solutions  $\psi_\pm$  of the two coupled Gross-Pitaevskii equation is expressed in the hydrodynamic approximation as  $\psi_\pm = \sqrt{n_\pm(x, t)} e^{-i\phi_\pm(x, t)/2}$ , where

$$n_\pm(x, t) = \frac{3}{4L} \left[ 1 - \left( \frac{x \mp x_0}{L} \right)^2 \right] \quad (4.2)$$

is the density of the atomic clouds moving to the right (denoted by plus sign) or left (denoted by minus sign) respectively while  $\phi_\pm$  is the corresponding absolute spatial



phase [63, 64] accumulated by moving clouds,

$$\phi_{\pm}(x, t) = \pm \frac{Mv}{2\hbar}(x \mp x_0) + \frac{d}{2L_0^2}(x \mp x_0)^2 \pm \frac{s}{3!L_0^3}(x \mp x_0)^3. \quad (4.3)$$

Parameter  $d$  is the strength of the quadratic phase in the clouds that moved to the right and left respectively,  $s$  is the strength of the cubic phase in the clouds that moved to the right and left respectively,  $x_0$  is the position of the center of mass of the moving clouds,  $v$  is the velocity of the cloud just before recombination.  $L_0$  is the initial equilibrium radius of the cloud in Thomas-Fermi approximation given by

$$L_0 = \left( \frac{3\hbar\omega_{\perp}a_s N}{M\omega^2} \right)^{1/3}, \quad (4.4)$$

where  $N$  is the total number of atoms in the condensate,  $\omega_{\perp}$  is the transverse frequency of the parabolic trap, and  $\omega$  is the longitudinal frequency of the trap.

Usually the quantity of interest in interferometry is not the absolute phases  $\phi_{\pm}$  but the relative phase  $\phi = \phi_+ - \phi_-$ . The wave function of the system before recombination in terms of the relative phase is

$$\psi = \frac{1}{\sqrt{2}} [\sqrt{n_+} e^{-i\phi/2} + \sqrt{n_-} e^{i\phi/2}], \quad (4.5)$$

where the irrelevant global phase term  $e^{-i(\phi_+ + \phi_-)/2}$  has been ignored since it does not affect the physics of the problem. The relative phase  $\phi$  is written in terms of dimensionless variable  $z$  and parameter  $q$  as [85]

$$\phi(z, q) = \Delta K(q)z + \Gamma(q)z^3, \quad (4.6)$$

where

$$K(q) = \frac{R}{\epsilon} \left[ \Delta V - \frac{Gq}{R} + \frac{Sq^2}{2R} \right], \quad (4.7)$$

$$\Gamma(q) = \frac{S}{6\epsilon},$$

and

$$\begin{aligned} z &= \frac{X}{R}, & q &= \frac{X_0}{R}, & R &= \frac{L}{L_0}, \\ 2\epsilon g &= G, & 2\epsilon s &= S, & X &= \frac{x}{L_0}. \end{aligned} \quad (4.8)$$

$\Delta V$  is the dimensionless change in the speed of the clouds at recombination,  $q$  the position of the center of mass in the dimensionless variable and  $R$  is their dimensionless radius.

At recombination, the wave functions  $\psi_{\pm} = \sqrt{n_{\pm}} e^{\mp i\phi/2}$  are transformed as follows

$$\begin{aligned} \psi_+ &\rightarrow -\frac{Qe^{-i\varphi}\chi_+ + De^{-i\pi/2}\eta_+}{2} + \frac{Qe^{-i\varphi}\chi_0 + De^{-i\pi/2}\eta_0}{\sqrt{2}} \\ &\quad + \frac{Qe^{-i\varphi}\chi_- + De^{-i\pi/2}\eta_-}{2}, \end{aligned} \quad (4.9)$$

$$\begin{aligned} \psi_- &\rightarrow \frac{Qe^{i\varphi}\chi_+ + De^{i\pi/2}\eta_+}{2} + \frac{Qe^{i\varphi}\chi_0 + De^{i\pi/2}\eta_0}{\sqrt{2}} \\ &\quad - \frac{Qe^{i\varphi}\chi_- + De^{i\pi/2}\eta_-}{2}, \end{aligned} \quad (4.10)$$

where  $Q = \sqrt{A^2 + (BC)^2}$ ,  $D = B\sqrt{1 - C^2}$ ,  $\varphi = \arctan(BC/A)$ ,

$$\eta_{\pm} = \frac{\eta'_{\pm} - C\chi_{\pm}}{\sqrt{1 - C^2}}, \quad \eta_0 = \frac{\eta'_0 - C\chi_0}{\sqrt{1 - C^2}}, \quad (4.11)$$

$$\chi_{\pm,0} = \frac{\sqrt{n_{\pm,0}} \cos \phi/2}{A}, \quad \eta'_{\pm,0} = \frac{\sqrt{n_{\pm,0}} \sin \phi/2}{B}. \quad (4.12)$$

The normalisation constants ( $A$  and  $B$ ) and the overlap integral  $C [= \langle \chi_{\pm,0} | \eta'_{\pm,0} \rangle]$  are defined as follows

$$A = \sqrt{\int dz n_{\pm,0} \cos^2 \frac{\phi}{2}}, \quad (4.13)$$

$$B = \sqrt{\int dz n_{\pm,0} \sin^2 \frac{\phi}{2}}, \quad (4.14)$$

$$C = \frac{1}{2AB} \int dz n_{\pm,0} \sin \phi. \quad (4.15)$$

Also, the density  $n_+$  of atomic cloud moving to the right, the density  $n_-$  of atomic cloud moving to the left and the density  $n_0$  of the cloud in the stationary cloud written

in terms of the dimensionless variable  $z$  and parameter  $q$  are

$$\begin{aligned} n_{\pm}(z, q) &= \frac{3}{4} [1 - (z \mp q)^2], \\ n_0(z) &= \frac{3}{4} [1 - z^2]. \end{aligned} \tag{4.16}$$

According to Eqs. (4.9) and (4.10), six basis vectors  $[\chi_{\pm,0}, \eta_{\pm,0}]$  are required to completely describe the three atomic clouds produced by each atomic wave packet  $\psi_{\pm}$  at recombination in the presence of the spatial dependent phase  $\phi$ . The clouds from the wave packets  $\psi_{\pm}$  are obtained from the basis vectors by superposing the appropriate corresponding basis vectors. For instance, a cloud at rest after recombination produced by the wave packet  $\psi_{+}$  is obtained by adding  $\chi_0$  and  $\eta_0$  basis vectors;  $(Qe^{-\varphi}\chi_0/\sqrt{2} + De^{-\varphi}\eta_0/\sqrt{2} = \sqrt{n_0/2}e^{-i\phi/2})$ , see Eq. (4.9). The two basis vectors  $\chi_0$  and  $\eta_0$  are on top of each other as shown in Fig. 4.1. For small values of  $\phi$  ( $\phi \ll 1$ ), the basis set  $\chi$  has an inverted parabolic (or dome) shape and the basis set  $\eta$  has an  $S$ -shape figure as shown in Fig. 4.1a. This is because when  $\phi$  is small,  $\cos \phi/2$  and  $\sin \phi/2$  are slow varying functions of coordinate so that the basis set of the  $\chi$  family is described roughly by the atomic density  $\chi \propto \sqrt{n}$ , and the basis set of the  $\eta$  family is described by the product of the atomic density and the relative phase  $\eta \propto \phi \sqrt{n}$ . At large values of  $\phi$ , both  $\sin \phi/2$  and  $\cos \phi/2$  vary rapidly with coordinate so that both basis sets  $\chi$  and  $\eta$  oscillate rapidly as shown in Fig. 4.1b.

Additional phase  $\xi$  is accumulated due to interatomic interactions that cause the linear superposition of different number states within a cloud to evolve at different rates. The phase  $\xi$  which is not contained within the mean field theory is obtained in the second quantisation, with many-body Hamiltonian as given in Eq. (1) of Ref. [82]. Let  $b_0, b_+, b_-$  be operators that act on vacuum state to create an atom belonging to a cloud at rest, and moving to the right or left respectively. Then,  $\hat{\Psi}$  is expanded in terms of the operators  $b_{\pm}$  and the solution  $\psi_{\pm}(x, t) \left[ = \sqrt{n_{\pm}(x, t)}e^{\mp i\phi(x, t)} \right]$  of the

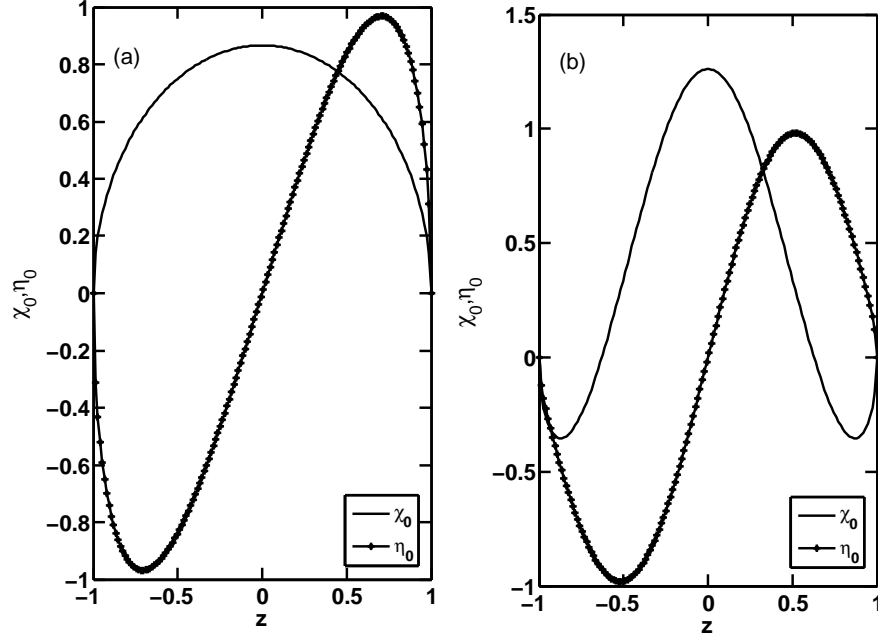


**Figure 4.1** The basis vectors  $\chi_0$  and  $\eta_0$  versus the dimensionless coordinate  $z$ . The parameters for the plots are  $K = 10^{-3}, \Gamma = 0$  for Fig (a) and  $K = 5, \Gamma = 0$  for Fig (b).

Gross-Pitaevskii equation as

$$\hat{\Psi}(x, t) = b_+ \psi_+(x, t) + b_- \psi_-(x, t). \quad (4.17)$$

At recombination, the pulses couple the operators according to the rules Eqs. (4.9) and (4.10)

$$b_+ \rightarrow -\frac{Qe^{-i\varphi}b_{\chi_+} + De^{-i\pi/2}b_{\eta_+}}{2} + \frac{Qe^{-i\varphi}b_{\chi_0} + De^{-i\pi/2}b_{\eta_0}}{\sqrt{2}} + \frac{Qe^{-i\varphi}b_{\chi_-} + De^{-i\pi/2}b_{\eta_-}}{2}, \quad (4.18)$$

$$b_- \rightarrow \frac{Qe^{i\varphi}b_{\chi_+} + De^{i\pi/2}b_{\eta_+}}{2} + \frac{Qe^{i\varphi}b_{\chi_0} + De^{i\pi/2}b_{\eta_0}}{\sqrt{2}} - \frac{Qe^{i\varphi}b_{\chi_-} + De^{i\pi/2}b_{\eta_-}}{2}. \quad (4.19)$$

The state vector before the recombination pulses are applied is given by Eq. (3.16)

$$|\Psi(t)\rangle = \frac{1}{\sqrt{2^N N!}} \sum_{n=0}^N \frac{N!}{n!(N-n)!} e^{i\Phi(t)} \left( b_+^\dagger e^{-i(\theta/2)} \right)^n \times \left( b_-^\dagger e^{i(\theta/2)} \right)^{N-n} |0\rangle, \quad (4.20)$$

$$\Phi(t) = \frac{\xi}{2} [2n^2 + 2(n-N)^2], \quad (4.21)$$

where the phase  $\theta$  is the environment-introduced phase angle defined in Eq. (3.14) [see also Eq. (11) of Ref. [82]] and the phase  $\xi$  is as a result of atom-atom interactions that cause each number state contained within the mode-entangled states of the system during propagation to evolve at different rate and it is defined as

$$\xi = \frac{1}{\hbar} \int_t d\tau U, \quad (4.22)$$

$$U = \frac{g_{1D}}{2} \int dz |\psi_\pm|^4,$$

where  $g_{1D} = 2\hbar\omega a_s$ ,  $\omega = \sqrt{\omega_x\omega_y}$  is the geometric mean transverse frequency and  $a_s$  is the s-wave scattering length. The recombination pulses applied at time  $t = T$  transform the operator according to Eqs. (4.18) and (4.19), and the resulting state vector of the system is

$$|\Psi_{\text{rec}}\rangle = \frac{1}{\sqrt{2^N N!}} \sum_{n=0}^N \frac{N!}{n!(N-n)!} \exp [i\xi (n^2 + (N-n)^2)] e^{-i\theta(n-N/2)} \left[ -Q \frac{(b_{x+}^\dagger - b_{x-}^\dagger) e^{-i\varphi}}{2} - D \frac{(b_{\eta+}^\dagger - b_{\eta-}^\dagger) e^{-i\pi/2}}{2} + \frac{Q e^{-i\varphi} b_{x_0}^\dagger + D e^{-i\pi/2} b_{\eta_0}^\dagger}{\sqrt{2}} \right]^n \left[ Q \frac{(b_{x+}^\dagger - b_{x-}^\dagger) e^{i\varphi}}{2} + D \frac{(b_{\eta+}^\dagger - b_{\eta-}^\dagger) e^{i\pi/2}}{2} + \frac{Q e^{i\varphi} b_{x_0}^\dagger + D e^{i\pi/2} b_{\eta_0}^\dagger}{\sqrt{2}} \right]^{N-n} |0\rangle. \quad (4.23)$$

## 4.2 Probability

The state representing  $n_+$  atoms,  $n_-$  atoms in the clouds that moved to the right and left respectively and  $n_0$  atoms in the cloud at rest is given by

$$|n_+, n_-, n_0\rangle = \sum_{j,k,l}^{n_+, n_-, n_0} \frac{b_{\chi_+}^\dagger{}^j b_{\eta_+}^\dagger{}^{n_+-j}}{\sqrt{j!(n_+-j)!}} \frac{b_{\chi_-}^\dagger{}^k b_{\eta_-}^\dagger{}^{n_- - k}}{\sqrt{k!(n_- - k)!}} \frac{b_{\chi_0}^\dagger{}^l b_{\eta_0}^\dagger{}^{n_0 - l}}{\sqrt{l!(n_0 - l)!}} |0\rangle. \quad (4.24)$$

The probability of getting the state  $|n_+, n_-, n_0\rangle$  after recombination is given by the modulus square of the the probability amplitude  $\langle n_0, n_-, n_+ | \Psi(T) \rangle$

$$P = \sum_{j,k,l}^{n_+, n_-, n_0} \left| \langle 0 | \frac{b_{\chi_+}^\dagger{}^j b_{\eta_+}^\dagger{}^{n_+-j}}{\sqrt{j!(n_+-j)!}} \frac{b_{\chi_-}^\dagger{}^k b_{\eta_-}^\dagger{}^{n_+-k}}{\sqrt{k!(n_+-k)!}} \frac{b_{\chi_0}^\dagger{}^l b_{\eta_0}^\dagger{}^{n_0-l}}{\sqrt{l!(n_0-l)!}} | \Psi_{\text{rec}} \rangle \right|^2. \quad (4.25)$$

The probability  $P$  depends on three phase angles, (i) the environment-introduced phase angle  $\theta$ , (ii) the phase  $\xi$  is a time-dependent phase resulting from different evolution rate of each number state contained within the mode-entangled states of the system during propagation and (iii) the spatial dependent phase  $\phi$  through  $Q$  and  $D$ . The dependence of the probability  $P$  on the phase  $\xi$  when  $\phi = 0$  has been previously described in Sec. 3.3.2 (and in Ref. [82]). This chapter focuses on the understanding the combined effects of the unwanted phases.

### 4.2.1 Probability for $\xi$ equal to zero

Substituting Eq. (4.24) into Eq. (4.25), only terms for which the  $n = n_0$  is selected and the probability  $P_{\xi=0}$  becomes

$$P_{\xi=0} = \frac{2^{n_0-N} N!}{n_+! n_-! n_0!} \left[ Q^2 \cos^2 \left( \frac{\theta}{2} + \varphi \right) + D^2 \cos^2 \left( \frac{\theta}{2} + \frac{\pi}{2} \right) \right]^{n_0} \times \left[ Q^2 \sin^2 \left( \frac{\theta}{2} + \varphi \right) + D^2 \sin^2 \left( \frac{\theta}{2} + \frac{\pi}{2} \right) \right]^{N-n_0}, \quad (4.26)$$

where the conservation of the total population  $n_+ + n_- = N - n_0$  have been used. Note that for  $\phi = 0$ , the angle  $\varphi$  and  $D$  are zero while  $Q$  is unity. Then one recovers

the results in the ideal case obtained in Sec. 3.3.2 where both the interactions and special dependent phases are equal to zero. Using Eq. (4.6) for  $\phi$ , the overlap integral  $C$  is zero and

$$P_{\xi=0} = \frac{2^{n_0-N} N!}{n_+! n_-! n_0!} \left[ Q^2 \cos^2 \left( \frac{\theta}{2} \right) + D^2 \cos^2 \left( \frac{\theta}{2} + \frac{\pi}{2} \right) \right]^{n_0} \times \left[ Q^2 \sin^2 \left( \frac{\theta}{2} \right) + D^2 \sin^2 \left( \frac{\theta}{2} + \frac{\pi}{2} \right) \right]^{N-n_0}. \quad (4.27)$$

The probability  $P_{\xi=0}$  for  $\xi = 0$  could be written as a product of two functions

$$P_{\xi=0} = P_{\pm} P_{0,\xi=0}, \quad (4.28)$$

where  $P_{\pm}$  is the probability of observing  $n_+$  atoms in the cloud moving to right and  $n_-$  atoms in the cloud moving to the left for a given number of  $n_0$  atoms in the central cloud. The properties of the probability function  $P_{\pm}$  is as described in Sec. 3.3.2, [see also Sec. III of Ref. [82]]. The function  $P_{0,\xi=0}$  is the probability of observing  $n_0$  atoms in the cloud at rest for  $\xi = 0$ ,

$$P_{0,\xi=0} = \frac{N!}{n_0!(N-n_0)!} \left[ Q^2 \cos^2 \frac{\theta}{2} + D^2 \sin^2 \frac{\theta}{2} \right]^{n_0} \left[ Q^2 \sin^2 \frac{\theta}{2} + D^2 \cos^2 \frac{\theta}{2} \right]^{N-n_0}. \quad (4.29)$$

The probability  $P_{0,\xi=0}$  depends on the environment-introduced phase angle  $\theta$  and on the phase  $\phi$  through the normalisation constants ( $Q$  and  $D$ ) and is plotted in Fig. 4.2. A prominent feature of Fig. 4.2 is that the peak of the probability function  $P_{0,\xi=0}$  shifts towards one-half of the total number of atoms i.e.  $N/2$  irrespective of the environmental-introduced angle  $\theta$ . Using Stirling's approximation, the probability function  $P_{0,\xi=0}$  is Gaussian

$$P_{0,\xi=0} = \sqrt{\frac{1}{2\pi(\Delta n_0)^2}} \exp \left[ -\frac{1}{2(\Delta n_0)^2} (n_0 - \langle n_0 \rangle)^2 \right], \quad (4.30)$$

with the peak of the probability located by the mean value  $\langle n_0 \rangle$  of the distribution

$$\langle n_0 \rangle = \frac{N}{2} \left( 1 + \cos \theta \int dz n_0(z) \cos \phi(z, q) \right). \quad (4.31)$$

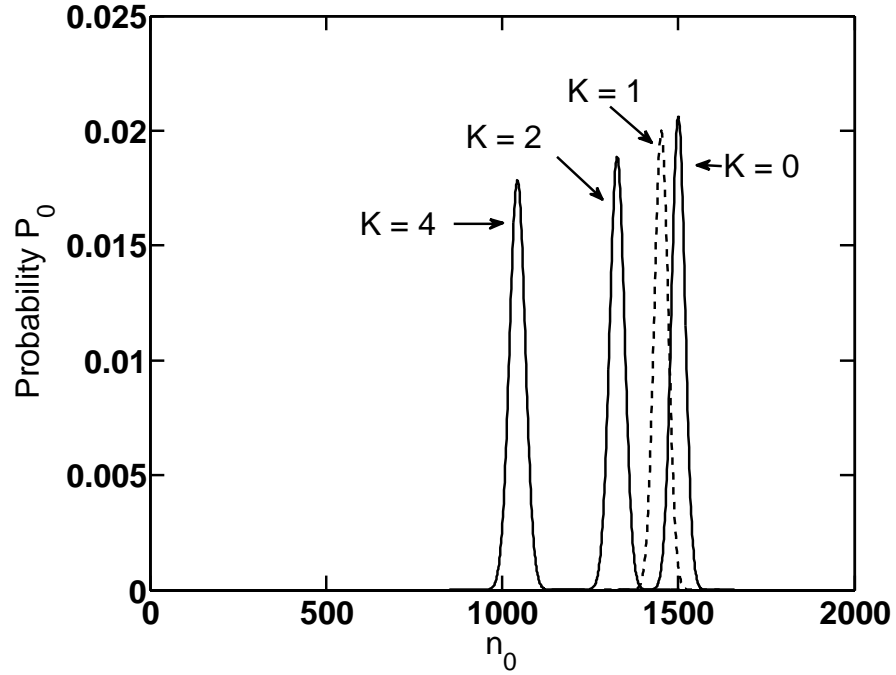


**Figure 4.2** The probability function  $P_0$  versus  $n_0$  at different values of  $K$  for  $N = 2000$ ,  $\theta = \pi/3$  and  $\Gamma = 0$ .

For very small values of  $\phi$ ,  $\cos \phi$  is approximately unity and the mean value in this limit is  $\langle n_0 \rangle \approx N \cos^2(\theta/2)$ . The position of the peak is then determined by the environment-introduced phase angle  $\theta$  as shown in Fig. 4.2. At large values of  $\phi$  ( $|\phi| \gg 1$ ), the function  $n_0(z) \cos \phi(z, q)$  oscillates rapidly so that on average it gives roughly zero, and the position of the peak is approximately located at  $\langle n_0 \rangle \approx N/2$  independent of the phase angle  $\theta$ . The dependence of the mean value on the phase angle  $\phi$  is shown in Fig. 4.3 and demonstrates that the mean value goes to its limiting value which is approximately  $N/2$  at large values of  $\phi$ .

Another parameter of interest in Eq. (4.30) is the standard deviation  $\Delta n_0$ ,

$$\Delta n_0 = \sqrt{\frac{N}{4}} \left[ 1 - \cos^2 \theta \left( \int dz n_0(z) \cos \phi(z, q) \right)^2 \right]^{1/2}, \quad (4.32)$$



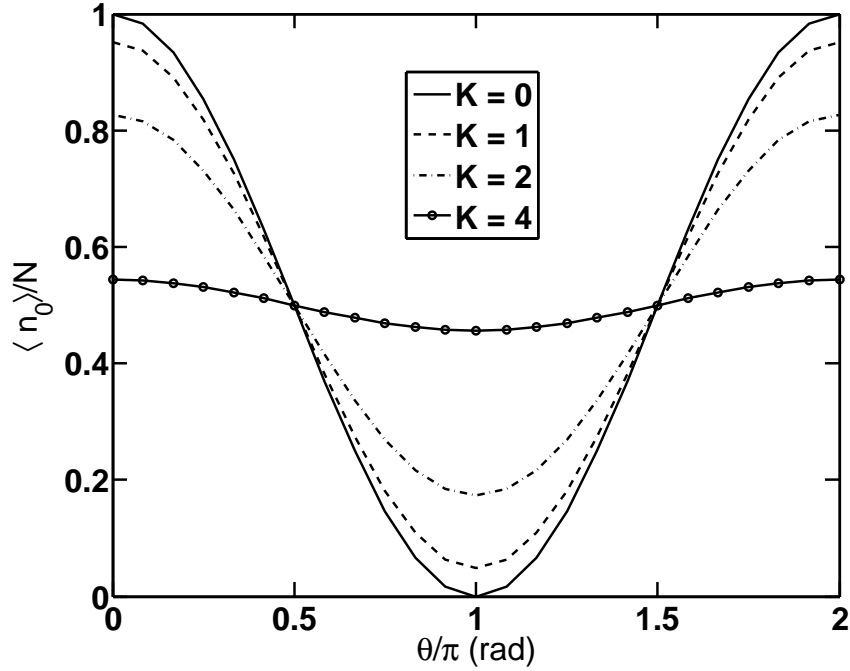


**Figure 4.3** The normalised average number of atoms in the cloud at rest  $\langle n_0 \rangle / N$  versus  $\theta$  for  $N = 2000$  and  $\Gamma = 0$ .

and is plotted in Fig. 4.4. For small values of  $\phi$ , the standard deviation  $\Delta n_0 \approx \left(\sqrt{N/4}\right) (1 - \cos^2 \theta)^{1/2}$ . In this limit the standard deviation is zero at  $\theta = 0, \pi$  or  $2\pi$  and maximum at  $\theta = \pi/2$  and  $3\pi/2$ . The phase angles  $\theta = 0, 2\pi$  corresponds to situation where the all the atoms are known with absolute certainty to be in the cloud at rest and the phase angle  $\theta = \pi$  corresponds to all atoms being in the moving clouds with absolute certainty. In these situations, the width of the distribution is zero. At  $\theta = \pi/2$  or  $3\pi/2$  the width of the distribution albeit standard deviation is maximum and corresponds to observing equal number of atoms between the moving clouds and the cloud at rest with largest possible error.

As the spatial phase  $\phi$  increase, the standard deviation starts showing dependence on the phase angle  $\phi$  and causes the probabilities which were initially

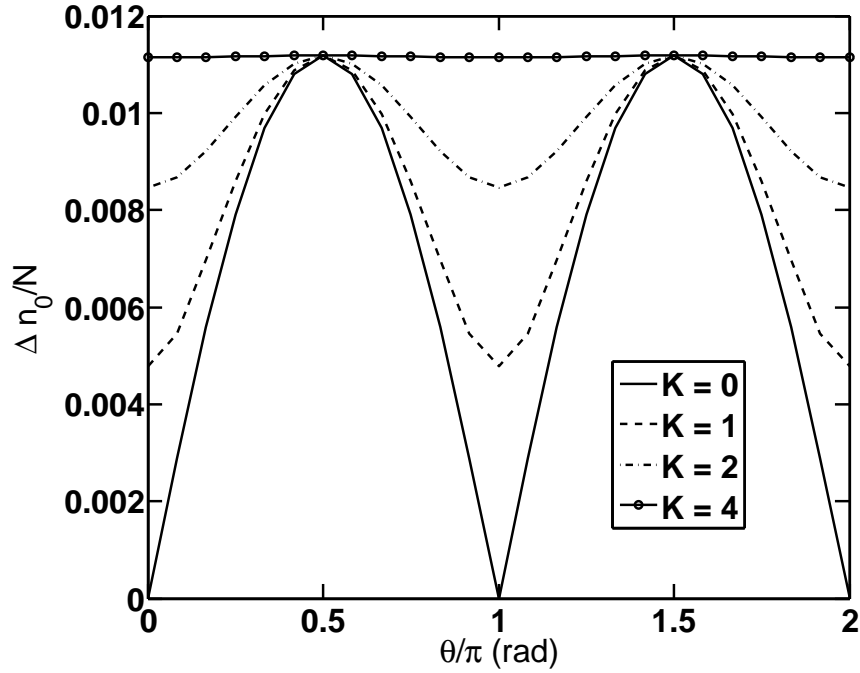


**Figure 4.4** The relative standard deviation  $\Delta n_0/N$  versus  $\theta$  for  $N = 2000$  and  $\Gamma = 0$ .

known with absolute certainty at very small values of  $\phi$  to be known only with some error as shown in Fig. 4.4. The width of the probability is no longer zero for any value of  $\theta$ . At large values of  $\phi$ , the standard deviations shows no sensitivity to changes in the the phase angle  $\theta$  for the same reason explained above. In this limit all width of the of the probability and hence standard deviation have the same value  $\sqrt{N}/2$  as shown in Fig. 4.4.

### 4.2.2 Probability for $\xi$ not equal to zero

Equation (4.23) can be re-arranged such that all creation operators that create an atom say in the right cloud ( $b_{\chi_+}^\dagger, b_{\eta_+}^\dagger$ ) are paired together and vice versa. The probability  $P$  of observing  $n_+$  atoms,  $n_-$  atoms in the clouds that moved to the right and

left respectively and  $n_0$  atoms in the cloud at rest becomes ( $\varphi = 0$ )

$$P = \sum_{j=0, k=0, l=0}^{n_0, n_-, n_+} \left| (Q)^k (De^{i\pi/2})^{n_- - k} (Q)^j (De^{i\pi/2})^{n_0 - j} (Q)^l \times (De^{i\pi/2})^{n_+ - l} \sqrt{\frac{N! j! (n_0 - j)! l! (n_+ - l)! k! (n_- - k)!}{2^{3N - n_0}}} \times \sum_{n=0}^N e^{-i\theta(n - N/2) + i\xi(n^2 + (n - N/2)^2)} S(n_0, n_+, n_-, n, j, k, l) \right|^2. \quad (4.33)$$

The function  $S(n_0, n_+, n_-, n, j, k, l)$  is determined by comparing Eqs. (4.27) and (4.33) at  $\xi = 0$  and evaluating the resulting fourier transform using the steepest descent method. For very large number of atoms, the probability  $P$  becomes

$$P = \frac{N! 2^{n_0 - N}}{n_0! n_-! n_+!} \sum_{j, k, l}^{n_0, n_-, n_+} \frac{(Q^2)^{j+k+l} (D^2)^{N-j-k-l} n_0! n_-! n_+!}{j! (n_0 - j)! k! (n_- - k)! l! (n_+ - l)!} |\Sigma(n_0, j, k, l)|^2. \quad (4.34)$$

where

$$\Sigma(n_0, j, k, l) = \frac{e^{i(m\pi/2 + N^2\xi/2)}}{\sqrt{1 - 2iN\xi}} \left( \sqrt{1 - \frac{m}{N}} \right)^{N-m} \left( \sqrt{\frac{m}{N}} \right)^m \times \left[ e^{-im\pi/2 - N(\theta/2 - x_0)^2 / (1 - 2iN\xi)} + e^{im\pi/2 - N(\theta/2 + x_0)^2 / (1 - 2iN\xi)} \right], \quad (4.35)$$

$m = n_0 - j + k + l$  and  $x_0 = \arctan \sqrt{m/(N - m)}$ .

In presence of both phases  $\phi$  and  $\xi$ , the probability that describes the distribution of atoms in the three clouds that emerge after recombination is given by Eq. (4.34). Shown in Fig. 4.5 and Fig. 4.6 are the contour plots of the probability plotted at different values of  $\phi$  and  $\xi$ . The peak of the probability Eq. (4.34) is located approximately at  $n_- = n_+$  irrespective of the value of  $\phi$  and  $\xi$  and the inserts in those figures are plotted along the line  $n_+ = n_-$ . At small values of  $\phi$  and  $\xi$  plotted in Fig. 4.5 the peak of the probability is located at  $n_0 \sim N \cos^2 \theta/2$  where  $\theta = 2\pi/3$ . The influence of the phase diffusion and spatial relative phase on the operation of the interferometer is negligible. For small values of  $\phi$  and large values of  $\xi$ , the width of the probability function  $P$  becomes of the order of the total population  $N$ . The exponential terms in

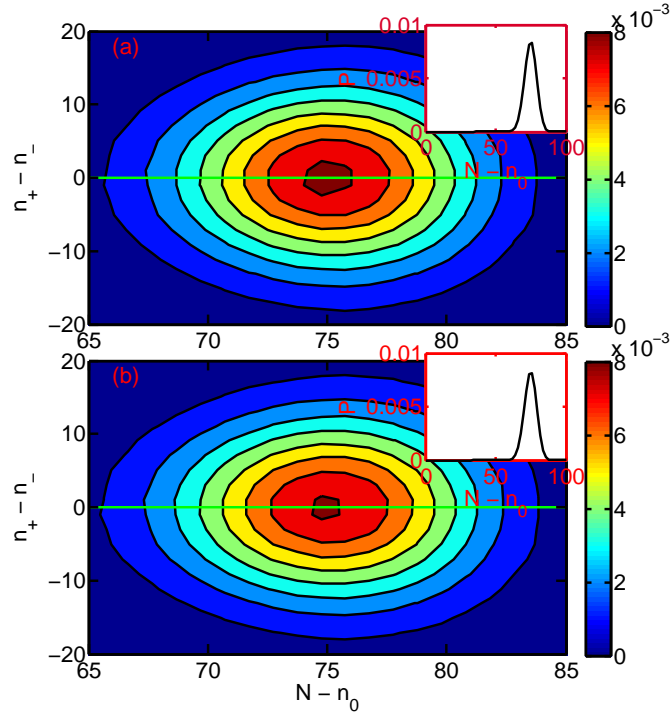


**Figure 4.5** The contour plots of the probability function  $P$  as a function of the relative number of atoms and total number of atoms in the moving clouds after recombination for  $N = 100$  atoms and  $\Gamma = 0$ . In (a)  $\xi\sqrt{N} = 0$ ,  $K = 0$  and in (b)  $\xi\sqrt{N} = 0.01$ ,  $K = 0.01$ . The inserts are plotted along the green line.

Eq. (4.34) interferes as discussed in Ref. [82] which manifest as appearance of islets of peaks in the contour plots of the probability shown in Fig. 4.6(a) that are seen as oscillations in the insert. Similarly, for large values of  $\phi$  and small values of  $\xi$  plotted in Fig. 4.6(b), there is no noticeable change in the width of the probability function  $P$ . However the peak of the distribution has moved towards one-half of the total population of atoms  $N$  in accordance to the results of Sec 4.2.1. At large values of  $\phi$  and  $\xi$ , the probability function  $P$  is exactly one-half of the total population  $N$  as shown in Fig. 4.6(c). Notice that the interference effects resulting from the large values  $\xi$  is totally suppressed. This is because the overall amplitude of the probability

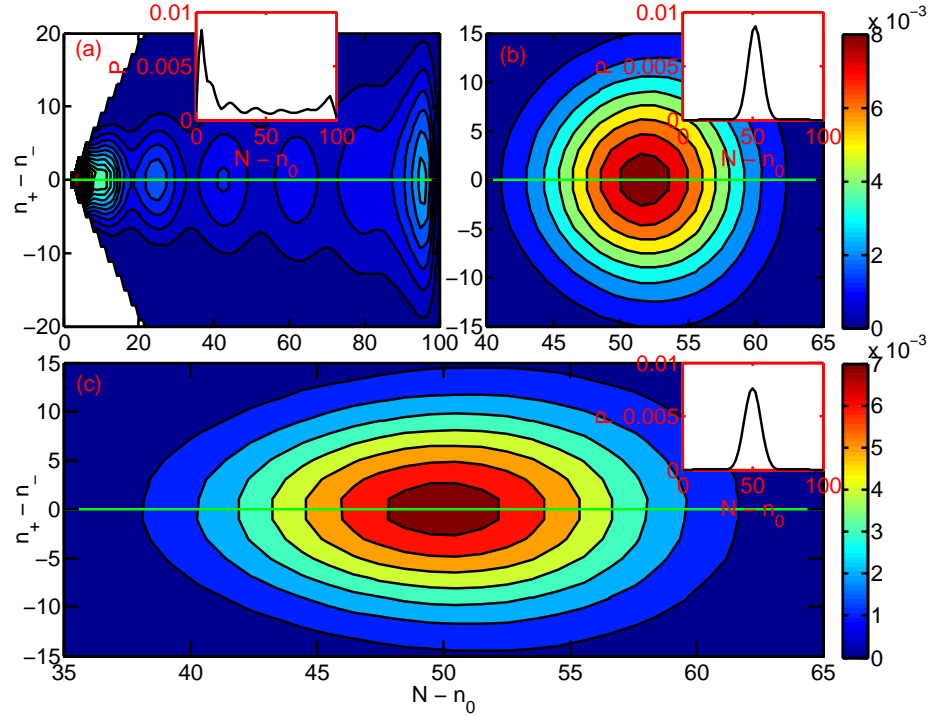


**Figure 4.6** The contour plots of the probability function  $P$  as a function of the relative number of atoms and total number of atoms in the moving clouds after recombination for  $N = 100$  atoms and  $\Gamma = 0$ . The parameters of the plots are as follows; in (a)  $\xi\sqrt{N} = 1$ ,  $K = 1$ , in (b)  $\xi\sqrt{N} = 0.1$ ,  $K = 5$  and in (c)  $\xi\sqrt{N} = 1$ ,  $K = 5$ . The inserts are plotted along the green line.

function  $P$ , which depends on the spatial relative phase  $\phi$  through  $Q$  and  $D$ , is very small at large values of  $\phi$  except at values of  $N - n_0$  close to  $N/2$ , thereby suppressing the interference effects. The suppression of the interference effect is also evident on the insert shown in Fig. 4.6(c).

#### Approximate expression for probability function at small values of $\phi$

To gain more insight into the behaviour of the probability function  $P$ , we consider very small values of spatial relative phase  $\phi$ . For small values of  $\phi$  ( $|\phi| \ll 1$ ),  $D$  is very small while  $Q$  is roughly of order unity. The probability  $P$  is then written to the

lowest order terms in  $D$ . Keeping terms to order  $D^2$  in Eq. (4.34), the probability function  $P$  is written as

$$P \approx P_{\pm} P_{n_0}, \quad (4.36)$$

where

$$P_{\pm} = \frac{2^{n_0-N} (N - n_0)!}{n_+! n_-!}, \quad (4.37)$$

and

$$P_{n_0} = P_0 + P_{-1} + P_{+1}. \quad (4.38)$$

The properties of the probability function  $P_{\pm}$  are well described in Sec. 3.3.2. The probability  $P_{n_0}$  of observing  $n_0$  atoms in the central cloud consists of three terms. The first term  $P_0$  is the zeroth order term in  $D$  of the probability function  $P_{n_0}$  and corresponds to the contribution from term that peak at  $n_0 = N \cos^2 \frac{\theta}{2}$ ,

$$P_0 = \frac{Q^{2N}}{\sqrt{1 + 4N^2\xi^2}} \sqrt{\frac{N}{2\pi n_0(N - n_0)}} \left| \left[ e^{-i(N-n_0)\pi/2 - N(\theta/2-x_0)^2/(1-2iN\xi)} + e^{i(N-n_0)\pi/2 - N(\theta/2+x_0)^2/(1-2iN\xi)} \right] \right|^2, \quad (4.39)$$

where  $x_0 = \arctan \sqrt{\frac{N-n_0}{n_0}}$ , and Stirling's approximation had been used in writing Eq. (4.39). The other two terms  $P_{-1}$  and  $P_{+1}$  are corrections to  $P_0$  coming from terms that peak at  $n_0 - 1 = N \cos^2 \frac{\theta}{2}$  and  $n_0 + 1 = N \cos^2 \frac{\theta}{2}$  respectively and are of order  $D^2$ . Using Stirling's approximation, one writes  $P_{-1}$  and  $P_{+1}$  as follows

$$P_{-1} = \frac{(Q^2)^{N-1} D^2}{\sqrt{1 + 4N^2\xi^2}} \sqrt{\frac{N(N - n_0 + 1)}{2\pi(n_0 - 1)}} \left| \left[ e^{-i(N-n_0+1)\pi/2 - N(\theta/2-x_-)^2/(1-2iN\xi)} + e^{i(N-n_0+1)\pi/2 - N(\theta/2+x_-)^2/(1-2iN\xi)} \right] \right|^2, \quad (4.40)$$

$$P_{+1} = \frac{(Q^2)^{N-1} D^2}{\sqrt{1 + 4N^2\xi^2}} \sqrt{\frac{N(n_0 + 1)}{2\pi(N - n_0 - 1)}} \left| \left[ e^{-i(N-n_0-1)\pi/2 - N(\theta/2-x_+)^2/(1-2iN\xi)} + e^{i(N-n_0-1)\pi/2 - N(\theta/2+x_+)^2/(1-2iN\xi)} \right] \right|^2, \quad (4.41)$$

where  $x_- = \arctan \sqrt{\frac{N-n_0+1}{n_0-1}}$  and  $x_+ = \arctan \sqrt{\frac{N-n_0-1}{n_0+1}}$ .

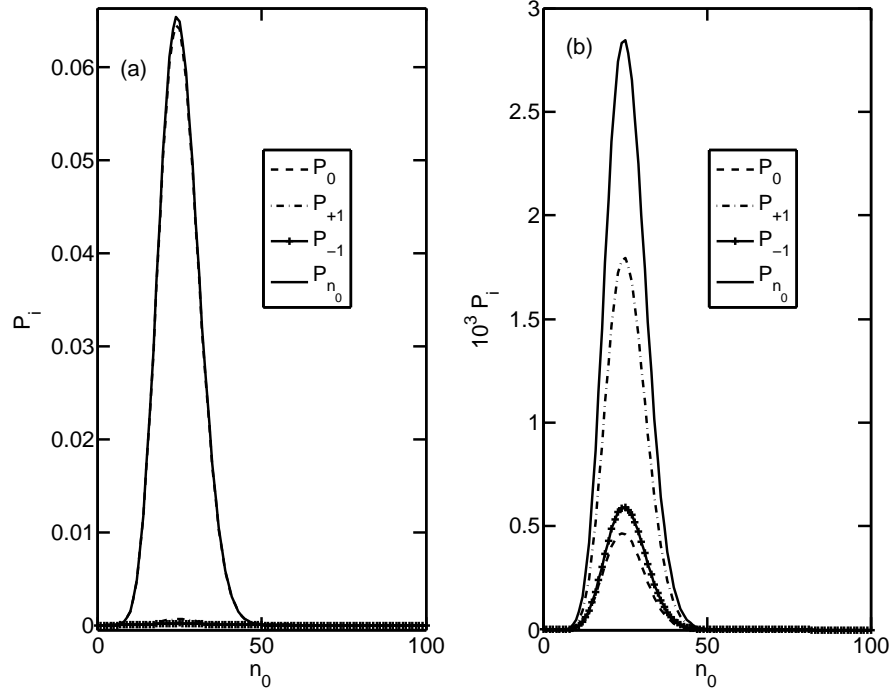


**Figure 4.7** The probability function  $P_{n_0}$  and its constituents versus  $n_0$  for  $N = 100$  atoms at  $\theta = 2\pi/3$ ,  $\Gamma = 0$  and  $\xi = 0.05/\sqrt{N}$ . Fig (a) is plotted at  $K = 0.05$  and Fig (b) is plotted at  $K = 1$ .

For  $|\phi| \ll 1$  both  $P_{+1}$  and  $P_{-1}$  are negligible and the dominant contribution to  $P_{n_0}$  comes from the term  $P_0$  as shown in Fig. 4.7a. Increasing the value of  $\xi$  broadens the width of the probability density  $P_{n_0}$ . The function  $P_{n_0}$  has been studied previously in Chap. 3 [see also Ref [82]] and needs no further analysis. As  $\phi$  increases, the values of  $|Q|$  and  $|D|$  are significantly different from unity and zero respectively, thereby causing significant decrease in the height of  $P_0$ . Also, the correction terms  $P_{-1}$  and  $P_{+1}$  are no longer negligible. For  $|\phi|$  values that are comparable to unity  $|\phi| \sim 1$ , the approximation breaks down and the dominant contribution comes from the term  $P_{-1}$  or  $P_{+1}$  depending on the value of  $\theta$ . For  $0 \leq \theta/2 < \pi/4$ , the dominant contribution

comes from  $P_{-1}$  and the probability function  $P$  approaches  $N/2$  from the right, while for  $\pi/4 < \theta/2 \leq \pi/2$  the dominant contribution comes from  $P_{+1}$  and the probability function  $P$  approaches  $N/2$  from the left. For  $\theta/2 = \pi/3$  shown in Fig. 4.7b, the dominant contribution comes from  $P_{+1}$  that peaks at  $n_0 + 1 = N \cos^2 \frac{\theta}{2}$ . The shift in peak of the distribution  $P_0$  from  $n_0 = N \cos^2 \frac{\theta}{2}$  to  $n_0 + 1 = N \cos^2 \frac{\theta}{2}$  at increasing value of  $\phi$  explains the shifts in the probability density  $P$  observed in Fig. 4.6b and Fig. 4.6c and suggests that full expression Eq. (4.34) has to be used while calculating the probability  $P$  in the presence of  $\phi$ .

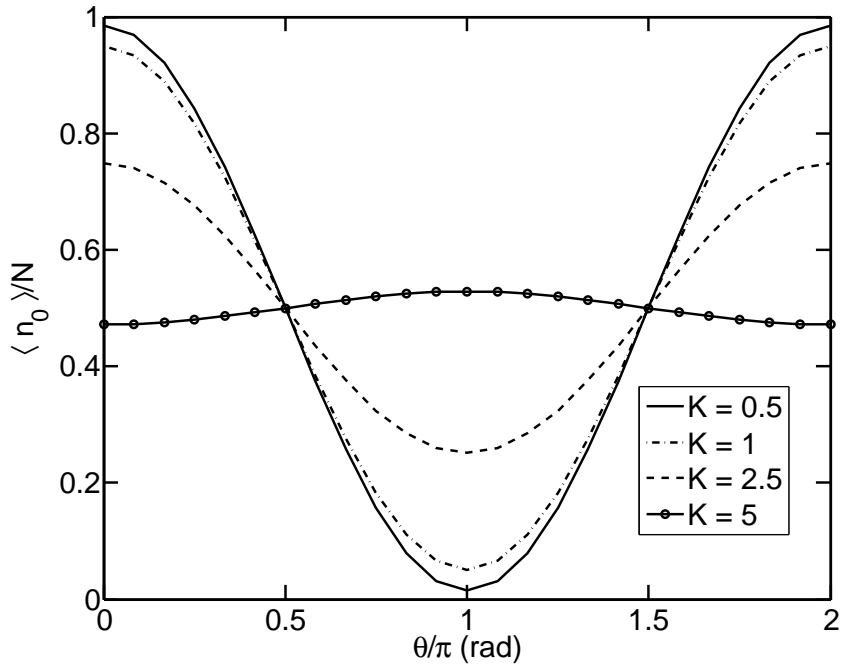


**Figure 4.8** The relative mean value of atoms in the cloud at rest after recombination versus the phase angle  $\theta$  at  $\xi = 0.05/\sqrt{N}$  and  $\Gamma = 0$ .



### 4.2.3 Moments of the probability function

The moments of the probability function like the mean value and standard deviation are also affected by the variations in the spatial phase and the nonlinear phase per atom. Figures 4.8 and 4.10 show that the relative mean value of the populations found in the cloud at rest after recombination were sensitive to the phases  $\phi$  and  $\xi$ , and demonstrate that increases in either phase or both phases would eventually lead to the loss of interference fringes. Similar results for the standard deviation shown in Figs. 4.9 and 4.11 demonstrate that increases in the phases cause large shot-to-shot fluctuations in the population of atoms in the output ports of the cold-atom interferometer. These results are understood by calculating the moments of the approximate probability function  $P_{n_0}$  when the spatial dependent phase is small. For example, when  $\phi$  ( $|\phi| \ll 1$ ) is very small the dominant contribution to the averages comes from points around  $n_0 = N \cos^2(\theta/2)$  in the probability function  $P_{n_0}$  and the mean evaluates to

$$\langle n_0 \rangle_0 = (Q^2)^N \frac{N}{2} \left( 1 + e^{-\frac{1}{2\alpha}} \cos \theta \right) \quad (4.42)$$

where  $\alpha = N/(1 + 4N^2\xi^2)$ . The correction to the mean is given by

$$\begin{aligned} \langle n_0 \rangle_{+1} &= \frac{N^2}{8} (Q^2)^{N-1} D^2 \left[ 3 + e^{-2/\alpha} \cos 2\theta + 4e^{-1/(2\alpha)} \cos \theta + \right. \\ &\quad \left. - \frac{4}{N} (1 + e^{-1/(2\alpha)} \cos \theta) \right], \\ \langle n_0 \rangle_{-1} &= \frac{N^2}{8} (Q^2)^{N-1} D^2 \left[ 1 - e^{-2/\alpha} \cos 2\theta + \frac{4}{N} (1 - e^{-1/(2\alpha)} \cos \theta) \right]. \end{aligned} \quad (4.43)$$

As  $\phi$  increases, the dominant contribution to the mean value  $\langle n_0 \rangle$  comes from the points around  $n_0 \pm 1 = N \cos^2(\theta/2)$  depending on the value of  $\theta$  as explained previously. At very large values of  $\phi$ , the moments  $\langle n_0 \rangle$  and  $(\Delta n_0)^2$  calculated using the probability  $P_{n_0}$  is very small because  $(Q^2)^{N-1} D^2$  and  $(Q^2)^N$  are small (i.e. the

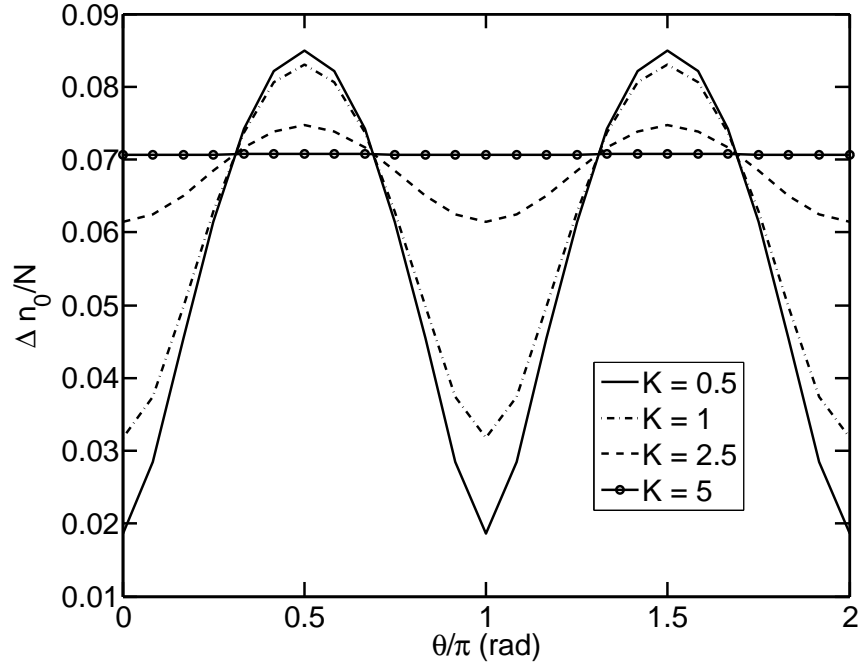


**Figure 4.9** The relative standard deviation of atoms in the cloud at rest after recombination versus the phase angle  $\theta$  at  $\xi = 0.05/\sqrt{N}$  and  $\Gamma = 0$ .

approximation  $P_{n_0}$  breaks down as shown in Fig. 4.7b). So neither terms whose peaks are at  $n_0 \pm 1 = \cos^2(\theta/2)$  make significant contribution to the averages. In this situation, all the terms in Eq. (4.34) are needed to correctly calculate the averages of the distribution and explains the gradual slip of the relative mean value towards one-half shown in Fig. 4.8 and large shot-to-shot variations in the standard deviation shown in Fig. 4.9. Similarly, when the phase  $\phi$  is very small, then only  $P_0$  is sufficient to calculate the moments of the distribution plotted in Figs. 4.10 and 4.11. The changes in the moments  $\langle n_0 \rangle$  and  $(\Delta n_0)^2$  with increasing  $\xi$  has been studied in Chp. 3 and elsewhere [82]. Note that in the averages, the phase  $\phi$  regulates the overall amplitude of the averages through  $Q$  and  $D$ , while the phase  $\xi$  regulates only phase  $\theta$  through  $\alpha$ . As such effects from  $\xi$  on the mean value (albeit fringe pattern) would

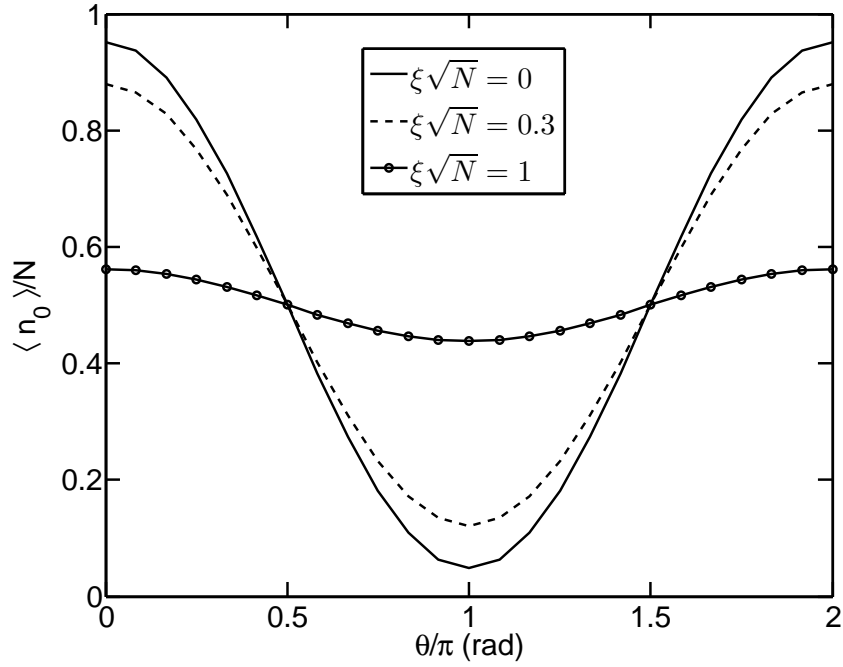


**Figure 4.10** The relative mean value of atoms in the cloud at rest after recombination versus the phase angle  $\theta$  at  $K = 1$  and  $\Gamma = 0$ .

be very hard to observe at large values of phase  $\phi$ .

So far we have shown that increasing spatial phase mask the dependence of the probability function on the environment-introduced phase angle by scrambling the relative phase of the two counter propagating clouds during the interferometric cycle. This manifests as shifts of the probability towards one-half of the total population. We also showed that phase diffusion is responsible for the increased width of the probability observed at the end of the interferometric cycle.

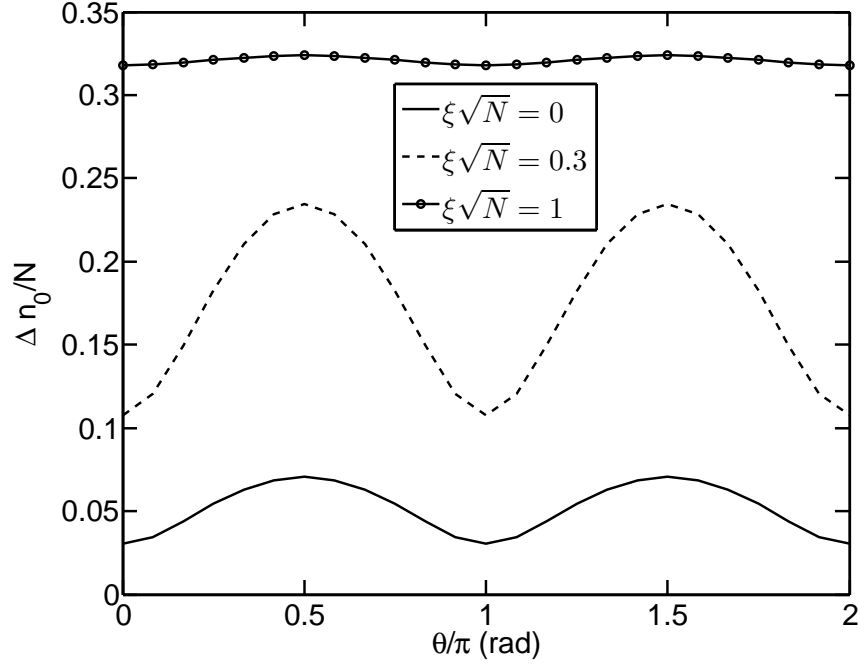


**Figure 4.11** The relative standard deviation of atoms in the cloud at rest after recombination versus the phase angle  $\theta$  at  $K = 1$  and  $\Gamma = 0$ .

### 4.3 Optimisation of interference fringe contrast

Both spatial relative phase and phase diffusion limits the measurement precision of BEC-based atom interferometers, which can be improved by optimising the interference fringe contrast. This offers a way to tune or control the performance of the interferometers in experimentally-controlled parameter space.

Consider the limit where the nonlinear phase per atom  $\xi$  is small and negligible. The relative mean value of the population of atoms in the cloud at rest is  $\langle n_0 \rangle / N = (1/2)(1 + V \cos \theta)$ , (See Eq. (4.31)). The function  $V$  called the contrast is defined as

$$V = \int dz n_0(z) \cos \phi(z, q). \quad (4.44)$$

In the limit of interest where the magnitude of  $\phi(z, q)$  is approximately unity, the contrast  $V$  is evaluated by expanding the cosine function keeping terms only to second order in phase  $\phi(\eta, q)$ . The result is  $V \approx 1 - f$ , where the function  $f$ , which measures the amount by which the contrast  $V$  is different from unity, is

$$f = \frac{1}{10} \left( \Delta K^2 + \frac{6}{7} \Delta K \Gamma + \frac{5}{21} \Gamma^2 \right), \quad (4.45)$$

and  $K$  and  $\Gamma$  are defined in Eq. (4.8). A contrast value of unity means that  $f = 0$  and a contrast value of zero implies that  $f$  is unity. The limit on  $f$  is arbitrarily set to one-half,  $f \leq 1/2$ , and corresponds to observing a contrast value that is 50% or more. Near the end of the interferometric cycle, the dimensionless strength  $S$  of the cubic phase is [85]

$$S = -\frac{35}{V_0} |q|^3. \quad (4.46)$$

For a single reflection interferometer, the change in the dimensionless speed [85] at recombination is

$$\Delta V = \frac{1}{V_0} \left[ \frac{V_0^2 T^2 - 2}{4} \right], \quad (4.47)$$

where  $T \geq R$ , that is the clouds completely separate after splitting pulses are applied. Since the center of masses of the two clouds are not exactly on top of each other at recombination,  $q$  is very small. The strength of the effective dimensionless linear phase  $K$  to first order in  $q$  becomes

$$K = \left[ \frac{R_T}{V_0} \frac{V_0^2 T^2 - 2}{4} - G_T q \right] \frac{1}{\epsilon}, \quad (4.48)$$

Similarly, the strength of the effective dimensionless cubic phase is

$$\Gamma = -\frac{35}{6\epsilon V_0} |q|^3. \quad (4.49)$$

Substituting the values of  $K$  and  $\Gamma$  into the function  $f$  Eq. (4.45), one writes

$$f_S = \frac{1}{10\epsilon^2 V_0^2} \left[ \left( \frac{V_0^2 T^2}{4} - \frac{1}{2} + \frac{V_0 T}{2} q \right)^2 - 5 \left( \frac{V_0^2 T^2}{4} - \frac{1}{2} + \frac{V_0 T}{2} q \right) |q|^3 \right], \quad (4.50)$$

where  $G_T = -T/2$  [63] and we have assumed that the value of  $R_T$  at recombination is roughly of the order unity. The function  $f_S$  depends on the dimensionless distance  $V_0 T$  traveled during interferometric time. For traveled distances that are large in comparison to the radial size of the clouds  $V_0 T \gg 1$ , the clouds separate and  $f_S$  has the following form

$$f_S = \frac{1}{10\epsilon^2 V_0^2} \left( \frac{V_0 T}{2} \right)^4 \left[ 1 + \frac{4}{V_0 T} q \right]. \quad (4.51)$$

It is evident from Eq. (4.51) that the function  $f$  cannot be optimised by minimising it with respect to  $q$  because when  $V_0 T \gg 1$ ,  $1/(V_0 T) \approx 0$ . Similar conclusion was reached previously in Ref. [63]. Requiring that the function  $f$  be less than one half implies that

$$\left( \frac{V_0 T}{2} \right)^4 \leq 5\epsilon^2 V_0^2. \quad (4.52)$$

Similarly for a double reflection interferometer both  $G_T$  [63] and  $\Delta V$  [85] are given by

$$\Delta V = -\frac{3T^2}{20V_0}, \quad (4.53)$$

$$G_T \approx -\frac{7}{16}T. \quad (4.54)$$

The function  $f$  in the case of double reflection interferometer becomes

$$f_D = \frac{1}{10\epsilon^2} \left[ T^2 \left( -\frac{3T}{20V_0} + \frac{7}{16}q \right)^2 - \left( -\frac{3T}{20V_0} + \frac{7}{16}q \right) \frac{5T}{V_0} |q|^3 \right]. \quad (4.55)$$

For dimensionless interferometric times that are much less than than the initial dimensionless speed of the atomic clouds  $T/V_0 \ll 1$ , the function  $f_D$  is

$$f_D \approx \frac{T^2}{10\epsilon^2} \left( -\frac{21}{160} \frac{T}{V_0} q + \frac{49}{256} q^2 \right). \quad (4.56)$$

The function  $f_D$  Eq. (4.56) could be optimised by minimising it with respect to  $q$ .

The value of  $q$  that minimises the function  $f_D$  is

$$q_m = \frac{12}{35} \frac{T}{V_0}. \quad (4.57)$$

At this value of  $q_m$ , the function  $f$  is

$$f_D = -\frac{9}{4000} \frac{T^2 T^2}{\epsilon^2 V_0^2}. \quad (4.58)$$

Requiring that  $|f|$  be at most one-half implies that

$$3T^2 \leq 20\sqrt{5}\epsilon V_0. \quad (4.59)$$

In the double reflection interferometer at the least 50% contrast is measured when Eq. (4.59) is met provided that the interferometric time is much less than the initial speed of the clouds. For times longer than the initial speed, contrast of 50% or more would be observed only if the clouds do not separate. This is because on a time scale comparable to or greater than the initial speed other decoherence mechanisms come into play. The possible way for the clouds to still maintain their coherence is if there is a weak link between them.

Nonlinear phase per atom defined in Eq. (4.22) is a possible source of such decoherence mechanism at longer times. The evaluation of the phase  $\xi$  using Eq. (4.22) gives

$$\xi = \frac{3^{2/3}}{5} \left( \frac{M\omega_{\perp}^2}{\hbar\omega} a_s^2 \right)^{1/3} \left( \frac{1}{N} \right)^{1/3} \omega T. \quad (4.60)$$

When the phase due to interatomic interactions is present and the spatial relative phase is small and negligible, more than 50% fringes is observed if the contrast  $V = e^{-1/(2\alpha)}$  [Eq. (4.42)] is about 60% [see Fig. 3.10]. This corresponds to  $1/(2\alpha) \approx \xi\sqrt{N} \leq 1/2$  or in terms of measurable experimental quantities

$$f_P = \frac{\hbar}{M\omega^2\omega_{\perp}^2 a_s^2 T^3 N^{1/2}} \geq \frac{72}{125} \approx 0.6. \quad (4.61)$$

Since  $f_P \propto \{T^3(\omega_{\perp}\omega)^2 N^{1/2}\}^{-1}$ , one could make  $f_P$  small by manipulating the total number  $N$  of atoms, the trap frequencies  $\omega_{\perp}$ ,  $\omega$  and the the time  $T$  of the experiment. For instance, the phase due to interatomic interactions is reduced by using fewer atoms

$N$  in experiment, and by the use of traps with smaller frequencies while increasing the time of the experiment. Re-expressing the Eqs. (4.52) and (4.59) in terms of dimensional measurable quantities gives

$$f_S = \frac{\hbar^2}{Na_s M^2 \omega_\perp \omega^4 v_0^3 T^6} \geq \frac{9}{64\sqrt{5^3}} \approx 0.01, \quad (\text{Single Reflection}), \quad (4.62)$$

$$f_D = \frac{v_0}{N\omega_\perp a_s \omega^2 T^2} \geq \frac{9}{20\sqrt{5}} \approx 0.2, \quad (\text{Double Reflection}), \quad (4.63)$$

respectively. The parameters  $f_S$  and  $f_D$  measure the amount by which contrast due to spatial phase distortion is different from unity in a single-reflection and double-reflection interferometer respectively.

For a given atomic specie, the mass  $M$ , initial speed  $v_0$  imparted by the splitting laser pulses and the s-wave scattering length  $a_s$  are fixed. Then  $f_S \propto (N\omega_\perp \omega^4 T^6)^{-1}$ . Since the goal is to maximise time  $T$  of the experiment, one is left with manipulating the total number  $N$  and the trapping frequencies. Already the numerator of  $f_S$  is very small, so the total number and trapping frequencies have to be made small in order to increase the contrast in single-reflection interferometer. This conclusion was previously arrived at in Ref. [62]. In double reflection interferometer, the situation is different; the numerator is roughly  $\sim 10^{-2}$ . For a given atomic specie,  $f_D \propto (N\omega_\perp \omega^2 T^2)^{-1}$ . The spatial phase distortion could be minimised by reducing the the total number  $N$  of atoms used in experiment, use traps with smaller frequencies while increasing the time of the experiment.

## 4.4 Discussion

Guided-wave atom interferometer using BEC has been demonstrated in several experiments [31, 53, 59]. In the earliest experiment [31], a single reflection atom-Michelson interferometer was used to interfere a BEC cloud containing  $10^5$   $^{87}\text{Rb}$  atoms. The



transverse and longitudinal frequencies of the trap are 177 Hz and 5 Hz respectively. The propagation time was up to 10 ms and the initial speed of the cloud  $v_0 = 11.7$  mm/s. For these parameters and value of the s-wave scattering length  $a_s = 5.2 \times 10^{-9}$  m,  $f_S = 6 \times 10^{-7}$  is several orders of magnitude less than 0.01 and  $f_P = 70$ . The loss of contrast in the experiment is due to spatial phase that was accumulated by the clouds during the propagation time.

Similar experiments were performed in Ref. [59]. The frequencies of the trap used in the experiment are  $(\omega_x, \omega_y, \omega_z) = 2\pi(6.0, 3.3, 1.2)$  Hz respectively. The trap was used to confine and manipulate about  $3 \times 10^4$   $^{87}\text{Rb}$  atoms for propagation times up to 12 ms. The values of  $f_S$  and  $f_P$  evaluated at these parameters are  $f_S = 0.01$  and  $f_P = 2 \times 10^6$ , and show that the loss of contrast is due to spatial phase accumulated by the two moving clouds during their propagation. A double reflection realised in the same geometry [53] was used to manipulate about  $10^4$   $^{87}\text{Rb}$  atoms for a propagation time of about 44 ms. The  $f_S$  and  $f_P$  values for these parameters are 90 and  $8 \times 10^4$  respectively. These values suggest that more than 50% of contrast is observed and the loss of contrast is more likely to be due to spatial phase distortion than phase diffusion. Even though phase diffusion is not remotely the cause loss of contrast in the experiment, the value  $f_P$  in the double reflection interferometer is two order of magnitude smaller than the value of  $f_P$  in the single reflection interferometer. This is because the double reflection interferometer was operated at a longer propagation time.

Recently, it [85] was shown that a contrast of at the least one-half could be measured in a free oscillation interferometer if

$$f_F = \frac{Mv_0^4}{\hbar\omega_{\perp}^2\omega a_s^2 N^2} \geq 0.1.$$

Such an interferometer was realised [61] and used to trap and manipulate about  $10^5$

---

$^{87}\text{Rb}$  atoms [83]. The transverse and longitudinal frequencies of the trap are 80 Hz and 4.1 Hz respectively. The atoms were allowed to propagate for a time corresponding to the longitudinal period of the trap  $T = 2\pi/\omega$ . At these values, the parameter  $f_P = 0.04$  and  $f_F = 7 \times 10^3$ . The loss of contrast in this experiment is more likely to be as a result of phase diffusion because the duration of the experiment allowed for significant accumulation of the phase due to interatomic interactions.

# Bibliography

- [1] A. Einstein, “Quantentheorie des einatomigen idealen Gases: Zweite Abhandlung,” *Sitzungsber. Preuss. Akad. Wiss.* p. 18 (1925).
- [2] S. N. Bose, “Plancks Gesetz und Lichtquantenhypothese,” *Z.Phys.* **26**, 178–181 (1924).
- [3] F. London, “On the Bose-Einstein Condensation,” *Phys. Rev.* **54**, 947–954 (1938).
- [4] C. E. Hecht, “The possible superfluid behaviour of hydrogen atom gases and liquids,” *Physica* **25**, 1159–1161 (1959).
- [5] W. C. Stwalley and L. H. Nosanow, “Possible “New” Quantum Systems,” *Phys. Rev. Lett.* **36**, 910–913 (1976).
- [6] D. A. Bell, H. F. Hess, G. P. Kochanski, S. Buchman, L. Pollack, Y. M. Xiao, D. Kleppner, and T. J. Greytak, “Relaxation and recombination in spin-polarized atomic hydrogen,” *Phys. Rev. B* **34**, 7670–7697 (1986).
- [7] H. F. Hess, G. P. Kochanski, J. M. Doyle, N. Masuhara, D. Kleppner, and T. J. Greytak, “Magnetic trapping of spin-polarized atomic hydrogen,” *Phys. Rev. Lett.* **59**, 672–675 (1987).

- 
- [8] H. F. Hess, “Evaporative cooling of magnetically trapped and compressed spin-polarized hydrogen,” *Phys. Rev. B* **34**, 3476–3479 (1986).
- [9] M. H. Anderson, J. R. Ensher, M. R. Matthews, C. E. Wieman, and E. A. Cornell, “Observation of Bose-Einstein Condensation in a Dilute Atomic Vapor,” *Science* **269**, 198–201 (1995).
- [10] C. C. Bradley, C. A. Sackett, J. J. Tollett, and R. G. Hulet, “Evidence of Bose-Einstein Condensation in an Atomic Gas with Attractive Interactions,” *Phys. Rev. Lett.* **75**, 1687–1690 (1995).
- [11] K. B. Davis, M. O. Mewes, M. R. Andrews, N. J. van Druten, D. S. Durfee, D. M. Kurn, and W. Ketterle, “Bose-Einstein Condensation in a Gas of Sodium Atoms,” *Phys. Rev. Lett.* **75**, 3969–3973 (1995).
- [12] D. G. Fried, T. C. Killian, L. Willmann, D. Landhuis, S. C. Moss, D. Kleppner, and T. J. Greytak, “Bose-Einstein Condensation of Atomic Hydrogen,” *Phys. Rev. Lett.* **81**, 3811–3814 (1998).
- [13] F. P. D. Santos, J. Léonard, J. Wang, C. J. Barrelet, F. Perales, E. Rasel, C. S. Unnikrishnan, M. Leduc, and C. Cohen-Tannoudji, “Bose-Einstein Condensation of Metastable Helium,” *Phys. Rev. Lett.* **86**, 3459–3462 (2001).
- [14] A. Robert, O. Sirjean, A. Browaeys, J. Poupard, S. Nowak, D. Boiron, C. I. Westbrook, and A. Aspect, “A Bose-Einstein Condensate of Metastable Atoms,” *Science* **292**, 461 (2001).
- [15] T. Weber, J. Herbig, M. Mark, H. Nägerl, and R. Grimm, “Bose-Einstein Condensation of Cesium,” *Science* **299**, 232 (2003).

- [16] S. Stellmer, M. K. Tey, B. Huang, R. Grimm, and F. Schreck, “Bose-Einstein Condensation of Strontium,” *Phys. Rev. Lett.* **103**, 200401 (2009).
- [17] M. Y. N. de Escobar, P. G. Mickelson, M. Yan, B. J. DeSalvo, S. B. Nagel, and T. C. Killian, “Bose-Einstein Condensation of  $^{84}\text{Sr}$ ,” *Phys. Rev. Lett.* **103**, 200402 (2009).
- [18] M. Greiner, C. A. Regal, and D. S. Jin, “Emergence of a molecular BoseEinstein condensate from a Fermi gas,” *Nature* **426**, 537–540 (2003).
- [19] S. Jochim, M. Bartenstein, A. Altmeyer, G. Hendl, S. Riedl, C. Chin, J. H. Denschlag, and R. Grimm, “Bose-Einstein Condensation of Molecules,” *Science* **302**, 2101 (2003).
- [20] M. W. Zwierlein, C. A. Stan, C. H. Schunck, S. M. F. Raupach, S. Gupta, Z. Hadzibabic, and W. Ketterle, “Observation of Bose-Einstein Condensation of Molecules,” *Phys. Rev. Lett.* **91**, 250401 (2003).
- [21] C. A. Regal, M. Greiner, and D. S. Jin, “Observation of Resonance Condensation of Fermionic Atom Pairs,” *Phys. Rev. Lett.* **92**, 040403 (2004).
- [22] M. R. Andrews, C. G. Townsend, H. J. Miesner, D. S. Durfee, D. M. Kurn, and W. Ketterle, “Observation of interference between two Bose condensates,” *Science* **275**, 637–641 (1997).
- [23] J. R. Abo-Shaeer and C. Raman and J. M. Vogels and W. Ketterle, “Observation of Vortex Lattices in Bose-Einstein Condensates,” *Science* **292**, 476–479 (2001).
- [24] B. P. Anderson and M. A. Kasevich, “Macroscopic Quantum interference from Atomic Tunnel Arrays,” *Science* **282**, 1686 (1998).

- 
- [25] F. S. Cataliotti, S. Burger, C. Fort, P. Maddaloni, F. Minardi, A. Trombettoni, A. Smerzi, and M. Inguscio, “Josephson Junction Arrays with Bose-Einstein Condensates,” *Science* **293**, 843–846 (2001).
- [26] M. Greiner, O. Mandel, T. Esslinger, T. W. Hänsch, and I. Bloch, “Quantum phase transition from a superfluid to a Mott insulator in a gas of ultracold atoms,” *Nature* **415**, 39–44 (2002).
- [27] G.-B. Jo and Y. Lee and J. Choi and C. A. Christensen and T. H. Kim and J. H. Thywissen and D. E. Pritchard and W. Ketterle, “Itinerant Ferromagnetism in a Fermi Gas of Ultracold Atoms,” *Science* **325**, 1521–1524 (2009).
- [28] C. Orzel, A. K. Tuchman, M. L. Fenselau, M. Yasuda, and M. A. Kasevich, “Squeezed States in a Bose-Einstein Condensate,” *Science* **291**, 2386–2389 (2001).
- [29] J. Estève, A. Weller, S. Giovannazzi, and M. K. Oberthaler, “Squeezing and entanglement in a Bose-Einstein condensate,” *Nature* **455**, 1216–1219 (2008).
- [30] Y. Shin, C. Sanner, G. B. Jo, T. A. Pasquini, M. Saba, W. Ketterle, D. E. Pritchard, M. Vengalattore, and M. Prentiss, “Interference of Bose-Einstein condensates split with an atom chip,” *Phys. Rev. A* **72**, 021604 (2005).
- [31] Y. Wang, D. Z. Anderson, V. M. Bright, E. A. Cornell, Q. Diot, T. Kishimoto, M. Prentiss, R. A. Saravanan, S. R. Segal, and S. Wu, “Atom Michelson interferometer on a chip using a Bose-Einstein Condensate,” *Phys. Rev. Lett.* **94**, 090405 (2005).
- [32] M. Horikoshi and K. Nakagawa, “Dephasing due to atom-atom interaction in a waveguide interferometer using a Bose-Einstein condensate,” *Phys. Rev. A* **74**, 031602–1 (2006).

- 
- [33] J. I. Cirac and P. Maraner and J. K. Pachos , “Cold Atom Simulation of Interacting Relativistic Quantum Field Theories,” *Phys. Rev. Lett.* **105**, 190403 (2010).
- [34] J. Simon and W. S. Bakr and R. Ma and M. E. Tai and P. M. Preiss and M. Greiner , “Quantum simulation of antiferromagnetic spin chains in an optical lattice,” *Nature* **472**, 307–312 (2011).
- [35] J. J. García-Ripoll and J. I. Cirac, “Quantum computation with cold bosonic atoms in an optical lattice,” *Phil. Trans. R. Soc. Lond. A* **361**, 1537–1548 (2003).
- [36] I. Bloch, “Ultracold quantum gases in optical lattices,” *Nature Physics* **1**, 23–30 (2002).
- [37] I. Bloch and M. Köhl and M. Greiner and T. W. Hänsch and T. Esslinger , “Optics with an Atom Laser Beam,” *Phys. Rev. Lett.* **87**, 030401 (2001).
- [38] T. Young, “An account of some cases of the production of colours, not hitherto described,” *Phil. Trans. Roy. Soc.* **92**, 387–392 (1802).
- [39] L. de Broglie, *Ann. Phys.* **3**, 387–392 (1925).
- [40] O. Carnal and J. Mlynek, “Young’s double-slit experiment with atoms: A simple atom interferometer,” *Phys. Rev. Lett.* **66**, 2689–2692 (1991).
- [41] M. Kasevich and S. Chu, “Atomic Interferometry using stimulated Raman transitions,” *Phys. Rev. Lett.* **67**, 181 (1991).
- [42] M. Kasevich and S. Chu, “Measurement of the gravitational acceleration of an atom with a light-pulse atom interferometer,” *Appl. Phys. B* **54**, 321 (1992).

- [43] K. Moler, D. S. Weiss, M. Kasevich, and S. Chu, “Theoretical analysis of velocity-selective Raman transitions,” *Phys. Rev. A* **45**, 342 (1992).
- [44] E. M. Rasel, M. K. Oberthaler, H. Batelaan, J. Schmiedmayer, and A. Zeilinger, “Atom Wave Interferometry with Diffraction Gratings of Light,” *Phys. Rev. Lett.* **75**, 2633 (1995).
- [45] M. K. Oberthaler, S. Bernet, E. M. Rasel, J. Schmiedmayer, and A. Zeilinger, “Inertial sensing with classical atomic beams,” *Phys. Rev. A* **54**, 3165–3176 (1996).
- [46] D. M. Giltner, R. W. McGowan, and S. A. Lee, “Atom interferometer based on Bragg scattering from Standing Light Waves,” *Phys. Rev. Lett.* **75**, 2638 (1995).
- [47] J. B. Fixler, G. T. Foster, J. M. McGuirk, and M. A. Kasevich, “Atom Interferometer Measurement of the Newtonian Constant of Gravity,” *Science* **315**, 74 (2007).
- [48] C. R. Ekstrom, J. Schmiedmayer, M. S. Chapman, T. D. Hammond, and D. E. Pritchard, “Measurement of electric polarizability of sodium with an atom interferometer,” *Phys. Rev. A* **51**, 3883 (1995).
- [49] A. Wicht, J. M. Hensley, E. Sarajlic, and S. Chu, “A Preliminary Measurement of the Fine Structure Constant Based on Atom Interferometry,” *Phys. Scr.* **T102**, 82 (2002).
- [50] A. Peters, K. Y. Chung, and S. Chu, “Measurement of gravitational acceleration by dropping atoms,” *Nature* **5400**, 849 – 852 (1999).



- 
- [51] T. Schumm, S. Hofferberth, L. M. Andersson, S. Wildermuth, S. Groth, I. Bar-Joseph, J. Schmiedmayer, and P. Krüger, “Matter-wave interferometry in a double well on an atom chip,” *Nature* **1**, 57–62 (2005).
- [52] G. B. Jo, Y. Shin, S. Will, T. A. Pasquini, M. Saba, W. Ketterle, D. E. Pritchard, M. Vengalattore, and M. Prentiss, “Long Phase Coherence Time and Number Squeezing of Two Bose-Einstein condensates on an Atom Chip,” *Phys. Rev. Lett.* **98**, 030407 (2007).
- [53] O. Garcia, B. Deissler, K. J. Hughes, J. M. Reeves, and C. A. Sackett, “Bose-Einstein condensate interferometer with macroscopic arm separation,” *Phys. Rev. A* **74**, 031601(R) (2006).
- [54] J. A. Stickney and A. A. Zozulya, “Wave-function recombination instability in cold-atom interferometers,” *Phys. Rev. A* **66**, 053601 (2002).
- [55] Y. Shin, M. Saba, T. A. Pasquini, W. Ketterle, D. E. Pritchard, and A. E. Leanhardt, “Atom Interferometry with Bose-Einstein Condensates in a Double-Well Potential,” *Phys. Rev. Lett.* **92**, 050405 (2004).
- [56] J. Javanainen and M. Wilkens, “Phase and Phase diffusion of a split Bose-Einstein condensate,” *Phys. Rev. Lett.* **78**, 4675 (1997).
- [57] E. M. Wright, T. Wong, M. J. Collett, S. M. Tan, and D. F. Walls, “Collapses and revivals in the interference between two Bose-Einstein condensates formed in small atomic samples,” *Phys. Rev. A* **56**, 591 (1997).
- [58] J. Stickney and A. Zozulya, “Influence of nonadiabaticity and nonlinearity on the operation of cold-atom beam splitters,” *Phys. Rev. A* **68**, 013611 (2003).

- [59] J. H. T. Burke, B. Deissler, K. J. Hughes, and C. A. Sackett, “Confinement effects in a guided-wave atom interferometer with millimeter-scale arm separation,” *Phys. Rev. A* **78**, 023619 (2008).
- [60] M. Horikoshi and K. Nakagawa, “Suppression of dephasing due to trapping potential and atom-atom interactions in a trapped-condensate interferometer,” *Phys. Rev. Lett.* **99**, 18040–1 (2007).
- [61] S. R. Segal, Q. Diot, E. A. Cornell, A. A. Zozulya, and D. Z. Anderson, “Revealing buried information: Statistical processing techniques for ultracold-gas image analysis,” *Phys. Rev. A* **81**, 053601 (2010).
- [62] M. Olshanii and V. Dunjko, “Interferometry in dense nonlinear media and interaction-induced loss of contrast in microfabricated interferometers,” *arXiv:cond-mat/ 0505358v2* (2005).
- [63] J. A. Stickney, D. Z. Anderson, and A. A. Zozulya, “Increasing the coherence time of Bose-Einstein condensate interferometers with optical control of dynamics,” *Phys. Rev. A* **75**, 063603 (2007).
- [64] J. A. Stickney, R. P. Kaffle, D. Z. Anderson, and A. A. Zozulya, “Theoretical analysis of a single- and double-reflection atom interferometer in a weakly confining magnetic trap,” *Phys. Rev. A* **77**, 043604 (2008).
- [65] P. J. Martin and B. G. Oldaker and A. H. Miklich and D. E. Pritchard , “Bragg scattering of atoms from a standing light wave,” *Phys. Rev. Lett.* **60**, 515–518 (1988).
- [66] M. Kozuma and L. Deng and E. W. Hagley and J. Wen and R. Lutwak and K. Helmerson and S. L. Rolston and W. D. Phillips, “Coherent Splitting of Bose-

- Einstein Condensed Atoms with Optically Induced Bragg Diffraction,” *Phys. Rev. Lett.* **82**, 871–875 (1999).
- [67] B. Young, M. Kasevich, and S. Chu, “Precision atom interferometry with light pulses,” in *Atom interferometry*, P. R. Berman, ed., (Academic Press, New York, 1997), pp. 363 – 334.
- [68] C. Cohen-Tannoudji, B. Diu, and F. Laloë, *Quantum Mechanics* (John Wiley, Singapore, 2005), Vol. 1.
- [69] C. J. Foot, *Atomic Physics* (Oxford University Press, New York, 2005).
- [70] W. J. Mullin , “Bose-Einstein condensation in a harmonic potential,” *J. Low Temp. Phys.* **106**, 615–641 (1997).
- [71] F. Dalfovo, S. Giorgini, L. P. Pitaevskii, and S. Stringari, “Theory of Bose-Einstein condensation in trapped gases,” *Rev. Mod. Phys.* **71**, 463 (1999).
- [72] M. Abramowitz and I. A. Stegun, *Handbook of Mathematical Functions* (Dover, New York, 1972).
- [73] C. J. Pethick and H. Smith, *Bose-Einstein condensation in dilute gases* (Cambridge University Press, Cambridge, 2002).
- [74] L. Pitaevskii and S. Stringari, *Bose-Einstein condensation* (Oxford University Press, Oxford, 2003).
- [75] G. Baym and C. J. Pethick, “Ground-State Properties of Magnetically Trapped Bose-Condensed Rubidium Gas,” *Phys. Rev. Lett.* **76**, 6 (1996).
- [76] E. M. Wright and D. F. Walls, “Collapses and revivals of Bose-Einstein condensates formed in small atomic samples,” *Phys. Rev. Lett.* **77**, 2158 (1996).

- 
- [77] W. Li, A. K. Tuchman, H. Chien, and M. A. Kasevich, “Extended Coherence Time with Atom-Number Squeezed States,” *Phys. Rev. Lett.* **98**, 040402 (2007).
- [78] L. Pezzé, L. A. Collins, A. Smerzi, G. P. Berman, and A. R. Bishop, “Sub-shot-noise phase sensitivity with a Bose-Einstein condensate Mach-Zehnder interferometer,” *Phys. Rev. A* **72**, 043612 (2005).
- [79] J. A. Dunningham and K. Burnett, “Sub-shot-noise-limited measurements with Bose-Einstein condensates,” *Phys. Rev. A* **70**, 033601 (2004).
- [80] M. F. Riedel, P. Böhi, Y. Li, T. W. Hänsch, A. Sinatra, and P. Treutlein, “Atom-chip-based generation of entanglement for quantum metrology,” *Nature* **464**, 1170–1173 (2010).
- [81] C. Gross, T. Zibold, E. Nicklas, J. Estève, and M. K. Oberthaler, “Nonlinear atom interferometer surpasses classical precision limit,” *Nature* **464**, 1165–1169 (2010).
- [82] E. O. Ilo-Okeke and A. A. Zozulya, “Atomic population distribution in the output ports of cold-atom interferometers with optical splitting and recombination,” *Phys. Rev. A* **82**, 053603 (2010).
- [83] P. D. D. Schwindt, E. A. Cornell, T. Kishimoto, Y. Wang, and D. Z. Anderson, “Efficient loading of a magnetic waveguide on an atom chip,” *Phys. Rev. A* **72**, 023612 (2005).
- [84] P. S. Julienne, F. H. Mies, E. Tiesinga, and C. J. Williams, “Collisional Stability of Double Bose Condensates,” *Phys. Rev. Lett.* **78**, 1880 (1997).
- [85] R. P. Kafle, D. Z. Anderson, and A. A. Zozulya, “Analysis of a free oscillation atom interferometer,” *Phys. Rev. A* **84**, 033639 (2011).

# Appendix A

## Published Work

# Atomic population distribution in the output ports of cold-atom interferometers with optical splitting and recombination

Ebubechukwu O. Ilo-Okeke and Alex A. Zozulya\*

*Department of Physics, Worcester Polytechnic Institute, 100 Institute Road, Worcester, Massachusetts 01609, USA*

(Received 17 June 2010; published 3 November 2010)

Cold-atom interferometers with optical splitting and recombination use off-resonant laser beams to split a cloud of Bose-Einstein condensate (BEC) into two clouds that travel along different paths and are then recombined again using optical beams. After the recombination, the BEC in general populates both the cloud at rest and the moving clouds. Measuring a relative number of atoms in each of these clouds yields information about the relative phase shift accumulated by the atoms in the two moving clouds during the interferometric cycle. We derive the expression for the probability of finding any given number of atoms in each of the clouds, discuss features of the probability density distribution, analyze its dependence on the relative accumulated phase shift as a function of the strength of the interatomic interactions, and compare our results with experiment.

DOI: [10.1103/PhysRevA.82.053603](https://doi.org/10.1103/PhysRevA.82.053603)

PACS number(s): 03.75.Dg, 37.25.+k, 03.75.Kk

## I. INTRODUCTION

Using wavelike properties of atoms for atomic interferometry has been a subject of intense and extensive study [1]. Atoms are sensitive to electromagnetic fields due to their electric and magnetic moments; their mass allows them to be deflected in the gravitational field thereby making them attractive in the measurements of inertial forces [2]. Atom interferometers have been used to measure the gravitational constant [3], acceleration [4–6], electric polarizability [7], and fine-structure constant [8] to very high accuracy.

The technical realization of neutral-atom interferometers took some time compared to their electron- and neutron-based counterparts. Part of the reason is that atoms have large mass, resulting in smaller de Broglie wavelengths for the same velocity. Also, neutral atoms cannot easily propagate in dense matter unlike, e.g., neutrons, and therefore they require more ingenious ways to coherently split and diffract the atomic beam. An atom interferometer [9] realized in a double-slit diffraction geometry worked with a stream of supersonic gaseous atoms and used mechanical gratings. Later experiments [10,11] used standing light waves to coherently diffract the atomic beam. The standing light wave is formed using a laser beam that is detuned from atomic resonance to avoid spontaneous emission, and is retroreflected by a mirror. The spatially varying envelope of the standing wave creates an effective optical potential acting as a diffraction grating for atoms that can be used to split and recombine an atomic beam.

Another technique [4,12] for diffracting an atomic beam exploits Raman transitions between two hyperfine ground states of an atom via a third quasiexcited state. The laser pulses (often called Raman pulses) consist of two counterpropagating light beams with frequencies which are different by the Bohr transition frequency between the two hyperfine states. Absorption of a photon from one laser beam and stimulated

reemission into another one in this case is accompanied by a transition between the two hyperfine states.

The use of Bose-Einstein condensates (BECs) [13] in atom interferometers is appealing for many reasons. A BEC has a narrow momentum distribution that minimizes the spread in momentum during the splitting and recombination of the atomic cloud and reduces the expansion of the condensate during propagation. BECs can be easily manipulated and confined in a very small area on an atom chip [14]. Finally, a BEC has large coherence length allowing for good fringe contrast and helping to determine any offset phases more accurately. Since the experimental demonstration of interference between two different Bose condensates [15], several experimental techniques for the manipulation of BECs and different BEC-based interferometric geometries have been proposed and demonstrated [14,16–19].

In trapped-atom interferometer geometries [16,17,20–22] the BEC is kept in a trap confining the atomic cloud in all three dimensions. This trap is dynamically transformed into a double-well trap to create two arms which were physically separated in space. After some time, the trap is switched off allowing the condensates in each arm to fall, expand, and interfere. An example of this type of interferometer is a double-well atom Mach-Zehnder interferometer that has been attracting recent theoretical ([23,24]) and experimental ([20–22]) attention in relation to a generation of squeezed states and sub-shot-noise measurements. In some of the experiments, the external motional states are used to produce interference fringes by controlling the Josephson tunneling between wells through trap deformation [20,23,24] by manipulating the barrier in the middle of the well. During the splitting the barrier is raised slowly so that the condensates follow the ground state of the well adiabatically. The fluctuation in the relative number of atoms is reduced when the tunneling energy between the wells is smaller than the interaction energy. Counting the population of atoms in each well site gives information on the squeezed states. Another method [21,22] uses the internal (spin) states of BECs trapped in a deep potential well to form the arms of the interferometer. A BEC cloud initially in a hyperfine state  $|a\rangle$  is put in superposition of two hyperfine states  $|a\rangle$  and  $|b\rangle$  using the  $\pi/2$  pulse. Feshbach resonance [21]

\*zozulya@wpi.edu

or a state-dependent potential [22] is used to tune down the interspecies scattering, thereby leading to increased intraspecies interactions that cause oscillation of the condensates. The two clouds are recombined at the end of the interferometric cycle using a  $\pi/2$  pulse with a controlled phase or a state-dependent potential [22]. Information on squeezing is obtained by counting the population of atoms in each hyperfine state.

In guided-wave interferometers the BEC is kept in a waveguide. The condensate is tightly confined in two transverse dimensions but allowed to propagate along the third dimension [14,25]. The waveguide potential along this guiding dimension is typically weakly parabolic either because of the difficulty of completely canceling magnetic-field gradients or by design. A typical example is the Michelson-type single reflection atom interferometer realized in Ref. [14]. In this interferometer, the BEC cloud  $\psi_0$  is initially at rest in a waveguide. Splitting pulses that consist of a pair of counterpropagating laser beams detuned from atomic resonance and that act as a diffraction grating are incident on the cloud. These pulses split the condensate into two harmonics,  $\psi_+$  and  $\psi_-$ , that move with the initial velocities  $\pm v_0$ , respectively. In a single-reflection interferometer, the directions of propagation of these harmonics are reversed at time  $T/2$  (where  $T$  is the duration of the interferometric cycle) (i.e., in the middle of the cycle with the help of a reflection pulse). The harmonics are then allowed to propagate back and are recombined when they overlap again using the same optical pulses that were used to split the original BEC cloud. After recombination, the condensate is, in general, in a superposition of  $\psi_0$ ,  $\psi_+$ , and  $\psi_-$  with the relative amplitudes, depending on the amount of the accumulated phase shift, between the arms of the interferometer acquired during the cycle.

In a double-reflection interferometer [25,26], the optical reflection pulse is applied twice at times  $T/4$  and  $3T/4$ . After the first reflection pulse, the harmonics change their direction of propagation and start moving back. They pass through each other, and exchange their positions by the time  $3T/4$ . The harmonic that was on the right at  $T/2$  is now on the left and vice versa. The second reflection pulse applied at  $3T/4$  again reverses the directions of propagation of the harmonics and, finally, they are recombined at time  $T$ .

The authors of Refs. [26–28] investigated interferometric geometry that does not rely on reflecting optical pulses but instead uses the gradient of the confining waveguide potential for reversing the direction of propagation of the BEC harmonics. In this “free-oscillation” interferometer the moving BEC clouds propagate in a parabolic confining potential. They slow down as they climb the potential, stop at their classical turning points after one-quarter of the trap period ( $T/4$ ) has elapsed, and turn back. At  $T/2$  the clouds meet at the bottom of the potential, reach again their turning points at  $3T/4$ , and are recombined at time  $T$ . The duration of the interferometric cycle is thus equal to the oscillation period of the parabolic longitudinal waveguide potential  $T$ .

Another waveguide interferometer that uses BEC is the Mach-Zehnder-type atom interferometer [18,27]. Here the two counterpropagating waves used for a  $\pi/2$  splitting pulse are frequency-shifted with respect to each other

resulting in a traveling optical potential. This  $\pi/2$  pulse transforms the original BEC at rest into two clouds of equal amplitude. One of these clouds remains at rest and the other propagates with velocity  $v_0$ . A  $\pi$  pulse in the middle of the cycle stops the moving cloud and brings the one that was at rest into motion. Finally, the second  $\pi/2$  pulse applied at the end of the cycle recombines the two clouds.

Both in trapped-atom and guided-wave interferometers, the interference fringes depend on the relative phase accumulated by the atomic clouds in different arms during the interferometric cycle. Apart from the accumulated phase shift induced by fields or interactions of interest during the experiment, an unwanted phase may be accumulated due to confinement effects and interatomic interactions resulting in a decrease in the visibility of the interference fringes. For example, in the single-pass interferometer [14], during propagation the outer edge of each cloud experiences a higher potential than the inner edge (the outer edge is the leading edge in the first half of the cycle when the clouds move away from each other and the trailing edge in the second part when the clouds move toward each other). The outer edge thus accumulates a larger phase than the inner one. During the recombination, the outer edge of one cloud interferes with the inner edge of another and the phase difference accumulated due to the presence of the confinement potential leads to a coordinate-dependent residual phase across the clouds after the recombination. Another mechanism for phase accumulation is due to mutual interaction of two BEC clouds  $\psi_-$  and  $\psi_+$  when they spatially overlap. During the separation, the inner edge of one cloud interacts with atoms in the other cloud until it has traversed the entire length of the other cloud, while the outer edge of each cloud hardly interacts with any atoms in the other cloud (and similarly during the recombination). As a result, the inner edge accumulates a larger phase than the outer edge. The above two contributions have opposite signs but different magnitudes so the net coordinate-dependent phase is not zero. Still another mechanism of accumulation of the unwanted phase is due to the fact that the velocities  $\pm v$  of the moving harmonics  $\psi_+$  and  $\psi_-$  during the reflection are different from their initial velocities  $\pm v_0$  due to the influence of the confining potential and the interatomic interactions. As a result, the reflection pulses (which are formed by the same pair of counterpropagating beams as the splitting and recombination pulses) are not exactly on resonance and do not exactly reverse the clouds’ velocities (the direction of propagation of each of the clouds does change but the speeds before and the after the reflections are different).

A theoretical analysis of the single- and double-reflection interferometer geometries has been carried out in Refs. [26, 29–31]. According to the analysis of Refs. [26,31], symmetric motion of the two clouds in the double-reflection geometry partially cancels the velocity errors imposed by the reflection pulses and the phase imposed by the confining potential. This conclusion has been confirmed experimentally in Ref. [26]. The free-oscillation interferometer provides an even greater degree of cancellation of the unwanted coordinate-dependent phase since it does not rely on reflection pulses and does not suffer from the velocity mismatch effects. Recent experiments [26,27], where the atomic clouds were

allowed to be reflected from their classical turning points instead of using reflection pulses to truncate their motion, confirmed a more accurate cancellation of the unwanted phase.

An additional mechanism that could lead to dephasing of the interference fringes is due to atom-atom interactions within each of the two clouds. These interactions result in the so-called phase diffusion in the BEC clouds [32–36]. The aim of the present paper is to analyze effects of the atom-atom interactions within each of the BEC clouds on the operation of cold-atom interferometers using optical pulses for splitting and recombination of the condensate in the framework of the approach discussed in Refs. [32–36]. The basic physics of the interferometric cycle in the presence of the interatomic interactions can be described as follows: The BEC, which is initially in a number state with  $N$  atoms, is split by the optical pulses into two clouds moving in opposite directions. After the splitting the system is in a mode-entangled state with each cloud being a linear superposition of number states. This superposition is concentrated around the mean  $N/2$  with the relative uncertainty of the order of  $1/\sqrt{N}$ . In the presence of interatomic interactions, each number state evolves with different rate that results in the accumulation of relative time-dependent phases between the different number states. The recombination process is sensitive to these phases and thus the interactions should influence the contrast of the interferometric fringes. Specifically, we derive the expression for the probability density of observing any given number of atoms in each of the three output ports of the optical beamsplitter and recombiner and analyze it in different limits. Due to a large difference between the characteristic momenta of the condensate and the momentum imparted to the atoms by the optical beams, it turns out to be possible to analyze both the splitting and the recombination (detection) of the BEC explicitly without making any *ad hoc* assumptions about the process of detection (e.g., invoking phase states to describe the detection process).

Finally we note that the approach of the present paper is complementary to that of Refs. [26,29–31] which previously discussed the single- and double-reflection interferometer geometries. The analysis of these papers is carried out in the framework of the mean-field theory and thus cannot account for the mode-entangled nature of the two BEC clouds after the splitting, the subject discussed in the present paper. Degradation of the interference fringes in Refs. [26,29–31] is due to the accumulation of a coordinate-dependent phase across the BEC clouds during their evolution due to confinement and mutual interaction. Our analysis disregards these effects for simplicity since they have been previously studied. The more general analysis will be reported in a later publication.

The remainder of the paper is organized as follows. In Sec. II we discuss the operation of the optical beamsplitter and recombiner and obtain the expression for the state vector of the system after recombination. In Sec. III we derive an expression for the probability density. Characteristic features of the probability density, including the mean, the standard deviation, etc., are calculated and discussed in Sec. V. The results are compared with the experiment in Sec. VI.

## II. OPTICAL BEAMSPLITTER OPERATION

Consider a BEC cloud  $\psi_0$  at rest in a confining potential before the beginning of the interferometric cycle. As was discussed in the Introduction, the splitting optical pulses transform the initial BEC cloud into two clouds  $\psi_{\pm 1}$  moving in opposite directions. The clouds are allowed to evolve during time  $T$  and are subject to the action of the recombination optical pulses (which are identical to splitting optical pulses). After the recombination, the atoms in general populate all three clouds  $\psi_0$  and  $\psi_{\pm}$ . The relative population of the clouds depends on the phase difference between the clouds  $\psi_{\pm}$  acquired during the interferometric cycle.

Let  $b_0^\dagger$ ,  $b_{-1}^\dagger$ , and  $b_{+1}^\dagger$  be operators which, acting on a vacuum state, create an atom belonging to a cloud at rest and moving to the left or right, respectively.

The many-body Hamiltonian that describes the atomic BEC during the interferometric cycle is of the form

$$H = \int d\mathbf{r} \hat{\Psi}^\dagger(\mathbf{r}, t) H_0 \hat{\Psi}(\mathbf{r}, t) + \frac{U_0}{2} \int d\mathbf{r} \hat{\Psi}^\dagger(\mathbf{r}, t) \hat{\Psi}^\dagger(\mathbf{r}, t) \hat{\Psi}(\mathbf{r}, t) \hat{\Psi}(\mathbf{r}, t), \quad (1)$$

where  $H_0$  is a single-particle Hamiltonian and  $U_0 = 4\pi\hbar^2 a_{sc}/M$ , with  $M$  being the atomic mass and  $a_{sc}$  the  $s$ -wave scattering length. The single-particle Hamiltonian  $H_0$  accounts for the confining potential for the BEC and also includes effects of the environment resulting in different rates of evolution for the BEC clouds propagating in opposite directions. Finally, the quantity  $\hat{\Psi}(\mathbf{r}, t)$  is the field operator

$$\hat{\Psi}(\mathbf{r}, t) = b_{+1} \psi_{+1}(\mathbf{r}, t) + b_{-1} \psi_{-1}(\mathbf{r}, t), \quad (2)$$

where  $\psi_{\pm 1}(\mathbf{r}, t)$  are wave functions of the BEC clouds moving to the right and left, respectively. These wave functions are solutions of the two coupled Gross-Pitaevskii equations [see, e.g., Eq. (9) of Ref. [30]] and are normalized to one,  $\int d\mathbf{r} |\psi_{\pm 1}(\mathbf{r}, t)|^2 = 1$ .

Using Eq. (2) in (1) results in the following Hamiltonian describing effects of the environment and the interatomic interactions:

$$H_{\text{eff}} = -\frac{W}{2} (\hat{n}_{+1} - \hat{n}_{-1}) + g(\hat{n}_{+1}^2 + \hat{n}_{-1}^2). \quad (3)$$

Here  $\hat{n}_{\pm 1} = b_{\pm 1}^\dagger b_{\pm 1}$  are the number operators,  $W$  is the relative environment-introduced energy shift between the right- and left-propagating clouds, and

$$g = \frac{U_0}{2} \int d\mathbf{r} |\psi_{+1}|^4 = \frac{U_0}{2} \int d\mathbf{r} |\psi_{-1}|^4 \quad (4)$$

is the coefficient characterizing strength of the interatomic interaction. The Hamiltonian (3) neglects effects due to overlap of the right- and left-propagating clouds assuming that most of the time the clouds are spatially separated.

The state vector of the system at the beginning of the interferometric cycle before the splitting pulses is given by the relation

$$|\Psi_{\text{ini}}\rangle = \frac{(b_0^\dagger)^N}{\sqrt{N!}} |0\rangle, \quad (5)$$



where  $|0\rangle$  is the vacuum state and  $N$  is the total number of atoms in the BEC.

Splitting and recombination pulses couple the operators  $b_{\pm 1}$  and  $b_0$  according to the rules (see the Appendix in Ref. [30] for the corresponding splitting and recombination matrices),

$$\begin{aligned} b_{-1} &\rightarrow \frac{1}{2}b_{+1} + \frac{e^{-i\beta}}{\sqrt{2}}b_0 - \frac{1}{2}b_{-1}, \\ b_0 &\rightarrow (b_{+1} + b_{-1}) \frac{e^{-i\beta}}{\sqrt{2}}, \\ b_{+1} &\rightarrow -\frac{1}{2}b_{+1} + \frac{e^{-i\beta}}{\sqrt{2}}b_0 + \frac{1}{2}b_{-1}, \end{aligned} \quad (6)$$

where  $\beta$  is a phase factor.

A single-atom state is transformed by the splitting pulses as

$$b_0^\dagger|0\rangle \rightarrow \frac{1}{\sqrt{2}}(b_{+1}^\dagger + b_{-1}^\dagger)|0\rangle,$$

so the product state vector of the  $N$ -particle system, Eq. (5), after the splitting acquires the form

$$\begin{aligned} |\Psi_{\text{split}}\rangle &= \frac{1}{\sqrt{2^N N!}}(b_{+1}^\dagger + b_{-1}^\dagger)^N |0\rangle \\ &= \frac{1}{\sqrt{2^N}} \sum_{n=0}^N \binom{N}{n}^{1/2} |n, N-n\rangle, \end{aligned} \quad (7)$$

where

$$|n_+, n_-\rangle = \frac{(b_{+1}^\dagger)^{n_+} (b_{-1}^\dagger)^{n_-}}{\sqrt{n_+!} \sqrt{n_-!}} |0\rangle \quad (8)$$

is the state with  $n_+$  atoms traveling to the right and  $n_-$  to the left, respectively, and  $\binom{N}{n} = N!/n!(N-n)!$  is the binomial coefficient.

Time evolution of the state vector is governed by the Hamiltonian (3),

$$|\Psi(t)\rangle = |\Psi_{\text{split}}\rangle \exp\left[-(i/\hbar) \int_0^t H_{\text{eff}} dt'\right].$$

States  $|n_+, n_-\rangle$  given by Eq. (8) are eigenstates of the Hamiltonian (3) with the eigenvalues

$$E(n_+, n_-) = -\frac{W}{2}(n_+ - n_-) + g(n_+^2 + n_-^2). \quad (9)$$

The state vector of the system at time  $T$  immediately before the recombination is thus given by the relation

$$\begin{aligned} |\Psi(T)\rangle &= \frac{1}{\sqrt{2^N N!}} \sum_{n=0}^N \binom{N}{n} e^{i\theta(n-N/2) - i\xi[n^2 + (N-n)^2]} \\ &\quad \times (b_{+1}^\dagger)^n (b_{-1}^\dagger)^{N-n} |0\rangle. \end{aligned} \quad (10)$$

Here

$$\theta = \frac{1}{\hbar} \int_0^T dt W \quad (11)$$

is the environment-introduced accumulated phase difference between the right and the left clouds and

$$\xi = \frac{1}{\hbar} \int_0^T dt g \quad (12)$$

is the accumulated nonlinear phase per atom due to interatomic interactions. The recombination pulses act on  $|\Psi(T)\rangle$  in accordance with Eq. (6). The resulting state vector of the system after the recombination has the form

$$\begin{aligned} |\Psi_{\text{rec}}\rangle &= \frac{1}{\sqrt{2^N N!}} \sum_{n=0}^N \binom{N}{n} e^{i\theta(n-N/2) - 2i\xi(n-N/2)^2} \\ &\quad \times \left(-\frac{1}{2}b_{+1}^\dagger + \frac{e^{i\beta}}{\sqrt{2}}b_0^\dagger + \frac{1}{2}b_{-1}^\dagger\right)^n \\ &\quad \times \left(\frac{1}{2}b_{+1}^\dagger + \frac{e^{i\beta}}{\sqrt{2}}b_0^\dagger - \frac{1}{2}b_{-1}^\dagger\right)^{N-n} |0\rangle, \end{aligned} \quad (13)$$

where we have omitted the irrelevant phase term  $\exp(-i\xi N^2/2)$ .

### III. PROBABILITY DENSITY

The state that has  $n_+$  atoms in the cloud moving to the right,  $n_-$  in the cloud moving to left, and  $n_0 = N - n_+ - n_-$  in the cloud at rest, is described by the state vector

$$|n_+, n_-, n_0\rangle = \frac{(b_{+1}^\dagger)^{n_+} (b_{-1}^\dagger)^{n_-} (b_0^\dagger)^{n_0}}{\sqrt{n_+!} \sqrt{n_-!} \sqrt{n_0!}} |0\rangle. \quad (14)$$

The probability of this outcome after the recombination is given by the modulus squared of the probability amplitude  $\langle n_+, n_-, n_0 | \Psi_{\text{rec}} \rangle$ . Using Eq. (13), this probability amplitude can be written as

$$\begin{aligned} \langle n_+, n_-, n_0 | \Psi_{\text{rec}} \rangle &= \frac{1}{\sqrt{2^N N!}} \sum_{n=0}^N \binom{N}{n} e^{i\theta(n-N/2) - 2i\xi(n-N/2)^2} \\ &\quad \times \langle 0 | \frac{(b_0^\dagger)^{n_0}}{\sqrt{n_0!}} \frac{(b_{-1}^\dagger)^{n_-}}{\sqrt{n_-!}} \frac{(b_{+1}^\dagger)^{n_+}}{\sqrt{n_+!}} \left(-\frac{b_{+1}^\dagger - b_{-1}^\dagger}{2} + \frac{e^{i\beta}}{\sqrt{2}}b_0^\dagger\right)^n \\ &\quad \times \left(\frac{b_{+1}^\dagger - b_{-1}^\dagger}{2} + \frac{e^{i\beta}}{\sqrt{2}}b_0^\dagger\right)^{N-n} |0\rangle. \end{aligned} \quad (15)$$

Equation (15) can be recast as

$$\begin{aligned} \langle n_+, n_-, n_0 | \Psi_{\text{rec}} \rangle &= \frac{1}{\sqrt{2^N N!}} \sum_{n=0}^N \binom{N}{n} e^{i\theta(n-N/2) - 2i\xi(n-N/2)^2} \\ &\quad \times \frac{1}{\sqrt{n_+! n_-! n_0!}} \langle 0 | \frac{\partial^{n_0}}{\partial (b_0^\dagger)^{n_0}} \frac{\partial^{n_-}}{\partial (b_{-1}^\dagger)^{n_-}} \frac{\partial^{n_+}}{\partial (b_{+1}^\dagger)^{n_+}} \\ &\quad \times \left(-\frac{b_{+1}^\dagger - b_{-1}^\dagger}{2} + \frac{e^{i\beta}}{\sqrt{2}}b_0^\dagger\right)^n \\ &\quad \times \left(\frac{b_{+1}^\dagger - b_{-1}^\dagger}{2} + \frac{e^{i\beta}}{\sqrt{2}}b_0^\dagger\right)^{N-n} |0\rangle. \end{aligned} \quad (16)$$

The product of the two terms in parentheses can be represented as the double sum

$$\begin{aligned} & \left( -\frac{b_{+1}^\dagger - b_{-1}^\dagger}{2} + \frac{e^{i\beta}}{\sqrt{2}} b_0^\dagger \right)^n \left( \frac{b_{+1}^\dagger - b_{-1}^\dagger}{2} + \frac{e^{i\beta}}{\sqrt{2}} b_0^\dagger \right)^{N-n} \\ &= \sum_{i=0}^n \sum_{j=0}^{N-n} \binom{n}{i} \binom{N-n}{j} \left( \frac{e^{i\beta} b_0^\dagger}{\sqrt{2}} \right)^{i+j} (-1)^{n-i} \\ & \quad \times \left( \frac{b_{+1}^\dagger - b_{-1}^\dagger}{2} \right)^{N-i-j}. \end{aligned} \quad (17)$$

The derivatives with respect to  $b_0$  in Eq. (16) will select only the term with  $i + j = n_0$  from this sum, yielding

$$\langle n_+, n_-, n_0 | \Psi_{\text{rec}} \rangle = e^{i\alpha} \sqrt{\frac{N! 2^{n_0-N}}{n_0! n_+! n_-!}} \sum_{n=0}^N e^{i\theta(n-N/2)-2i\xi(n-N/2)^2} I(n, n_0), \quad (18)$$

where

$$\begin{aligned} I(n, n_0) &= i^{N-n_0} \frac{\binom{N}{n_0} \binom{N}{n}^{-1}}{2^N} \sum_{i=0}^n \sum_{j=0}^{N-n} \delta_{i+j, n_0} \binom{n}{j} \\ & \quad \times \binom{N-n}{j} (-1)^{n-i} \end{aligned} \quad (19)$$

and

$$\alpha = \beta n_0 + (\pi/2)(n_- - n_+). \quad (20)$$

The unwieldy expression (19) can be written in a much more manageable form by evaluating Eq. (16) for  $\xi = 0$ . In this case, summation in Eq. (16) can be readily carried out and, after differentiation, Eq. (16) results in the expression

$$\begin{aligned} & \langle n_+, n_-, n_0 | \Psi_{\text{rec}} \rangle_{\xi=0} \\ &= e^{i\alpha} \sqrt{\frac{N! 2^{(n_0-N)}}{n_0! n_+! n_-!}} \left( \cos \frac{\theta}{2} \right)^{n_0} \left( \sin \frac{\theta}{2} \right)^{N-n_0}. \end{aligned} \quad (21)$$

Comparison of Eq. (18) for  $\xi = 0$  and Eq. (21) then shows that

$$\sum_{n=0}^N e^{in\theta} I(n, n_0) = e^{i\theta N/2} \left( \cos \frac{\theta}{2} \right)^{n_0} \left( \sin \frac{\theta}{2} \right)^{N-n_0} \quad (22)$$

immediately yielding

$$I(n, n_0) = \frac{1}{\pi} \int_0^\pi dx e^{ix(N-2n)} (\cos x)^{n_0} (\sin x)^{N-n_0}. \quad (23)$$

Using Eq. (18), we can write the probability density

$$P(n_+, n_-, n_0) = |\langle n_+, n_-, n_0 | \Psi_{\text{rec}} \rangle|^2$$

as the product of two functions,

$$P(n_+, n_-, n_0) = P_\pm(n_+, n_-, n_0) P_0(n_0, \theta, \xi), \quad (24)$$

where

$$P_\pm(n_+, n_-, n_0) = \frac{(N-n_0)!}{n_+! n_-! 2^{N-n_0}} \quad (25)$$

and

$$P_0(n_0, \theta, \xi) = \binom{N}{n_0} |\Sigma(n_0, \theta, \xi)|^2 \quad (26)$$

with the function  $\Sigma(n_0, \theta, \xi)$  given by the relation

$$\Sigma(n_0, \theta, \xi) = \sum_{n=0}^N e^{i\theta(n-N/2)-2i\xi(n-N/2)^2} I(n, n_0). \quad (27)$$

The function  $P_\pm$  describes the probability of observing  $n_+$  and  $n_-$  atoms in the right and left clouds, respectively, for any given number  $n_0 = N - (n_+ + n_-)$  atoms in the central cloud. This function is independent both on  $\theta$  and the nonlinearity  $\xi$  and is normalized to one,

$$\sum_{n_+=0}^{N-n_0} P_\pm = \sum_{n_+=0}^{N-n_0} \frac{(N-n_0)! 2^{n_0-N}}{n_+! (N-n_0-n_+)!} = 1. \quad (28)$$

With the use of Stirling's approximation in Eq. (25),  $P_\pm$  can be simplified to

$$P_\pm = \sqrt{\frac{2}{\pi(N-n_0)}} \exp \left[ \frac{(n_+ - n_-)^2}{2(N-n_0)} \right], \quad (29)$$

with  $n_+ + n_- = N - n_0$ . The function  $P_0(n_0, \theta, \xi)$  describes the probability of observing  $n_0$  atoms in the central cloud. The effects of both the external phase  $\theta$  and the nonlinearity  $\xi$  are contained in this function. It is also normalized to one,

$$\sum_{n_0=0}^N P_0(n_0, \theta, \xi) = 1. \quad (30)$$

The function  $\Sigma$  (27) satisfies the symmetry relations

$$\begin{aligned} \Sigma(n_0, -\theta) &= (-1)^{N-n_0} \Sigma(n_0, \theta), \\ \Sigma(n_0, \pi - \theta) &= \Sigma(N - n_0, \theta). \end{aligned} \quad (31)$$

The probability function  $P_0$  given by Eq. (26) is periodic in  $\theta$  with the period  $2\pi$ . Relations (31) allow us in the following to restrict our analysis to the values of  $\theta$  lying in the interval  $0 \leq \theta \leq \pi/2$  since

$$\begin{aligned} P_0(n_0, -\theta) &= P_0(n_0, \theta), \\ P_0(n_0, \pi - \theta) &= P_0(N - n_0, \theta). \end{aligned} \quad (32)$$

#### IV. EVALUATING THE PROBABILITY DENSITY FUNCTION $P_0$

The exact expression for the probability density distribution function  $P_0$  given by Eq. (26) is relatively complex and does not lend itself readily to an easy interpretation. In the following we shall transform and simplify it to make it more amenable for the subsequent analysis.

The integral  $I(n, n_0)$  given by Eq. (23) can be evaluated in the complex plane by the method of steepest descent to yield

$$\begin{aligned} I(n, n_0) &= \frac{1}{\sqrt{\pi N}} \exp \left[ (N-n_0) \ln \sqrt{1 - \frac{n_0}{N}} + n_0 \ln \sqrt{\frac{n_0}{N}} \right. \\ & \quad \left. - \frac{(n - N/2)^2}{N} \right] \left[ e^{i(N-2n) \arccos \sqrt{n_0/N}} \right. \\ & \quad \left. + (-1)^{N-n_0} e^{-i(N-2n) \arccos \sqrt{n_0/N}} \right]. \end{aligned} \quad (33)$$

Using Eq. (33) in the expression for  $\Sigma$  [Eq. (27)], approximating the summation by integration, and evaluating the integral, we get

$$\Sigma(n_0) = \frac{1}{\sqrt{1+2i\xi N}} \exp \left[ (N-n_0) \ln \sqrt{1-\frac{n_0}{N}} + n_0 \ln \sqrt{\frac{n_0}{N}} \right] [e^{-\eta_-} + (-1)^{N-n_0} e^{-\eta_+}], \quad (34)$$

where

$$\eta_{\mp} = \frac{N(\arccos \sqrt{n_0/N} \mp \theta/2)^2}{1+2i\xi N}. \quad (35)$$

Finally, the use of the Stirling approximation and Eq. (34) in Eq. (26) results in the expression for the probability density  $P_0$ ,

$$P_0(n_0) = \frac{1}{\sqrt{2\pi(1+4\xi^2 N^2)}} \sqrt{\frac{N}{n_0(N-n_0)}} \times |e^{-\eta_-} + (-1)^{N-n_0} e^{-\eta_+}|^2. \quad (36)$$

Equation (36) is not applicable at the two end points,  $n_0 = 0$  and  $n_0 = N$ , where it has to be replaced by the expressions

$$P_0(0) = \frac{1}{\sqrt{1+\xi^2 N^2}} \exp \left[ \frac{-2(\pi-\theta)^2 N}{1+\xi^2 N^2} \right], \quad (37)$$

$$P_0(N) = \frac{1}{\sqrt{1+\xi^2 N^2}} \exp \left[ \frac{-2\theta^2 N}{1+\xi^2 N^2} \right].$$

## V. FEATURES OF THE PROBABILITY DENSITY

Expressions (25) and (36) for the probability density functions  $P_{\pm}$  and  $P_0$  give the probability  $P(n_+, n_-, n_0) = P_{\pm} P_0$  of observing any given number of atoms in the three output ports (three atomic clouds) of an optical beamsplitter. The function  $P_{\pm}$  describes the probability of observing  $n_{\pm}$  atoms in the right and left clouds, respectively, for a fixed number  $n_0 = N - (n_+ + n_-)$  atoms in the central cloud. This probability is the Gaussian distribution (29) with the average values of  $n_{\pm}$  and  $n_+$  given by

$$\langle n_- \rangle = \langle n_+ \rangle = \frac{1}{2}(N - n_0) \quad (38)$$

and the standard deviations

$$\Delta n_- = \Delta n_+ = \frac{1}{2}\sqrt{N - n_0}. \quad (39)$$

The numbers of atoms in the right and left clouds are anticorrelated,

$$\text{Cov}(n_+, n_-) = \langle n_+ n_- \rangle - \langle n_+ \rangle \langle n_- \rangle = -\frac{1}{4}(N - n_0). \quad (40)$$

The probability to find  $n_0$  atoms in the central cloud is given by the function  $P_0(n_0, \theta, \xi)$  Eq. (36). The dependence of this function on its arguments is not trivial, so we start the analysis by evaluating the expectation value of the atoms on the central cloud  $\langle n_0 \rangle$  and the standard deviation  $\Delta n_0$ .

The function  $P_0$  is proportional to the modulus squared of the sum of two terms:  $P_0 \propto |e^{-\eta_-} + (-1)^{N-n_0} e^{-\eta_+}|^2$ , where  $\eta_{\mp}$  are given by Eq. (35). The relative phase difference between them, as a function of  $n_0$ , changes rapidly due to the multiplier

$(-1)^{n_0}$ . Thus, the interference terms can be neglected in calculating both the mean and the standard derivation,

$$\langle n_0 \rangle \approx \frac{\sqrt{N}}{\sqrt{2\pi(1+4\xi^2 N^2)}} \int_0^N dn_0 \sqrt{\frac{n_0}{N-n_0}} \times (e^{-2\text{Re}\eta_-} + e^{-2\text{Re}\eta_+}).$$

Evaluation of the above integral yields

$$\langle n_0 \rangle = \frac{N}{2} [1 + \exp(-2\xi^2 N) \cos \theta]. \quad (41)$$

Similarly, the standard deviation evaluates to

$$(\Delta n_0)^2 = \frac{N^2}{8} [1 - \exp(-4\xi^2 N)][1 - \exp(-4\xi^2 N) \cos 2\theta]. \quad (42)$$

To understand these results, we shall look at the dependence of the function  $P_0$  on the number of atoms  $n_0$  for different values of the strength of the interatomic interactions  $\xi$ . At relatively small values of  $\xi$  such that  $\xi \ll 1/\sqrt{N}$ , the term  $\exp(-\eta_-)$  in the expression (36) for the probability dominates the second one. The probability  $P_0$  is then a simple Gaussian

$$P_0 \propto \exp \left[ -\frac{2N(\arccos \sqrt{n_0/N} - \theta/2)^2}{1+4\xi^2 N^2} \right] \quad (43)$$

with the maximum located at  $n_0 = N \cos^2 \theta/2$ . This situation is shown in Fig. 1. The two curves in this figure are plots of the function  $P_0(n_0)$  given by Eq. (36) versus  $n_0$  for two different values of the interatomic interaction strength  $\xi$ . Both curves correspond to the same value of the angle  $\theta$ . The most noticeable feature of Fig. 1 is the increase in the width of the probability distribution with  $\xi$ . This behavior is explained by Eq. (41), which in the limit  $\xi \ll 1/\sqrt{N}$  reduces to

$$\Delta n_0 \approx \frac{\sqrt{N}}{2} \sin \theta \sqrt{1+4\xi^2 N^2}. \quad (44)$$

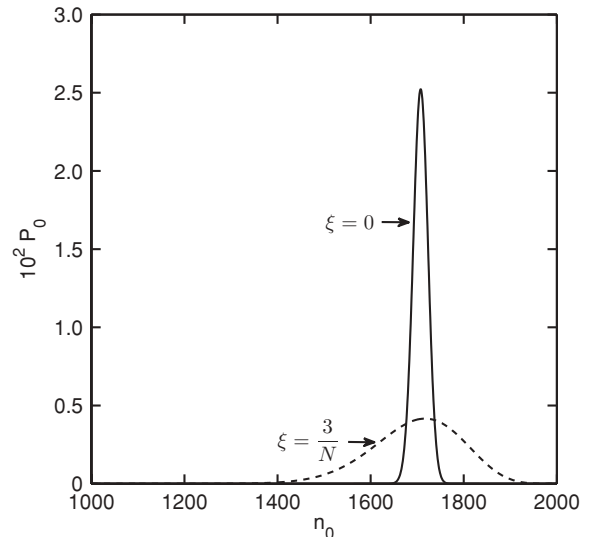


FIG. 1. Probability function  $P_0$  vs  $n_0$  for  $\xi = 0$  and  $\xi = 3/N$ . For both curves,  $\theta = \pi/4$  and  $N = 2000$ . Note that the abscissa axis range is from  $n_0 = 1000$  to  $2000$ .

For very small values of  $\xi$  ( $\xi \ll 1/N$ ), the influence of the interatomic interactions on the operation of the beamsplitter is negligible. The relative standard deviation of the number of atoms in the central cloud is inversely proportional to the square root of the total number of atoms in the system:  $\Delta n_0/N \propto 1/\sqrt{N}$ . For  $1/N \ll \xi \ll 1/\sqrt{N}$ , the width of the distribution linearly grows with the increase in  $\xi$ .

The mean value of  $n_0$  for  $\xi \ll 1/\sqrt{N}$  reasonably closely corresponds to the position of the peak. Equation (41) for  $\langle n_0 \rangle$  in this limit yields

$$\langle n_0 \rangle \approx \frac{N}{2} (1 + \cos \theta). \quad (45)$$

As is seen,  $n_0$  depends on  $\theta$  but not on  $\xi$ .

For larger values of  $\xi \approx 1/\sqrt{N}$ , the width of the probability distribution function  $P_0$  becomes of the order of the total number of atoms in the system  $N$ . The two terms  $\exp(-\eta_-)$  and  $\exp(-\eta_+)$  in Eq. (36) are now comparable in magnitude. The transition to this limit is shown by Figs. 2 and 3. Black regions not resolved in Figs. 2 and 3 correspond to rapid spatial oscillations with the period 2. These oscillations are clearly seen in Fig. 4, which shows part of Fig. 3 for a narrow range of values of  $n_0$ . The oscillations are caused by the interference between the two terms in Eq. (36). As the magnitude of  $\xi$  approaches  $1/\sqrt{N}$ , these terms become comparable in magnitude. Because of the nearly  $\pi$ -phase change between the two terms every time  $n_0$  changes by one due to the factor  $(-1)^{n_0}$ , the two terms consecutively add either in phase or out of phase when one steps through different values of  $n_0$ . Along with rapid spatial oscillations, both Figs. 2 and 3 demonstrate oscillations of the envelopes at a much slower spatial rate which are more pronounced for larger values of the interaction strength. These oscillations are due to the fact that the relative phase of the terms  $\exp(-\eta_-)$  and  $\exp(-\eta_+)$  in Eq. (36) changes with  $n_0$ . The nodes in Fig. 3 correspond to the value of this relative phase being equal to 0 or a  $\pi$  and antinodes have the phase shifted by  $\pm\pi/2$ .

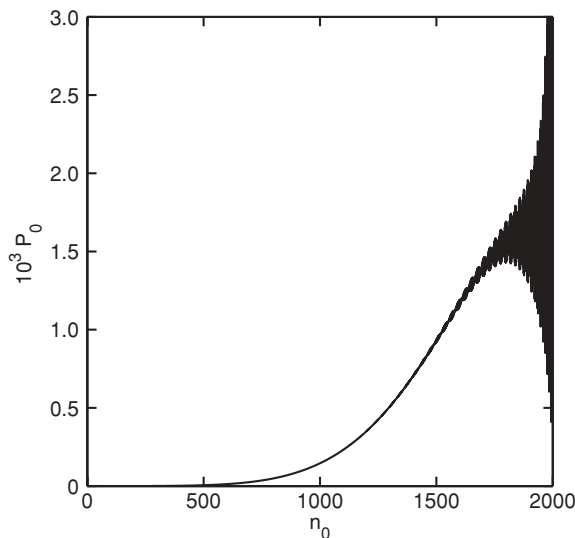


FIG. 2. Probability function  $P_0$  vs  $n_0$  for  $\xi = 0.2/\sqrt{N}$ ,  $\theta = \pi/4$ , and  $N = 2000$ .

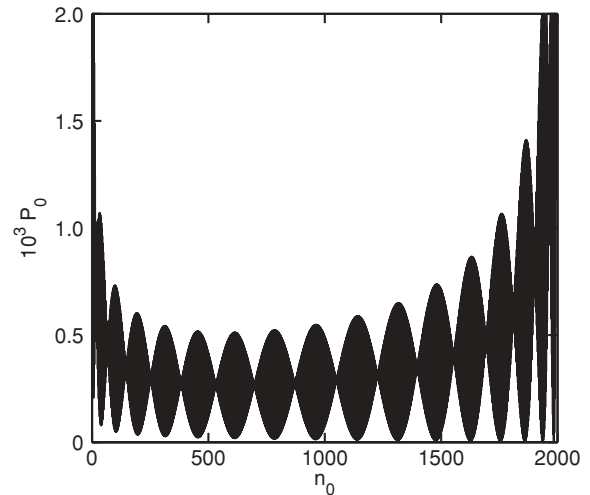


FIG. 3. Probability function  $P_0$  vs  $n_0$  for  $\xi = 1/\sqrt{N}$ ,  $\theta = \pi/4$ , and  $N = 2000$ .

Figures 2 and 3 indicate that the probability  $P_0$  and, as a consequence,  $\langle n_0 \rangle$  and  $\Delta n_0$ , become less sensitive to changes in the environment-introduced angle  $\theta$ . This fact is graphically illustrated by Figs. 5 and 6, showing the average value of the number of atoms in the central cloud  $\langle n_0 \rangle$  and the standard deviation  $\Delta n_0$  versus  $\theta$  as given by Eqs. (41) and (42), respectively. Figure 5 demonstrates that increased interatomic interactions eventually lead to the loss of contrast of interference fringes. Additionally, larger interatomic interactions cause larger shot-to-shot fluctuations in the number of atoms in each of the three output ports, as is seen from Fig. 6.

The loss of contrast of the interference fringes can be quantified by writing Eq. (41) as

$$\langle n_0 \rangle = \frac{N}{2} (1 + V \cos \theta), \quad (46)$$

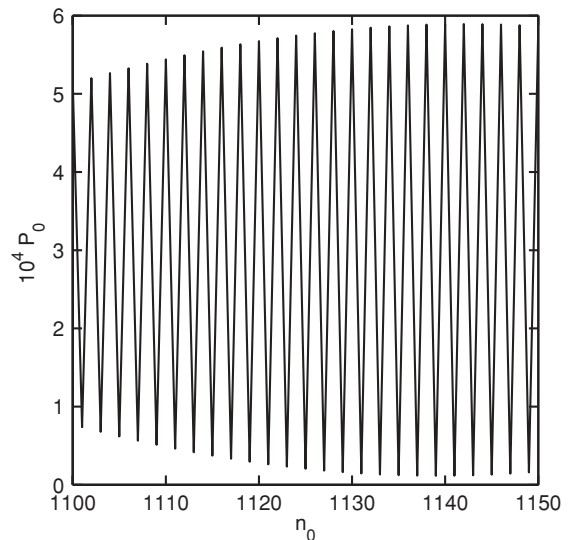


FIG. 4. An enlargement of a part of Fig. 3 showing fast-scale spatial oscillations of the probability function.

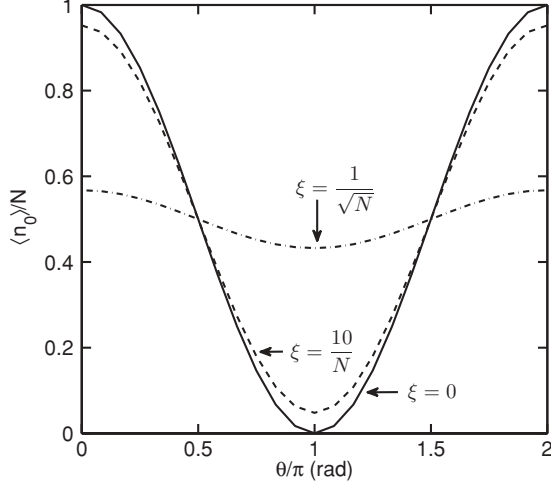


FIG. 5. Normalized mean value of the number of atoms in the central cloud  $\langle n_0 \rangle / N$  vs  $\theta$  for  $N = 2000$ .

where

$$V = \exp(-2\xi^2 N) \quad (47)$$

is the fringe contrast. Figure 7 shows the fringe contrast  $V$  [Eq. (47)] as a function of  $\xi$  and demonstrates that the values of  $\xi$  approaching  $1/\sqrt{N}$  result in a washout of the interference fringes.

## VI. DISCUSSION

The value of the accumulated nonlinear phase per atom due to interatomic interactions  $\xi$  given by Eq. (12) depends on the volume of the BEC clouds [cf. Eq. (4)]. Experiments [14,18,25–27] to be discussed in the following were conducted in parabolic traps with confining potentials of the form:

$$V = \frac{M}{2} (\omega_x^2 x^2 + \omega_y^2 y^2 + \omega_z^2 z^2). \quad (48)$$

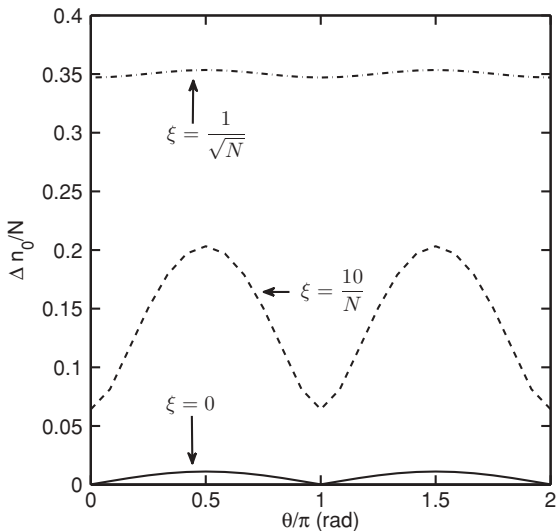


FIG. 6. Normalized standard deviation  $\Delta n_0 / N$  vs  $\theta$  for  $N = 2000$ .

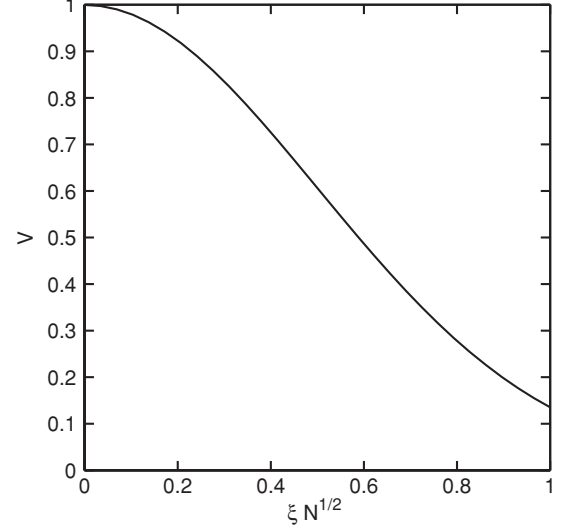


FIG. 7. Interference fringes contrast  $V$  as a function of the strength of the interatomic interactions  $\xi \sqrt{N}$ .

Density profiles of the moving clouds are well described by the Thomas-Fermi approximation

$$n(\mathbf{r}) = |\psi_{\pm}|^2 = \frac{15}{8\pi R_x R_y R_z} \left( 1 - \frac{x^2}{R_x^2} - \frac{y^2}{R_y^2} - \frac{z^2}{R_z^2} \right) \quad (49)$$

(recall that  $\psi_{\pm}$  are normalized to one).

Immediately after the splitting pulses, the density profiles of the moving clouds are the same as that of the initial BEC cloud containing  $N$  atoms and being in equilibrium in the confining potential given by Eq. (48). After the splitting, each moving cloud contains on the average  $N/2$  atoms. The repulsive nonlinearity is no longer balanced by the confining potential and the radii of both clouds start to oscillate. The maximum size of the oscillating clouds is the equilibrium size corresponding to  $N$  atoms and the minimum size lies below the equilibrium size corresponding to  $N/2$  atoms. For estimates, we can take  $R_i^2$  in Eq. (49) to be given by equilibrium size of a cloud with  $N/2$  atoms:  $R_i^2 = 2\mu/M\omega_i^2$ , where [37,38]

$$\mu = \frac{1}{4} \left( \frac{15}{\sqrt{2\pi}} \right)^{2/5} \left( N \frac{U_0}{\bar{a}^3} \right)^{2/5} (\hbar\bar{\omega})^{3/5}, \quad (50)$$

$U_0 = 4\pi\hbar^2 a_{sc}/M$ ,  $\bar{\omega} = (\omega_x \omega_y \omega_z)^{1/3}$ , and  $\bar{a} = \sqrt{\hbar/M\bar{\omega}}$ .

Evaluation of the constant  $g$  [Eq. (4)] yields  $g = (15U_0)/(28\pi R_x R_y R_z)$ . The accumulated nonlinear phase per atom due to interatomic interactions  $\xi$ , Eq. (12), is then given by the expression

$$\xi = \frac{1}{7} (30\sqrt{2})^{2/5} \left( \frac{a_s}{\bar{a}} \right)^{2/5} \bar{\omega} T N^{-3/5}, \quad (51)$$

where  $T$  is the duration of the interferometric cycle.

The relative importance of interatomic interaction effects on the operation of the interferometer is determined by the parameter  $P = \xi \sqrt{N}$ ,

$$P = 0.64 \left( \frac{a_s}{\bar{a}} \right)^{2/5} (\bar{\omega} T) N^{-1/10}. \quad (52)$$

Figure 7 shows that the contrast of the interference fringes decreases with the increase in  $P$ . The condition of good

contrast can be somewhat arbitrarily stated as  $P < 1/2$  (for  $P = 0.5$ , the contrast  $V = 0.6$ ).

Equation (52) shows that  $P \propto T\omega^{6/5}N^{-1/10}$ . The dependence of  $P$  on the total number of atoms in the BEC clouds is very weak, and so this parameter is primarily dependent on the duration of the interferometric cycle and the averaged frequency of the trap.

Experiments by Wang *et al.* [14] were conducted using the Michelson geometry. The BEC consisted of about  $10^5$   $^{87}\text{Rb}$  atoms [39]. The transverse and longitudinal frequencies of the trap were 177 and 5 Hz, respectively. The propagation time  $T$  was up to 10 ms. For these parameters and the value of the scattering length  $a_s = 5.2 \times 10^{-9}$  m [40], Eq. (52) yields  $P \approx 1.6 \times 10^{-2}$ . Thus, the interatomic interactions were not limiting the visibility of the interference fringes in these experiments.

Similar experiments were performed by Garcia [25] and Burke [26] also in the geometry of a Michelson interferometer. In Ref. [25], a BEC cloud of about  $10^4$   $^{87}\text{Rb}$  atoms has been produced in a trap with the frequencies of 6.0, 1.2, and 3.0 Hz, respectively. The interferometric time  $T$  was about 40 ms. Using Eq. (52), we can evaluate the value of the parameter  $P$  in the experiment as  $P \approx 10^{-2}$ , which was too small to result in observed degradation of the contrast. The loss of visibility in the experiment [25] was attributed by the authors to spatial noise on the splitting beams and asymmetric splitting of the cloud due to the condensate's residual motion when it was loaded into the trap. At longer times, the loss of coherence might have been caused by various noise sources. Similar results were reported in Ref. [26], where the confinement frequencies were deliberately kept weak, making the atomic density and thus the interatomic interaction effects small.

Horikoshi *et al.* [18,27] demonstrated a BEC Mach-Zehnder interferometer. The number of atoms in Ref. [27] was about  $3 \times 10^3$  and the radial frequency of the trap was fixed at 60 Hz. The experiments have been conducted for two different values of the axial frequencies and interrogation times  $T$ . At an axial frequency of  $\omega_z = 2\pi \times 17$  Hz and the propagation time of the cloud about  $T = 60$  ms, the parameter  $P = \xi\sqrt{N}$  estimated using Eq. (52) turns out to be about 0.38. For this value of  $P$ , Eq. (47) gives the value of the fringe contrast about 70%. The experimental value is 30% [27]. Similarly, for the axial frequency 10.29 Hz and the interferometric time 97 ms, Eq. (52) gives the value of  $P \approx 0.5$  corresponding to an estimated contrast of 58%. In this case no fringes were observed experimentally with about 40% scatter of the data points. The authors of Ref. [27] conjecture that vibrations could be the main source of the loss of fringes in their experiments. The above estimates indicate that the interatomic interactions discussed in the present paper could be also partially responsible for the observed degradation of the interference fringe.

#### ACKNOWLEDGMENTS

This work was partially supported by the Defense Advanced Research Projects Agency (Grant No. W911NF-04-1-0043). A.A.Z. thanks E. Zhirova for helpful discussions.

#### APPENDIX: MACH-ZEHNDER-TYPE INTERFEROMETER

In a Mach-Zehnder-type cold-atom interferometer, the optical splitting  $\pi/2$  pulse transforms a BEC cloud at rest in a superposition of two clouds  $\psi_0$  and  $\psi_{+1}$ . The first cloud is at rest and the second one is moving. The clouds evolve during the time  $T/2$  and are then subject to the action of a  $\pi$  pulse. It stops the moving cloud and brings the one at rest into motion, i.e., transforms the  $\psi_0$  cloud into  $\psi_{+1}$  and vice versa. After additional evolution time  $T/2$ , the clouds are subject to a recombination  $\pi/2$  pulse. After the recombination, both  $\psi_0$  and  $\psi_{+1}$  are in general populated.

Analysis of a Mach-Zehnder-type interferometer parallels that given in the paper for the Michelson-type interferometer and is somewhat simpler because with the Mach-Zehnder interferometer there are only two output ports as opposed to three in the case of a Michelson-type interferometer.

Let  $b_0^\dagger$  and  $b_{+1}^\dagger$  be operators which create an atom belonging to a cloud at rest and moving to the right, respectively. The Hamiltonian is of the form [cf. Eq. (3)]

$$H_{\text{eff}} = -\frac{W}{2}(\hat{n}_{+1} - \hat{n}_0) + g(\hat{n}_{+1}^2 + \hat{n}_0^2), \quad (\text{A1})$$

where the notations are the same as in Sec. II.

The state vector of the system at the beginning of the interferometric cycle before the splitting pulse is given by Eq. (5).

The splitting and recombination  $\pi/2$  pulse couples the operators  $b_1$  and  $b_0$  according to the rules

$$\begin{aligned} b_0 &\rightarrow \frac{1}{\sqrt{2}}(b_0 + ib_{+1}), \\ b_{+1} &\rightarrow \frac{1}{\sqrt{2}}(ib_0 - b_{+1}). \end{aligned} \quad (\text{A2})$$

For the  $\pi$  pulse, similarly, one has

$$b_0 \rightarrow ib_{+1}, \quad b_{+1} \rightarrow -ib_0. \quad (\text{A3})$$

By repeating steps of Sec. II, we arrive at the following expression for the state vector of the system after the recombination pulse:

$$\begin{aligned} |\Psi_{\text{rec}}\rangle &= \frac{1}{2^N \sqrt{N!}} \sum_{n=0}^N \binom{N}{n} e^{i\theta(n-N/2) - 2i\xi(n-N/2)^2} \\ &\times (b_0^\dagger - ib_{+1}^\dagger)^n (b_0^\dagger + ib_{+1}^\dagger)^{N-n} |0\rangle. \end{aligned} \quad (\text{A4})$$

The probability to have after the recombination  $n_0$  atoms at rest and  $n_+ = N - n_0$  atoms moving is given by the modulus squared of the probability amplitude  $\langle n_0, N - n_0 | \Psi_{\text{rec}} \rangle$ . Here

$$|\langle n_0, n_+ \rangle| = \frac{(b_0^\dagger)^{n_0} (b_{+1}^\dagger)^{n_+}}{\sqrt{n_0!} \sqrt{n_+!}} |0\rangle \quad (\text{A5})$$

is the state with  $n_0$  atoms at rest and  $n_+$  atoms moving, respectively.

Repeating steps of Sec. III, the probability  $P(n_0) = |\langle n_0, N - n_0 | \Psi_{\text{rec}} \rangle|^2$  can be written as

$$P(n_0, \theta, \xi) = \binom{N}{n_0} |\Sigma(n_0, \theta, \xi)|^2, \quad (\text{A6})$$

where  $\Sigma$  is given by Eq. (27) with the function  $I(n, n_0)$  in Eq. (27) given by the relation (23). The probability  $P$  [Eq. (A6)] is thus completely identical to the probability

$P_0$  [Eq. (26)] of Sec. III. All relations of Secs. IV and VI equally apply to the case of the Mach-Zehnder-type interferometer.

- 
- [1] P. R. Berman, *Atom Interferometry* (Academic, New York, 1997).
- [2] L. Stodolsky, *Gen. Relativ. Gravit.* **11**, 391 (1979).
- [3] J. B. Fixler, G. T. Foster, J. M. McGuirk, and M. A. Kasevich, *Science* **315**, 74 (2007).
- [4] M. Kasevich and S. Chu, *Phys. Rev. Lett.* **67**, 181 (1991).
- [5] M. Kasevich and S. Chu, *Appl. Phys. B* **54**, 321 (1992).
- [6] A. Peters, K. Y. Chung, and S. Chu, *Metrologia* **38**, 25 (2001).
- [7] C. R. Ekstrom, J. Schmiedmayer, M. S. Chapman, T. D. Hammond, and D. E. Pritchard, *Phys. Rev. A* **51**, 3883 (1995).
- [8] A. Wicht, J. M. Hensley, E. Sarajlic, and S. Chu, *Phys. Scr. T* **102**, 82 (2002).
- [9] O. Carnal and J. Mlynek, *Phys. Rev. Lett.* **66**, 2689 (1991).
- [10] D. M. Giltner, R. W. McGowan, and S. A. Lee, *Phys. Rev. Lett.* **75**, 2638 (1995).
- [11] E. M. Rasel, M. K. Oberthaler, H. Batelaan, J. Schmiedmayer, and A. Zeilinger, *Phys. Rev. Lett.* **75**, 2633 (1995).
- [12] K. Moler, D. S. Weiss, M. Kasevich, and S. Chu, *Phys. Rev. A* **45**, 342 (1992).
- [13] M. H. Anderson, J. R. Ensher, M. R. Matthews, C. E. Wieman, and E. A. Cornell, *Science* **269**, 198 (1995).
- [14] Y. J. Wang, D. Z. Anderson, V. M. Bright, E. A. Cornell, Q. Diot, T. Kishimoto, M. Prentiss, R. A. Saravanan, S. R. Segal, and S. Wu, *Phys. Rev. Lett.* **94**, 090405 (2005).
- [15] M. R. Andrews, C. G. Townsend, H. J. Miesner, D. S. Durfee, D. M. Kurn, and W. Ketterle, *Science* **275**, 637 (1997).
- [16] Y. Shin, M. Saba, T. A. Pasquini, W. Ketterle, D. E. Pritchard, and A. E. Leanhardt, *Phys. Rev. Lett.* **92**, 050405 (2004).
- [17] L. A. Collins, L. Pezzé, A. Smerzi, G. P. Berman, and A. R. Bishop, *Phys. Rev. A* **71**, 033628 (2005).
- [18] M. Horikoshi and K. Nakagawa, *Phys. Rev. A* **74**, 031602 (2006).
- [19] M. Fattori, C. D'Errico, G. Roati, M. Zaccanti, M. Jona-Lasinio, M. Modugno, M. Inguscio, and G. Modugno, *Phys. Rev. Lett.* **100**, 080405 (2008).
- [20] J. Estève, A. Weller, S. Giovannazzi, and M. K. Oberthaler, *Nature (London)* **455**, 1216 (2008).
- [21] C. Gross, T. Zibold, E. Nicklas, J. Estève, and M. K. Oberthaler, *Nature (London)* **464**, 1165 (2010).
- [22] M. F. Riedel, P. Böhi, Y. Li, T. W. Hänsch, A. Sinatra, and P. Treutlein, *Nature (London)* **464**, 1170 (2010).
- [23] J. A. Dunningham and K. Burnett, *Phys. Rev. A* **70**, 033601 (2004).
- [24] L. Pezzé, L. A. Collins, A. Smerzi, G. P. Berman, and A. R. Bishop, *Phys. Rev. A* **72**, 043612 (2005).
- [25] O. Garcia, B. Deissler, K. J. Hughes, J. M. Reeves, and C. A. Sackett, *Phys. Rev. A* **74**, 031601(R) (2006).
- [26] J. H. T. Burke, B. Deissler, K. J. Hughes, and C. A. Sackett, *Phys. Rev. A* **78**, 023619 (2008).
- [27] M. Horikoshi and K. Nakagawa, *Phys. Rev. Lett.* **99**, 180401 (2007).
- [28] S. R. Segal, Q. Diot, E. A. Cornell, A. A. Zozulya, and D. Z. Anderson, *Phys. Rev. A* **81**, 053601 (2010).
- [29] M. Olshanii and V. Dunjko, e-print [arXiv:cond-mat/0505358v2](https://arxiv.org/abs/cond-mat/0505358v2).
- [30] J. A. Stickney, D. Z. Anderson, and A. A. Zozulya, *Phys. Rev. A* **75**, 063603 (2007).
- [31] J. A. Stickney, R. P. Kafle, D. Z. Anderson, and A. A. Zozulya, *Phys. Rev. A* **77**, 043604 (2008).
- [32] Y. Castin and J. Dalibard, *Phys. Rev. A* **55**, 4330 (1997).
- [33] J. Javanainen and M. Wilkens, *Phys. Rev. Lett.* **78**, 4675 (1997).
- [34] E. M. Wright, T. Wong, M. J. Collett, S. M. Tan, and D. F. Walls, *Phys. Rev. A* **56**, 591 (1997).
- [35] G.-B. Jo, Y. Shin, S. Will, T. A. Pasquini, M. Saba, W. Ketterle, D. E. Pritchard, M. Vengalattore, and M. Prentiss, *Phys. Rev. Lett.* **98**, 030407 (2007).
- [36] W. Li, A. K. Tuchman, H. C. Chien, and M. A. Kasevich, *Phys. Rev. Lett.* **98**, 040402 (2007).
- [37] G. Baym and C. J. Pethick, *Phys. Rev. Lett.* **76**, 6 (1996).
- [38] F. Dalfovo, S. Giorgini, L. P. Pitaevskii, and S. Stringari, *Rev. Mod. Phys.* **71**, 463 (1999).
- [39] P. D. D. Schwindt, E. A. Cornell, T. Kishimoto, Y. J. Wang, and D. Z. Anderson, *Phys. Rev. A* **72**, 023612 (2005).
- [40] P. S. Julienne, F. H. Mies, E. Tiesinga, and C. J. Williams, *Phys. Rev. Lett.* **78**, 1880 (1997).

# Index

- Annihilation operator, 29, 32
- Atom interferometer, 3
  - trapped-atom interferometer, 4
- Basis vectors, 57
- Bose-Einstein condensation, 20
- Bragg diffraction of atoms, 12
  - square-wave Bragg Pulses, 15
- Chemical potential, 20, 22, 26, 47, 48
- Contrast, 45, 50, 74, 77
- Creation operator, 29
- Critical phase space density, 21
- Critical temperature, 20, 22
- Diffraction of atoms, 10
- Discussion, 46
- Fourier transform, 34, 41
- Gross-Pitaevskii equation, 23, 24, 54, 58
- Guided-wave atom interferometer, 5, 78
  - Mach-Zehnder interferometer, 7
  - Michelson interferometer, 5
    - double reflection, 6, 76, 77
    - free oscillation, 7, 79
    - single reflection, 75
- Hamilton's principle, 24
- Harmonic potential, 24, 46
- Hydrodynamic approximation, 54
- Interferometric time, 4, 5, 8, 31, 50
- Introduction, 1
- Lagrangian, 24
- Many-body Hamiltonian, 28, 57
- Normalisation constants, 56, 61
- Outline, 8
- Phase
  - spatial, 63
  - environment, 31, 44, 60
  - spatial, 52, 60
  - two-body interaction, 31, 60, 77
- Phase diffusion, 27
  - Mach-Zehnder interferometer, 33, 50
    - probability, 34
    - probability amplitude, 33, 34
  - Michelson interferometer, 35, 49
    - cross-correlation, 37
    - mean, 37, 39, 42
    - probability, 35, 43
    - probability amplitude, 40
    - standard deviation, 37, 39, 42, 43
    - spatial oscillation, 43
- Phase space density, 22
- Polylogarithm function, 22
- Rabi frequency, 14
- Raman pulses, 11, 19
- Recombination matrix, 56
- Reflection matrix, 19, 20
- Riemann  $\zeta$  function, 21
- s-wave scattering length, 24, 29
- Spatial phase and phase diffusion, 52
  - mean, 61
  - moments of probability, 71
  - probability, 60, 64
  - standard deviation, 62
  - perturbation analysis
    - probability, 67



- 
- Splitting matrix, 19
  - State vector
    - Michelson interferometer, 28, 54
    - Mach-Zehnder interferometer, 32
  - Stirling's formula, 36, 61, 68
  
  - Thermal wavelength
    - de Broglie wavelength, 22
  - Thomas-Fermi approximation, 24, 47, 55
  - Two-body interaction, 27, 47
  
  - Velocity distribution, 22, 23